공학박사 학위논문

Investigation of Phase Stability of FCC High Entropy Alloy under Extreme Environment

극한 환경 하에서 FCC 하이엔트로피 합금의 상 안정성 고찰

2018년 8월

서울대학교 대학원

재료공학부

김 진 연

Investigation of Phase Stability of FCC High Entropy Alloy under Extreme Environment

극한 환경 하에서 FCC 하이엔트로피 합금의 상 안정성 고찰

지도 교수 박 은 수

이 논문을 공학박사 학위논문으로 제출함

2018년 8월

서울대학교 대학원

재료공학부

김 진 연

김진연의 박사 학위논문을 인준함

2018년 8월

위 원 장 김 영 운 (인)

부위원장 박 은 수 (인)

위 원 한 홍 남 (인)

위 원 서 진 유 (인)

위 원 장 혜 정 (인)

Abstract

Investigation of Phase Stability of FCC High Entropy Alloy under Extreme Environment

Jinyeon Kim
Department of Materials Science and Engineering
College of Engineering
Seoul National University

Unlike conventional alloy such as steels, high entropy alloy (HEA) consists of multiple elements with similar atomic percentage and shows solid solution with various atomic environment. Due to enhanced phase stability of the HEAs, they have been paid significantly attention among the multi-component system. The HEAs show stable solid solution, sluggish diffusion and lattice distortion effects, and consequently they exhibit excellent mechanical properties at cryogenic as well as elevated temperature and improved radiation resistance; however, the radiation resistance of HEAs was not studied in various alloy systems and at various irradiation conditions, thus it has not been comprehensively investigated.

In order to study a response of HEAs under irradiation, CrFeCoNiCu HEA consisting of CrFeCoNi-rich dendrite and Cu-rich interdendrite, was selected as a model alloy. Since both phases have FCC structures, they are easy to observe simultaneously at same irradiation condition. In this dissertation, the

microstructural defect evolution was elucidated under irradiation in order to investigate the radiation tolerance and, that is, the phase stability. The microstructure of as-cast CrFeCoNiCu HEA was analyzed using multi-scale characterization tools. As a result, it was observed that the dendrite contains nanometer-sized Cu-rich precipitates and the interdendrite has CrFeCoNi-rich precipitates, respectively. This indicates that Cr, Fe, Co, and Ni are chemically separated from Cu, which enables calculation of pseudo-binary phase diagram between CrFeCoNi and Cu. Using the phase diagram, solidification sequence was investigated and the annealing temperature was determined. After annealing at three phase region, solid CrFeCoNi, Cu, and liquid Cu-rich phase, the pre-existent precipitates grew and new precipitation formed in the matrix due to solubility change. The size and the fraction of these precipitates affected largely on the mechanical properties. Besides, just barreling was observed in composite pillar containing both dendrite and interdendrite without boundary sliding and multiple slip during deformation, suggesting stable boundary upon deformation.

To evaluate phase stability of HEAs under irradiation, MV electron and ion irradiation were carried out. First of all, dynamics of defect clusters was studied in real time using HVEM. As a result, the dislocation loops were dominantly observed in the dendrite and the stacking fault tetrahedra (SFTs) was dominant defect in the interdendrite. Moreover, the defect lifetime of dislocation loops in the dendrite was much longer than the SFTs in the interdendrite. Even at elevated temperature, the dislocation loops in the dendrite were dispersed uniformly and showed insignificant change in size distribution. On the other hand, the SFTs in the interdendrite were agglomerated and grew with asymmetric size distribution.

The phase stability of HEAs under irradiation was examined with the competition between radiation-enhanced diffusion and ballistic diffusion. Irradiation-induced defects lead to polygonization and irradiation-induced recrystallization consequently near surface that is activated by radiation-enhanced diffusion and subsequent dislocation climb. Specifically, the dendrite showed the polygonization with low angle boundary and the interdendrite was characterized by the continuous dynamic recrystallization with high angle boundary, which is quantified using precession electron diffraction technique. Prominent difference in irradiation-induced recrystallization between both phases results from lower initial defect density, higher recombination fraction in cascade, and sluggish diffusion and slower radiation-enhanced diffusion.

The dependence of the dose rate (with depth) on the precipitates in the dendrite was elucidated using atom probe tomography. Consequently, the precipitates shrunk and dissolved due to ballistic diffusion. The effective temperature that the parameter of phase stability in driven system was introduced and the effective temperature of the dendrite was higher value, suggesting that enhanced phase stability of HEAs under irradiation. In addition, when the implanted ion affected the microstructure and the ballistic diffusion was less activated with increasing depth, new precipitates formed, showing Ostwald ripening.

Besides, the hardness was measured in various alloy systems including widely utilized nuclear materials, pure metals, and HEAs in order to discuss the applicability of HEAs as the nuclear materials. Compared with the nuclear materials, the irradiation hardening of HEAs was higher a bit. This was quite

reasonable because the nuclear materials have radiation tolerant BCC matrix and the FCC HEAs in this study is not optimized in terms of alloy design and microstructure. Therefore, further studies such as alloy optimization is needed.

In this dissertation, the microstructure was comprehensively investigated in terms of defect and, thus enhanced phase stability of HEAs was elucidated under irradiation. The radiation damage investigated in one alloy system showed academically and industrially important results.

Keywords: High entropy alloy, Irradiation, Phase stability, Transmission electron microscope, Atom Probe Tomography, Microstructure

Student Number: 2014-30214

Table of Contents

List of Figures

List of Tables

List of Abbreviations

ADF	Annular dark field
APT	Atom probe tomography
BCC	Body-centered-cubic
BF	Bright field
BSE	Back-scattered electron
CDRX	Continuous dynamic recrystallization
DDRX	Discontinuous dynamic recrystallization
dpa	Displacements per atom
EBSD	Electron backscatter diffraction
EDS	Energy dispersive spectrometer
EELS	Electron energy-loss spectroscopy
EPMA	Electron probe micro-analyzer
FCC	Face-centered-cubic
F/M steel	Ferritic/martensitic steel
FFT	Fast Fourier transformation
FIB	Focused ion beams
FWHM	Full width at half maximum
GIXRD	Grazing incidence X-ray diffraction
HAADF	High angle annular dark field
HEA	High entropy alloy
HVEM	High voltage electron microscope
IM	Intermetallic
LPE	Lattice potential energy
MSAD	Mean-square atomic displacement
ND	Normal direction
ODS	Oxide dispersion strengthened
PED	Precession electron diffraction
PIPS	Precision ion polishing system
PKA	Primary knock-on atom
RAFM	Reduced activation ferritic/martensitic

RD	Rolling direction
RIS	Radiation-induced segregation
ROI	Region of interest
RPV	Reactor pressure vessel
SBIE	Seven-bond interaction energy
SE	Secondary electron
SEM	Scanning electron microscope
SFT	Stacking fault tetrahedral
SS	Solid solution
SQS	Special quasi-random structure
SRIM	Stopping and Range of ions in Materials
(S)TEM	(Scanning) Transmission electron microscope
TD	Transverse direction
XRD	X-ray diffraction

List of Symbols

a	Lattice parameter
C	The number of components
C_{eq}	Equilibrium concentration of vacancies at the irradiation temperature
C_p	Specific heat
D	(Thermally activated) diffusion coefficient
D_0	Pre-exponential factor for diffusion coefficient
D_B	Coefficient for ballistic diffusion
D_{eq}	Equilibrium diffusion coefficient in the absence of irradiation
D_{irrad}	Diffusion coefficient under irradiation
D_v	Diffusion coefficient of a vacancy
D^*	Effective diffusion coefficient
$\bar{d}$	Average displacement
E	Energy of particles
$\bar{E}$	Average modulus
e(n)	The number of blocks containing n solute atoms
F	Maximum number of thermodynamic degrees of freedom
F	Atomic displacement rate
g	Diffraction vector
$H_{v,\ irrad}$	Vickers hardness of irradiated alloy
$H_{v,\ un\text{-}irrad}$	Vickers hardness of un-irradiated alloy
N	Total number of atoms
N	The number of blocks sampled
N_v	Number density
n	The number of atoms in the reconstruction
k_B	Boltzmann's constant
P	The number of phases
Q	Activation energy for diffusion
R	Gas constant
R	Root-mean square displacement of an atom in the collision cascade

R	Radius of the volume equivalent sphere
S	Packing density
S’	Size-dependent density
T	Temperature
T_{tc}	Thermodynamic critical temperature
T_{eff}	Effective temperature
T_m	Melting temperature
T_{max}	Maximum recoil energy
m_i	Mass of target atom i
X_i	Fraction of the *i*th component
r_i	Atom radii of the *i*th
$\bar{r}$	Average atomic radii
Γ	Total jump frequency
Ω	Atomic volume
Ω_{ij}	Cohesive energy of *i*th and *j*th components
χ^2	chi-squared test
γ	X-ray angle of incidence
δ	Lattice distortion
ε	Displacement efficiency
η	Estimated detection efficiency
2θ	Diffraction angle
κ	Thermal conductivity
λ	Jump length
μ	Linear absorption coefficient
μ	Pearson coefficient
φ	Volume fraction of precipitates
ΔG_{mix}	Free energy of mixing
ΔH_{mix}	Mixing enthalpy
ΔS_{mix}	Mixing entropy
ΔQ	Activation energy for diffusion
ΔU_{strain}	Lattice distortion strain energy

Chapter 1. Introduction

As environmental problems and the issue of energy conservation have attracted global attention, the demand for environmentally friendly energy sources and various service environments has increased. In order to produce and use energy in the future, novel materials that perform and survive under extreme environments such as corrosion [24], cryogenic [34] and high temperature [37] environment, severe deformation [40] and irradiation [15] are necessary (Figure 1.1). Due to changes in the capabilities of materials, their response times should be investigated under extreme environments. Especially as the use of energy skyrockets, nuclear energy, which is affordable and clean, is entering the spotlight. However, nuclear energy is associated with safety and reliability issues. In order to overcome these concerns, the fourth generation of nuclear reactors has been developed. Accordingly, the materials required for these nuclear reactors should also be developed.

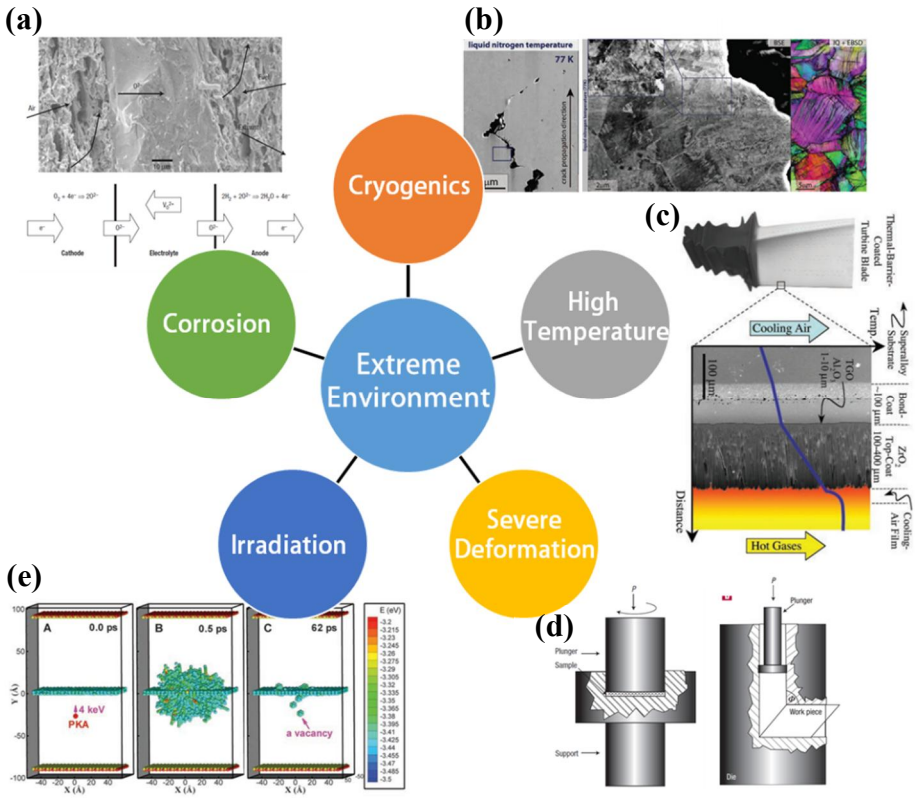

Figure 1.1 Illustration of extreme environments. (a) Corrosion environment: processing for an electrode-electrolyte structure [24]. (b) Cryogenic environment: ductile fracture by micro-void coalescence with more distorted crack path and deformation-induced nano-twinning at cryogenic temperature [34]. (c) High temperature condition: electron-beam physical-vapor deposited thermal barrier coatings (TBCs), showing temperature reduction provided by the TBC [37]. (d) Severe plastic deformation: high pressure torsion and equal channel angular pressing [39]. (e) Irradiation: a collision cascade near grain boundary at 300 K [15]. Reprinted from ref. [24], [34], [37], and [39] with permission through "Copyright Clearance Center". Also reprinted from [15] with permission from "AAAS".

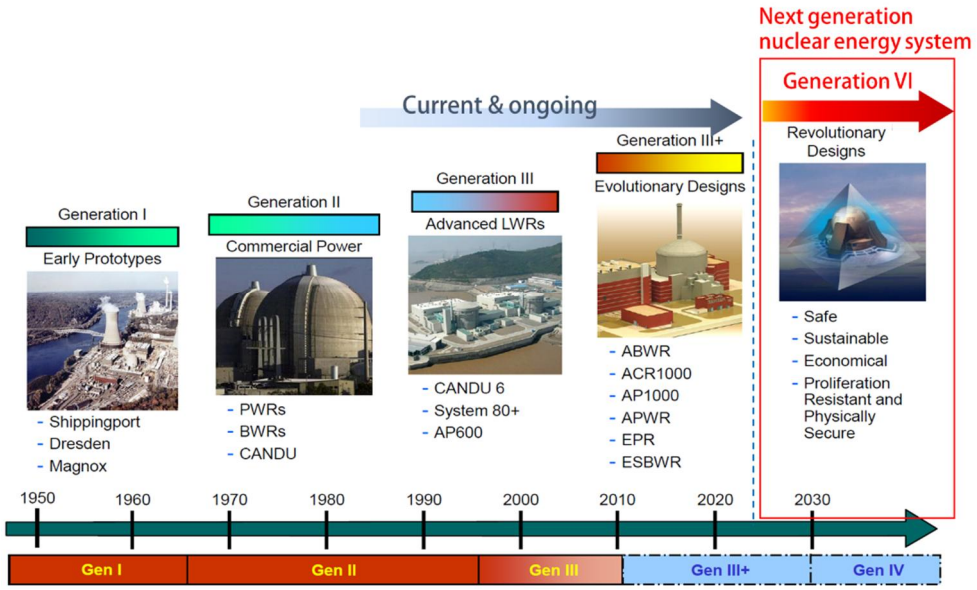

Figure 1.2 Development trend of nuclear energy system [2]. This is an Open Access article distributed under the terms of the Creative Commons Attribution License 2.0.

1.1 Radiation Effects on Materials

Generally, particle irradiation is the process of exposing incident energetic particles onto materials. When kinetic energy is sufficiently higher than the threshold energy for atomic displacement, permanent atomic displacement occurs from the lattice sites due to collisions. A collision cascade, also known as a displacement cascade or a displacement spike, is a set of nearby adjacent energetic collisions of atoms attributed to such energetic particles on materials (Figure 1.3) [41]. This phenomenon is affected by not only the density of the target material but also by the energy and mass of the incident particles, as discussed later in Sections 1.2.1 and 5.2.

The kinetic energy is converted to the thermal energy using the basic equation ($E = \frac{3}{2}Nk_BT$), where N is the total number of atoms, k_B is the Boltzmann constant and T is the absolute temperature in Kelvin. The temperature recalculated from the kinetic energy is on the order of 10,000 K; therefore, the region is known as a heat spike or a thermal spike. Heat spikes are characterized by the formation of an overly dense region surrounding a transient less dense region in the center of the cascade. Thermal spikes cool to ambient temperatures on the pico-second timescale, which is related to energy dissipation in the cascade reaction [30], and the temperature in this concept does not correspond to the thermodynamic equilibrium temperature. In the cascade reaction, various point defects are recombined [41]. Figure 1.4 shows the history of defects created as vacancies and interstitials during the

irradiation

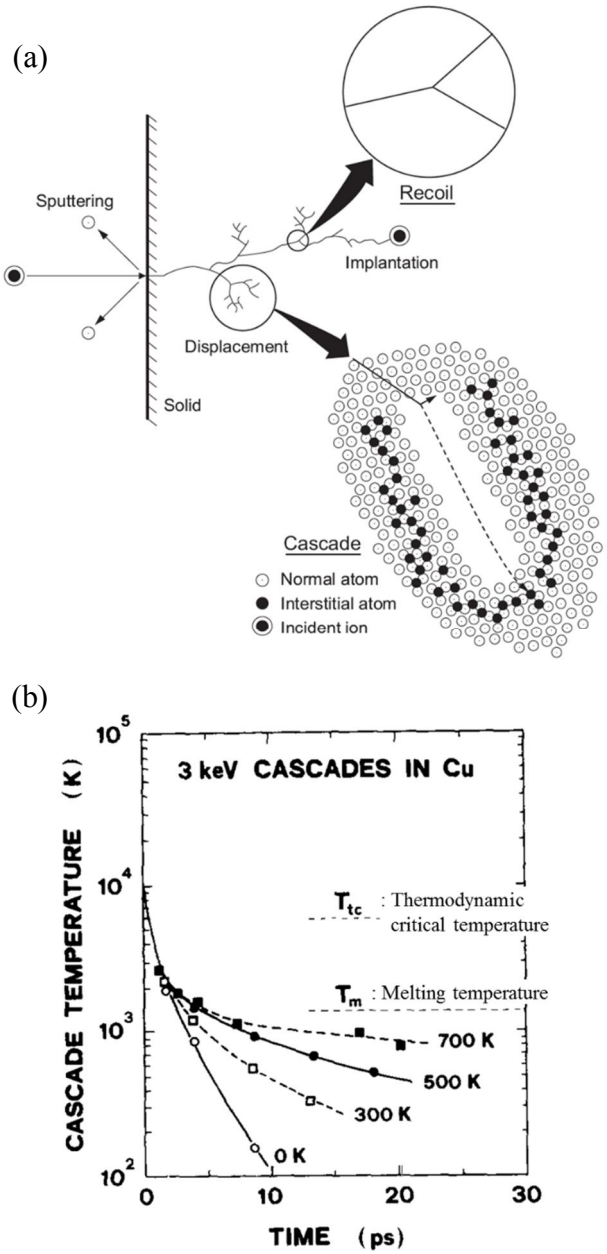

Figure 1.3 (a) Ballistic interaction of an energetic ion with a solid presenting the displacement spike [3] and temperature in the center of a 3 keV cascade in Cu as a function of time [30]. Reprinted from ref. [3] and [30] with permission through "Copyright Clearance Center".

process. The defects recombine significantly in the cascade, leaving a small fraction of defects that are free to migrate from the displacement zone. These surviving defects are referred to as freely migrating defects, which capable of long-range migration. They can be recombined outside of the cascade and can be absorbed at the sink in the matrix or at the grain boundaries, resulting in voids and/or loops or radiation-induced segregation, respectively [3].

To summarize irradiation induced damage, schematic diagrams of the spatial-temporal scale of radiation damage are presented in Figure 1.5. A radiation damage event consists of several processes: (1) incident energetic particles on the material; (2) the transfer of kinetic energy to the lattice atoms with subsequent primary knock-on atoms (PKA); (3) atomic displacement from the lattice sites; (4) the production of a displacement cascade; (5) the completion of the PKAs as interstitials and/or vacancies; and (6) the formation, migration, and dissolution or growth of defect clusters. Likewise, radiation damage shows various lengths or time scales ranging from the sub-nanometer or picosecond to even millimeters or years (Figure 1.5), with individual events occurring initially, followed by macroscopic radiation damage and microstructural evolution and degraded properties. Hence, changes in the microstructure under irradiation can be utilized as an indicator of the radiation resistance of the material. Due to the limited spatial and time resolutions, experiments provide only the length and time scale from nm to μs, as denoted by the red dashed box in Figure 1.5. Consequently, this dissertation covers multi-scale microstructural evolution upon irradiation via experiments.

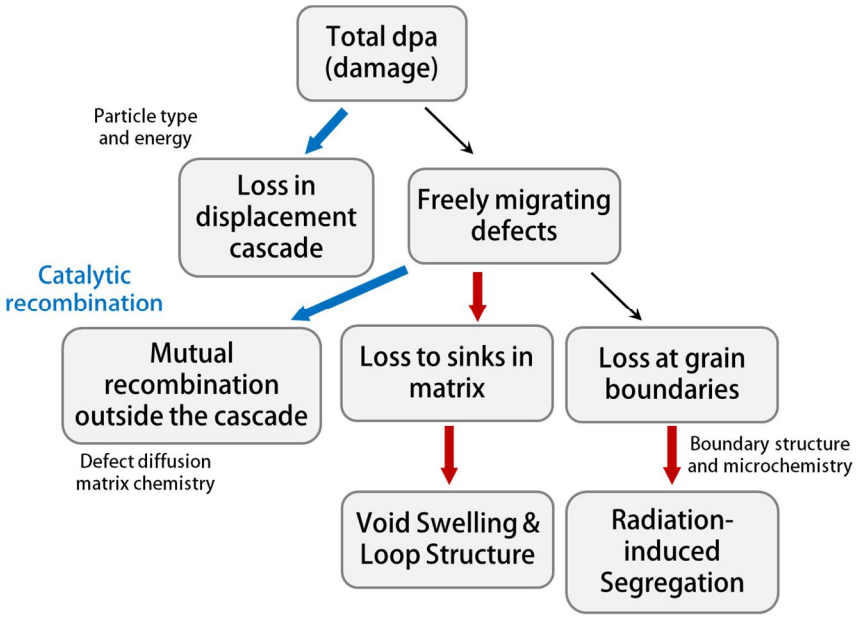

Figure 1.4 History of point defects after creation in the displacement cascade [3]. Reprinted from ref. [3] with permission through "Copyright Clearance Center".

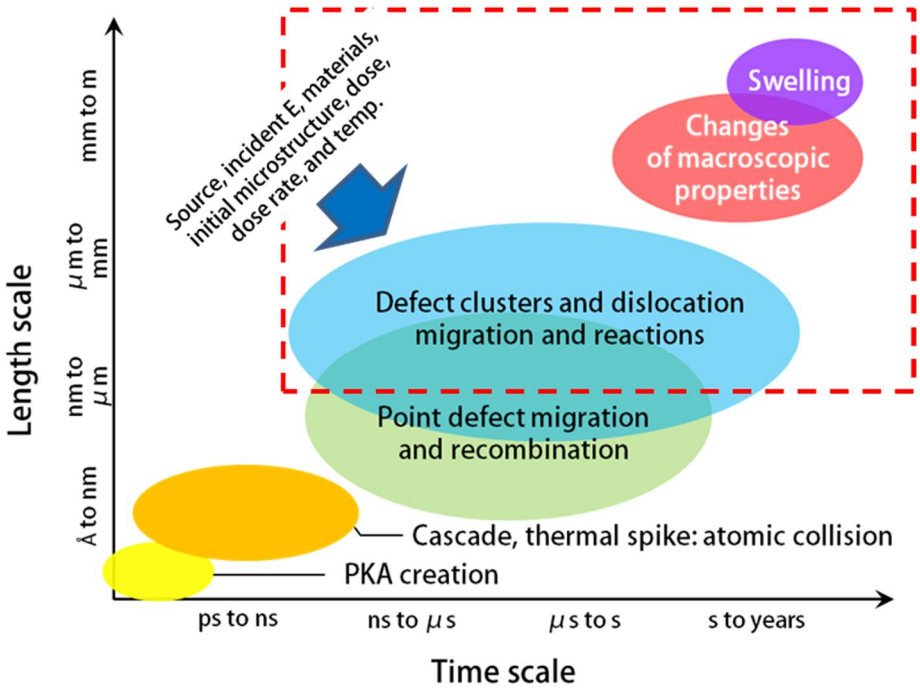

Figure 1.5 Schematic diagrams of spatial-temporal scale of radiation damage [18]. Reprinted from ref. [18] with permission through "Copyright Clearance Center".

1.2 Irradiation Environment Variables

Radiation damage is highly dependent on certain irradiation environment variables, such as the materials, incident particle, incident energy, irradiation temperature, dose, and the dose rate, among others. Here, the dependence of the incident particle type and the experimental temperature on the irradiation is discussed in detail. Additionally, the effects of the dose and the dose rate on irradiation will be studied later in Sections 5.3 and 6.6.

1.2.1 Incident Particle Type

The type of incident particle significantly affects the particle energy spectrum, the damage profile, and the cascade reaction. Figure 1.6 describes the differences in the damage morphology, displacement efficiency and average recoil energy for different types of 1 MeV particles incident on nickel. The type of incident particle affects (1) the energy spectrum, (2) the degree of asymmetry of the damage profile, (3) the penetration depth, (4) the cascade morphology, and (5) the displacement efficiency and recoil energy upon irradiation. First, the fundamental difference between ion and neutron irradiation is the energy spectrum of the particles, resulting from how the particles are produced. For instance, given that the ions are produced in an accelerator, they can be characterized by mono-energetic beams with quite narrow energy widths; however, the energy spectrum of neutrons ranges over

several orders of magnitude in terms of the energy. Secondly, the asymmetry of the profile and the penetration depth of the particles are the main differences between ions and neutrons. Figure 1.7 shows the differences in the damage profiles for 5 MeV Ni^{2+}, 3.2 MeV proton, 1 MeV neutron, and 1 MeV electron irradiation in stainless steel. Due to the high electronic energy loss, the ions lose energy quickly, resulting in a spatially non-uniform energy deposition. In addition, the penetration depth is between 0.1 and 100 μm with various ion energies. Furthermore, because neutrons are electrically neutral, they can penetrate very long distances, producing spatially flat damage profiles over the millimeter scale (Figure 1.7) [3].

Third, the difference in the cascade morphology can explain the variation in the average transferred energy and the defect production efficiency rates among different particle types. For example, light ions such as electrons and protons produce radiation damage as isolated Frenkel pairs or in small clusters, respectively, whereas heavy ions and neutrons produce large clusters, as shown in Figure 1.6. The maximum recoil energy is expressed as

$$T_{max} = \frac{4E(m_1 m_2)}{(m_1 + m_2)^2}$$

where E is the energy of the particles and m_1 and m_2 are correspondingly the mass of the target atom and that of the incident atom. Due to the individual mass amounts of incident particles, neutrons provide the highest recoil energy, followed by heavy ions, protons, and electrons in that order. In addition, the displacement efficiency, ε, is defined as the fraction of the total number of

defects produced. Numerous point defects are recombined in the cascade; therefore, the electron irradiation, which does not produce the cascade, results in the highest displacement efficiency. In contrast, the neutron irradiation producing damage in large clusters has the lowest displacement efficiency.

In this way, each type of particle irradiation results in distinct radiation damage. In order to utilize a nuclear material, neutron irradiation present in an actual reactor environment should be produced; however, this requires very expensive infrastructure, and difficulty arises when investigating radiation damage due to residual radioactivity. Thus, instead of neutron irradiation, various forms of particle irradiation have been assessed to understand the radiation effects on materials. Therefore, the pros and cons associated with electrons, heavy ions, light ions (protons), and neutron irradiation are described in Table 1.

Electron irradiation is easily realized in a TEM, a relatively simple source, and this enables us to investigate the microstructural evolution during irradiation in real time. In this regard, although electrons do not cause much radiation damage in a nuclear reactor and do not produce the cascade reaction or transmutation, electron irradiation is well utilized. Another advantage of electron irradiation is that it is an effective means of investigating radiation damage on a laboratory scale due to the high dose rate and short irradiation time, though unfortunately, because electron irradiation requires a TEM, it also has disadvantages. Initially, the energy types are limited to the accelerating voltage of the TEM. Secondly, a Gaussian beam shape in the

TEM provides a considerable gradient of the dose rate.

Due to these drawbacks, many researchers have also utilized heavy ions and proton irradiation. Heavy ion irradiation also useful due to the high doses available in short times, and it is efficient way to produce dense cascades, similar to those produced by neutrons. A shortcoming of heavy ion irradiation is that it produces short penetration depths and a strong peak damage profile, showing a continuously varying dose rate with the depth. Similar to heavy ions, protons offer accelerated dose and moderate irradiation times. Contrary to heavy ions, protons provide a flat damage profile and deeper penetration depth, similar to those of neutron irradiation; however, they also result in smaller and more widely separated cascades. These outcomes mean that related studies of various types of particle irradiation are necessary in order to mimic an actual nuclear reactor. Therefore, high-energy electron irradiation is utilized to study the defect dynamics, and heavy ion irradiation is used to investigate the effects of the dose and dose rate on the microstructural evolution in this dissertation.

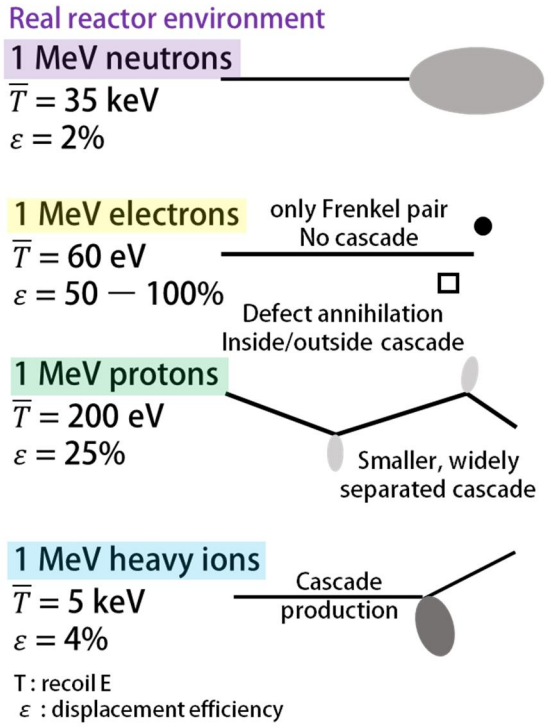

Figure 1.6 Comparison in damage morphology, displacement efficiency and average recoil energy for 1 MeV particles of different type incident on Ni [3]. Reprinted from ref. [3] with permission through "Copyright Clearance Center".

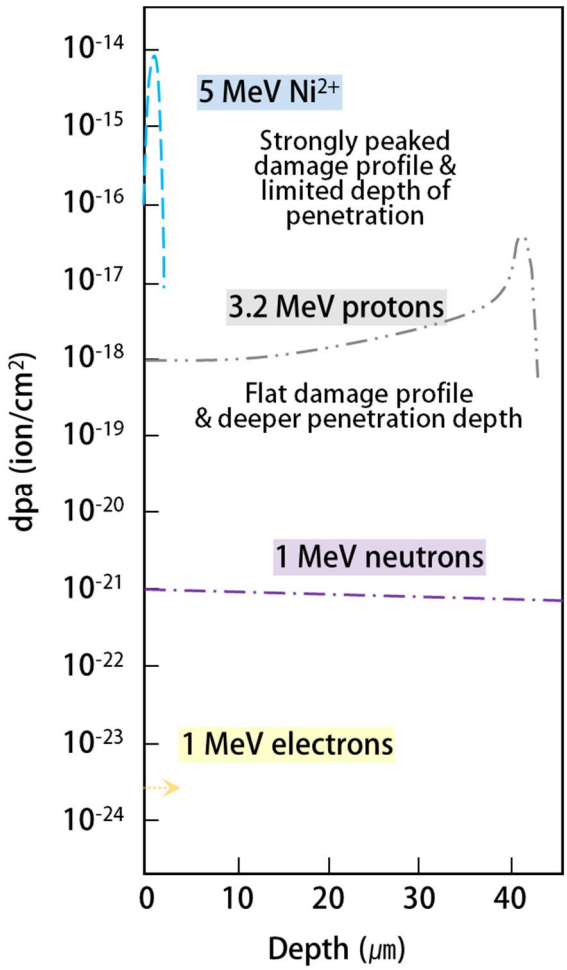

Figure 1.7 Damage profile for 5 MeV Ni^{2+}, 3.2 MeV proton, 1 MeV neutron , and 1 MeV electron irradiation in stainless steel [3, 23]. Reprinted from ref. [3] and [23] with permission through "Copyright Clearance Center".

	Advantages	Disadvantages
Neutrons	• Real reactor environment • Bulk Sample	• Very expensive infra-structure • Residual radioactivity
Heavy ions	• High dose rate — short irradiation time • Cascade production	• Limited depth of penetration • Strongly peaked damage profile • No transmutation
Protons	• Accelerated dose — moderate irradiation time • Flat damage profile • deeper penetration depth	• Smaller, widely separated cascades • Minor sample activation • No transmutation
Electrons	• Relatively 'simple' source - TEM • Using standard TEM sample • High dose rate - Short irradiation time	• Energy limitation • No cascades • No transmutation • Beam heating effect • Strong 'Gaussian' beam shape

Table 1 Advantages and disadvantages of various irradiation particle types [3, 23]. Reprinted from ref. [3] and [23] with permission through "Copyright Clearance Center".

1.2.2 Irradiation Temperature

Figure 1.8 shows typical examples of the microstructure of an irradiated material with an increase in the temperature. Considering the energy of interstitials and vacancy migration and vacancy cluster binding or dissociation, and in that complex defect clusters are rate-controlled and proportional to the melting temperature of the materials, the microstructural evolution here shows an increasing homologous irradiation temperature (T/T_M, where T_M is the melting temperature). Stage I describes the onset temperature for long-range self-interstitial-atom migration. At low temperatures below recovery stage I, point defects do not migrate and, consequently, crystalline-to-amorphous phase transitions can occur via direct in-cascade amorphization or point defect accumulation in various intermetallic and ceramic materials. Furthermore, small point defect clusters are created and diffused. At temperatures above stage I, the production of interstitial dislocation loops and other defect clusters is pronounced. Stage III corresponds to the onset temperature for monovacancy migration, and at temperatures above stage III, a cavity, solute segregation, and precipitation phenomena can be induced. Stage V indicates the onset temperature for the thermal dissolution of small vacancy clusters, and at very high temperatures, transmutant He migrates to the grain boundaries with the aid of stress.

These temperature-dependent microstructural evolution processes upon irradiation can induce various property changes in materials. The effects of

the irradiation temperature on the radiation damage correspond to the alloy design in that defects are immobile at the service temperatures discussed in Section 1.3.

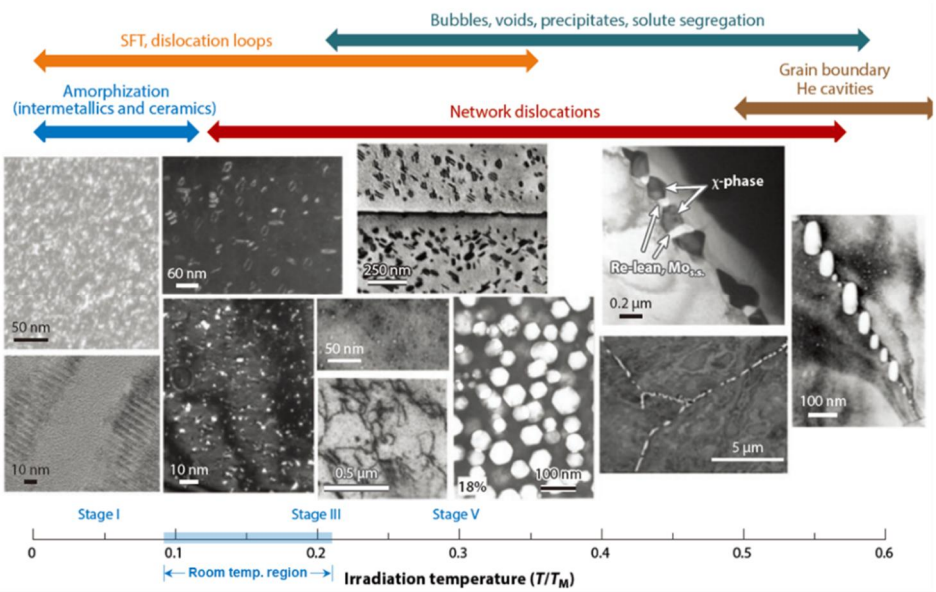

Figure 1.8 Overview of representative microstructures of irradiated material with irradiation temperature [22]. Reprinted from ref. [22] with permission through "Copyright Clearance Center".

1.3 Development of Nuclear Materials

In order to enhance the radiation resistance, various ways alloy designs have been proposed [22]. These include (1) the design of an intrinsically radiation-tolerant matrix phase, (2) the design of materials in which vacancies or interstitials are immobile at the service temperature, and (3) the design of materials with engineered high sink strengths, i.e. nano-engineered materials. The first approach to improve the radiation resistance is to choose radiation-resistant matrix phases. Generally, the efficiency of residual defect production is higher in BCC alloys compared to that in FCC alloys. In order to improve the radiation tolerance, it is important to exhibit a lower fraction of relatively large defect clusters and to gain a fine dispersion of defect clusters produced directly within energetic displacement cascades. This finely dispersed distribution of defect clusters provides effective defect recombinations upon subsequent microstructural evolution. Figure 1.9 compares the size, the number density and the distribution of visible defect clusters in BCC δ-ferrite and FCC austenitic matrixes after neutron irradiation at a low temperature. The defect clusters are relatively large and account for a low fraction in the BCC δ-ferrite compared to that in the FCC austenitic matrix. Furthermore, void swelling is an example of the clear difference in the defect accumulation between the FCC alloy and the BCC alloy when irradiated at higher temperatures. Figure 1.10 describes the void swelling behavior of 304L austenitic steel and 9-12%Cr ferritic/martensitic steel upon an increase in the

d o s e w i t h f a s t f i s s i o n r e a c t o r

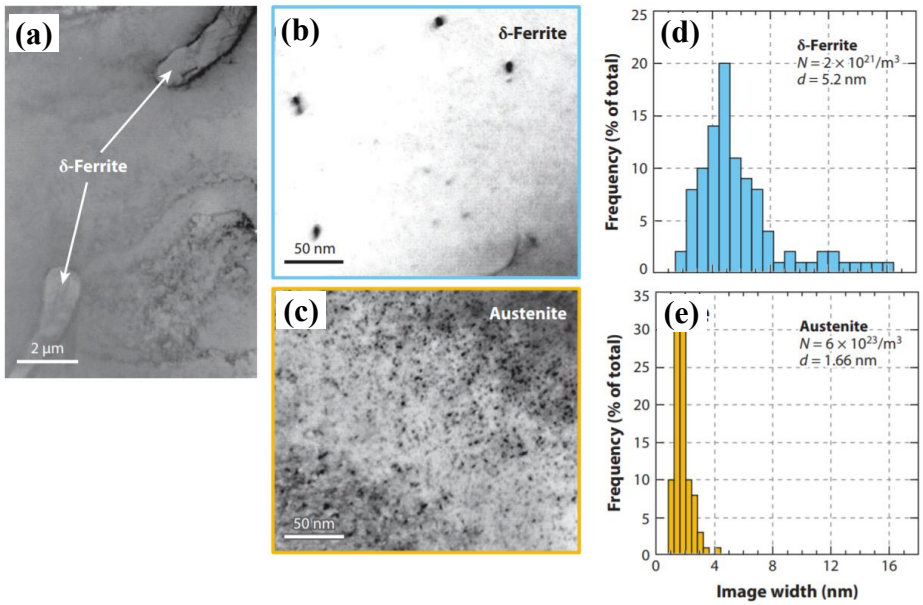

Figure 1.9 Accumulation of defect cluster in BCC vs FCC region of a type 308 stainless steel weldment after fission neutron irradiation at 120℃ to 0.065 dpa. (a) Microstructure of BCC δ-ferrite in an FCC austenitic matrix. Defect clusters in (b) δ-ferrite and (c) FCC austenitic matrix. The size distribution of dislocation loops in (d) δ-ferrite and (e) austenitic region [22]. Reprinted from ref. [22] with permission through "Copyright Clearance Center".

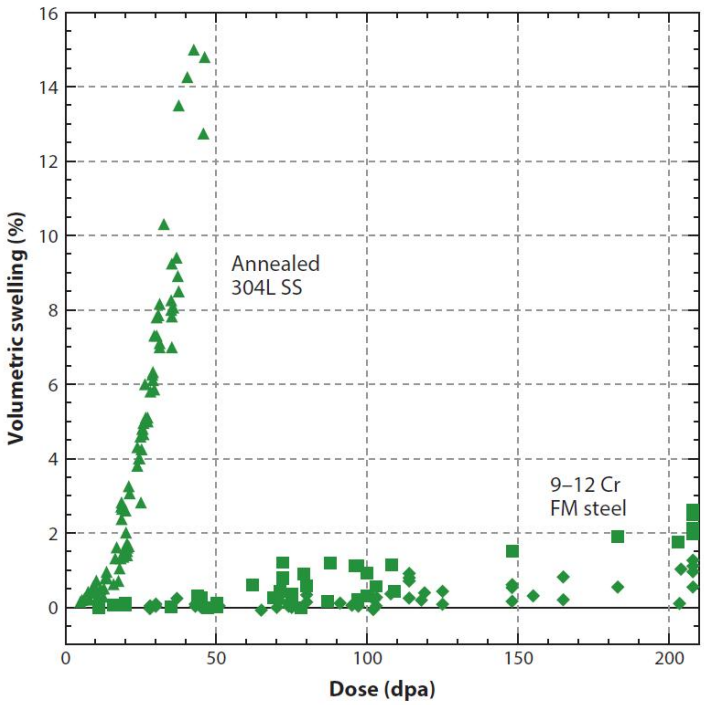

Figure 1.10 Void swelling in 304 austenitic steel and 9-12 %Cr ferritic/martensitic steel after neutron-irradiation at 400-550℃ [22]. Reprinted from ref. [22] with permission through "Copyright Clearance Center".

neutron irradiation at 400-550℃. The volumetric swelling increases sharply in the 304L austenitic steel as compared to the 9-12%Cr ferritic/martensitic steel. It is important to note that while BCC alloys generally show void-swelling resistance more than FCC metals, this behavior is not universal. Second, an alternative means of selecting materials is that to find those in which radiation-induced point defects are immobile at the service temperature. Figure 1.11(a) describes temperature-dependent saturation volumetric swelling in several materials at temperatures and doses above the critical temperature for amorphization and below the onset of void swelling. The temperature ranges are within the point-defect swelling regime in which interstitials are mobile and vacancies are immobile. Moreover, because defect migration is thermally activated and small defect clusters are dissolved, the point defect swelling decreases with an increase in the irradiation temperature for all materials presented in Figure 1.11(a). Specifically, HCP materials are characterized by high point defect swelling at a low temperature and structural anisotropy and, as a result, prominent microcracking and strength loss occur. However, Cu shows less swelling, suggesting a reduced energy barrier for point defect recombinations in metals. When applied, it shows much lower volumetric swelling rather than ceramics, suggesting that recovery stage I is exceeded to avoid amorphization in ceramics and intermetallics whereas it is below stage III to prevent the occurrence of a void-swelling regime. Figure 1.11(b) presents the temperature regime above stage I and below stage III for these materials, and it is possible to select a material in which point defects

are sessile at the operation temperature. Thus, the irradiation temperature during operation should be above recovery stage I and below stage III in order to avoid amorphization and a void-swelling regime. Lastly is the design of materials with engineered high sink strength levels that are nano-engineered. Figure 1.12(a) shows snapshot images of a collision cascade near a ∑11 <110>{133} symmetric tilt grain boundary in fcc Cu at 300 K as calculated from an MD simulation [15]. The color of the atoms indicates their potential energy, and atoms with energies higher than 3.43 eV are considered as defective. (A) When a PKA with 4 keV of kinetic energy goes directly toward the grain boundary plane, a collision cascade is initiated. Interstitials and vacancies are formed as irradiation damage, and they can be healed as the form of defect recombinations and by annihilation. (B) At 0.5 ps, the cascade reaches its maximum size. (C) Additionally, after ~ 10 ps, the cascade reaction is nearly done and most displaced atoms relocate to crystal lattice sites, but others lead to the formation of interstitials and vacancies. Thus, the boundary provides defect sinks such that the irradiation resistance can be largely enhanced, as shown in Figure 1.12(b). As expected, in Figure 1.12(a-C), the interstitial move quickly to the surface and not the vacancies in most metals, resulting in swelling, after which the vacancies that are left behind agglomerate, forming immobile voids and giving rise to embrittlement (Figure 1.12(b)). In the nanostructured material, the interstitial defects become stuck at the boundaries and virtual interstitials are re-emitted from the boundaries, indicative of defect healing. The healing of defects at the boundary is closely

related to the mechanical response of the

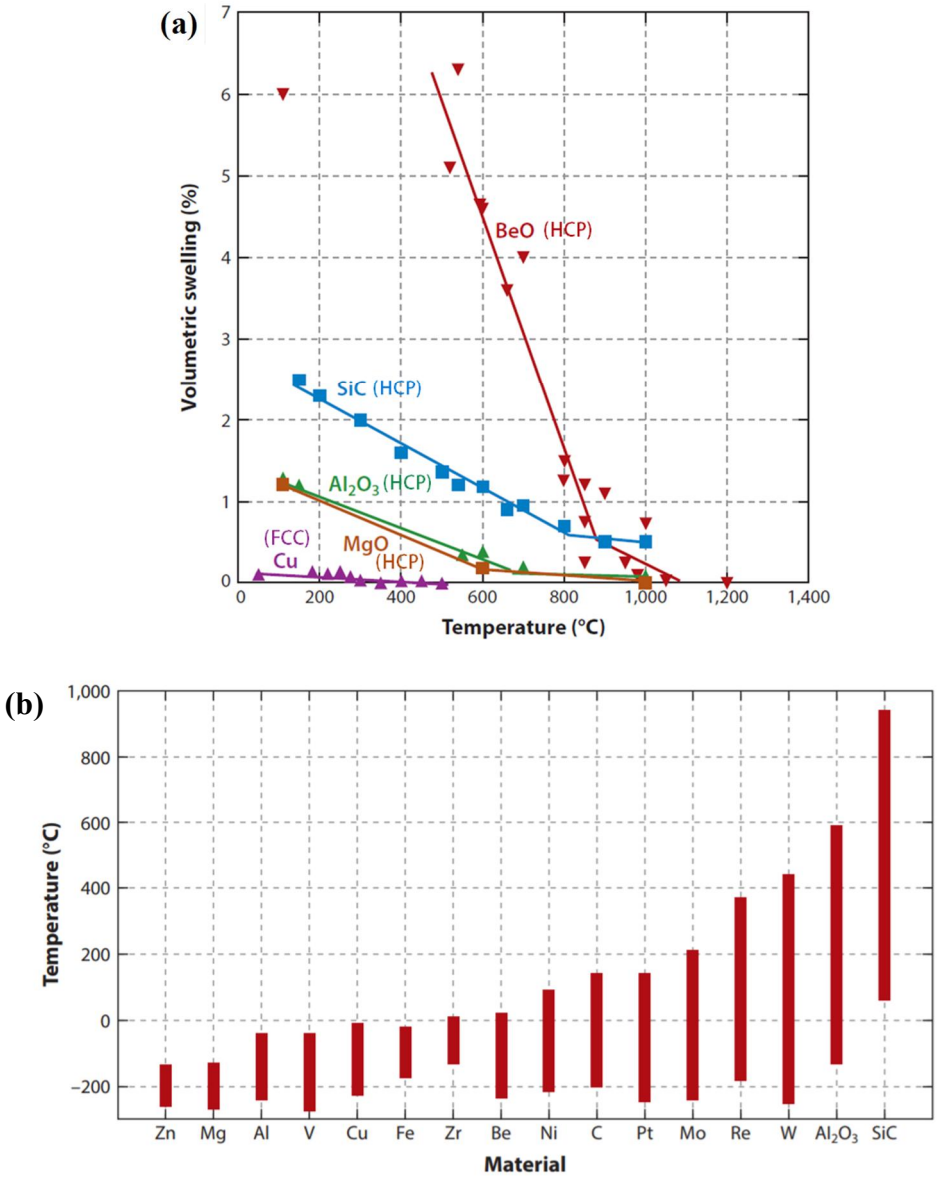

Figure 1.11 (a) Void swelling behavior in irradiated metals and ceramics and (b) temperature intervals associated with onset of interstitial migration (defect recovery above Stage I) and prior to vacancy migration (below Stage III) in selected materials [22]. Reprinted from ref. [22] with permission through "Copyright Clearance Center".

upon irradiation. Thus, the effect of the radiation sink strength on the radiation hardening is investigated upon fission neutron irradiation near 300℃ [22] (Figure 1.13). The sink strength in Figure 1.13 refers to the affinity of a sink for defects [23]. The mechanical properties are mostly not associated with the sink strength up to ~10^{16} /m^2; however, this depends on the sink strength at very high levels. Hence, the degradation of the mechanical properties under irradiation can be suppressed via the manipulation of the sink strength.

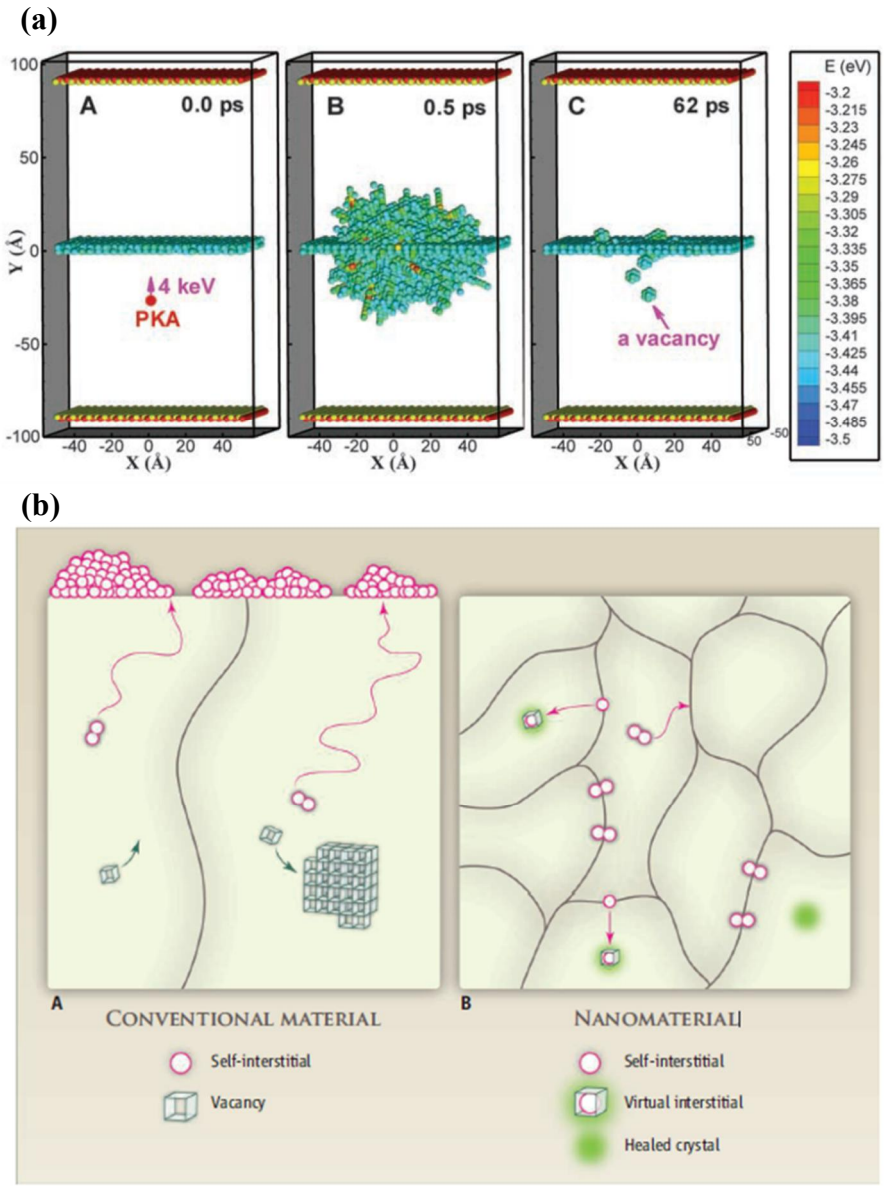

Figure 1.12 (a) Representative snapshots of a MD simulation of a collision cascade near grain boundary at 300 K [15]. (b) Conceptual image of agglomeration, movement, healing in conventional material and nanomaterial upon irradiation [31]. Reprinted from ref. [15] and [31] with permission from "AAAS".

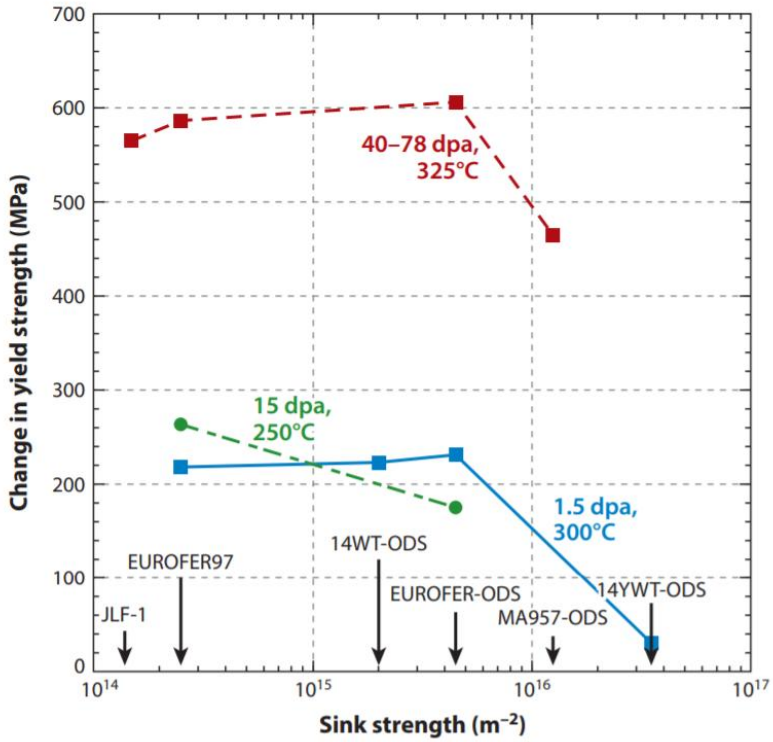

Figure 1.13 Effect of initial sink strength on the radiation hardening of steels following fission neutron irradiation near 300◦C to damage levels of 1.5 to 78 displacements per atom (dpa). Materials include conventionally fabricated low-activation ferritic/martensitic steels (the Japanese low-activation ferritic JLF-1 and EUROFER) and several oxide dispersion–strengthened (ODS) steels fabricated by using powder metallurgy processes [22]. Reprinted from ref. [22] with permission through "Copyright Clearance Center".

1.4 Core Effects of High Entropy Alloy

This dissertation focuses on new alloy systems that can utilize radiation-resistant matrixes with slow defect mobility at specific temperatures, as discussed in Section 1.3. Specifically, high-entropy alloys (HEAs), potential candidates for a radiation-resistant matrix, are defined as multi-component alloy systems with similar atomic percentages, showing maximized configurational entropy levels. This alloy design also has a high entropy effect, a lattice distortion effect, a sluggish diffusion effect, and a cocktail effect. In this section, these characteristics of HEAs are discussed in detail.

1.4.1 High Entropy Effect

According to the Gibbs phase rule, the number of phases (P) in an alloy is determined in a constant pressure in equilibrium condition by

$$P=C+1-F$$

where C is the number of components and F is the maximum number of thermodynamic degrees of freedom in the system. For example, a five-component system at a given pressure level is expected to have a maximum of six equilibrium phases during an invariant reaction; however, HEAs have a solid solution rather than showing intermetallic or intermediate compounds. Furthermore, according to $\Delta G_{mix}=\Delta H_{mix}-T\Delta S_{mix}$, HEAs can be more stable

even at elevated temperatures, suggesting high temperature stability [30, 42].

However, upon an increase in the number of alloy elements, solid-solution alloys are less likely in practice, indicating a contradiction between the premise and the experiment [3]. Figure 1.14 shows the distribution of a multi-principal component alloy with an increase in the number of alloy elements at 600℃ with melting temperature T_m via a computation screening method. Here, the alloy systems in this study are classified into SS alloys that consist of more than one solid solution (SS), IM alloys containing more than one intermetallic compound (IM), and (SS+IM) alloys including both SS and IM phases. In order to improve the reliability, a binary system for which the thermodynamic database is fully described is only considered to calculate the phase diagram. As shown in Figure 1.14, as the number of alloy components increases, the fraction of (SS+IM) alloys increases while the fractions of SS alloys and IM alloys decrease at both 600℃ and T_m due to the competition between configurational-entropy-favoring SS alloys and formation-enthalpy-favoring IM alloys. Additionally, the majority of SS alloys are of the single-phase type, and among the multi-phase alloys, the fraction of (SS+IM) alloys is highest. The fraction of SS alloys decreases sharply and the fraction of the IM alloys increases; however, the fraction of (SS+IM) alloys remains nearly unchanged from T_m to 600℃. Furthermore, the trends of the fractions of multi-component alloy systems are similar to the numbers of alloy elements at T_m and 600℃.

To summarize, this inconsistency between the premise, i.e., a ‘high

entropy effect', and the experiment is attributed to the fact that while the probability that at least one pair of elements prefers intermetallic compounds to rise more rapidly, the configurational entropy increases slowly with an increase in the number of alloy constituents.

1.4.1 Lattice Distortion Effect

Generally, solid-solution hardening is described as the interaction between randomly dispersed substitutional solute atoms and dislocations through misfits in the atomic size and elastic modulus of the solute and solvent atoms. Because lattice distortion serves as an energy barrier against dislocation motion due to the random fluctuation distortion in the alloys, it is an important parameter for describing solid-solution hardening. For this reason, the lattice distortion effect in HEAs was initially investigated using peak intensity changes in the XRD pattern [20]. Figure 1.15 shows schematic diagrams of Bragg diffraction on (a) a perfect lattice with a single type of alloy element and (b) a distorted lattice with various alloy components. Additionally, Figure 1.15(c) describes the effects of the temperature and lattice distortion on the peak intensity of the XRD pattern. The intrinsic lattice distortion effect caused by the addition of multiple-alloy elements causes an anomalous decrease in the peak intensity of the XRD pattern. Unfortunately, this somewhat qualitative method is not sufficient to gain a full understanding of the lattice distortion effects in HEAs. Thus, alternative approaches are

needed to investigate the relationship between the lattice distortion and strength levels in HEAs [26]. First, the solute-dislocation

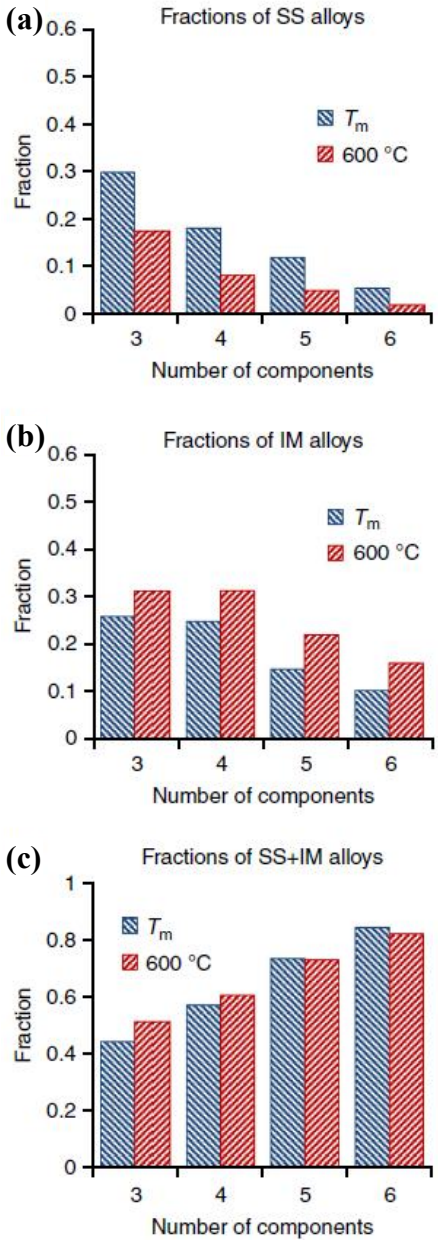

Figure 1.14 Distributions of multi-principal element alloys categorized by SS, IM, SS+IM alloys. Fractions of (a) SS, (b) IM, (c) (SS+IM) equiatomic alloys in 3- to 6-component alloy at melting temperature T_m and 600℃. Here, SS alloys and IM alloys mean solid solution alloys and intermetallic alloy, respectively [17]. Reprinted from ref. [17] with permission through "CC BY 4.0".

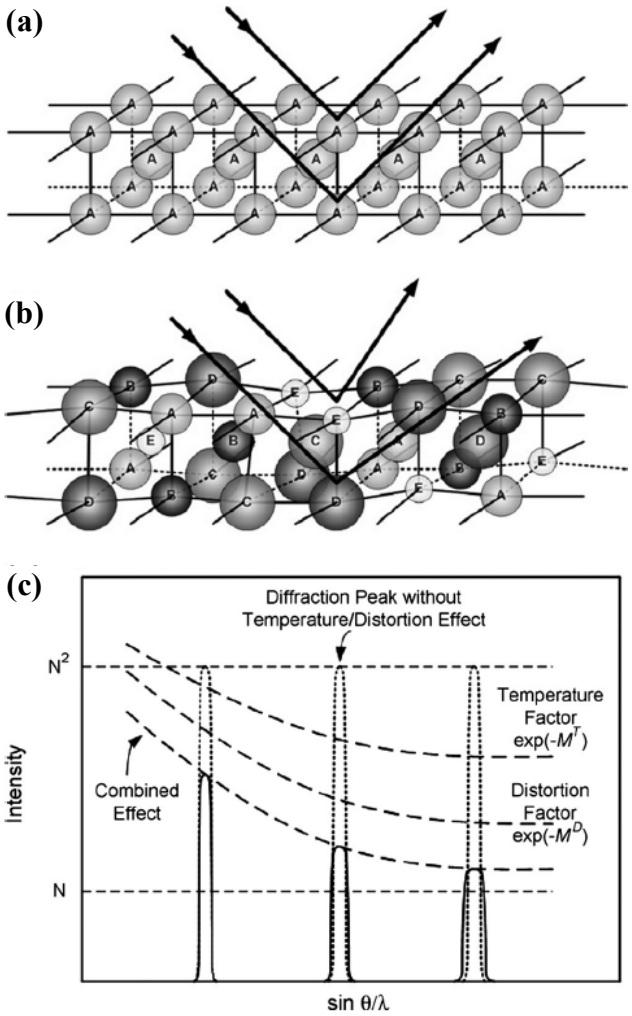

Figure 1.15 Schematic diagram considering the lattice distortion effects on Bragg diffraction: Bragg diffraction on (a) perfect lattice with same alloy elements (b) distorted lattice with different type of alloy elements, and (c) effect of temperature and lattice distortion on the peak intensity of XRD [20]. Reprinted from ref. [20] with permission through "Copyright Clearance Center".

interaction energy can be calculated to describe solid-solution hardening. In dilute alloys, a solute atom is surrounded by solvent atoms and, as a result, a spherically symmetric strain field is formed around the solute atom due to the atomic size misfit. However, in concentrated alloys, i.e., HEAs, solute and solvent atoms are not clearly defined and, consequently, an asymmetric strain field arises. This makes it difficult to calculate the 'solute-dislocation interaction energy' directly in HEAs. A secondly way is to calculate the average atomic displacement in the alloys. When the solute-dislocation interaction energy is calculated in dilute alloy systems, it is assumed that the spherically symmetric strain field leads to displacement of the solvent atoms from the ideal lattice positions. Thus, the average atomic displacement is expected to increase with an increase in the solute concentration. The mean-square atomic displacement (MSAD) values of individual alloy elements for five different quaternary HEAs are shown in Figure 1.16(a) , as derived by first-principles total-energy calculations for special quasi-random structures (SQSs) with 5x4x4 and 4x4x4 FCC supercells [26]. Despite the use of identical alloy elements, the MSAD values are affected by the alloy systems. This suggests that the lattice distortion is likely to be influenced by not only the radius of an individual atom but the combination of alloy elements. These lattice distortions are important with regard solid-solution strengthening. Figure 1.16(bshows the correlation between the yield strength normalized by the shear modulus at 0 K and the average MSAD values in the quinary CrMnFeCoNi HEA and its derivative ternary and quaternary alloy. The

normalized yield strength is linearly described by the square root of the average MSAD values, suggesting possibility of the average MSAD as a scaling factor to predict the athermal stress. As described in Figure 1.16(a), the lattice distortion is dependent on the radius of the alloy elements as well as on the environment for the alloy elements. This indicates that the description of the lattice distortion according to the mean value is not enough. From this standpoint, the standard deviation should be applied for a further investigation of the lattice distortion in HEAs [28].

Thus, it was reported that element-resolved lattice distortions were investigated via EXAFS measurements and electronic structure calculations [28]. An undistorted ideal FCC lattice is introduced as the reference structure in order to quantify the experimentally and theoretically extract the bond length variations. Figure 1.17(a-b) shows the projection of the employed SQS supercells onto the (100) planes and a lattice distortion histogram of Mn bonds in CrMnFeCoNi HEA as calculated by the first-principles method. While the mean distortion is comparably small (<0.5%), the fluctuation, i.e., the standard deviation of the individual bond lengths, is significant (≈2%), as shown in Figure 1.17(b). Figure 1.17(c) describes the mean bond distortions and corresponding standard deviations between the elements, indicating the incredible fluctuation of each bond length between the other elements compared to the small amount mean bond distortion. Specifically, Figure 1.17(c) shows that Cr and Mn result in strong local bond fluctuations among themselves, similar to Cr-Cr, Cr-Mn and Mn-Mn bonds and in combinations

with the other elements. Because the local bond fluctuation can affect the dislocation-solute interaction energy levels, it makes the solid-solution hardening much stronger than the actual mean bond distortions.

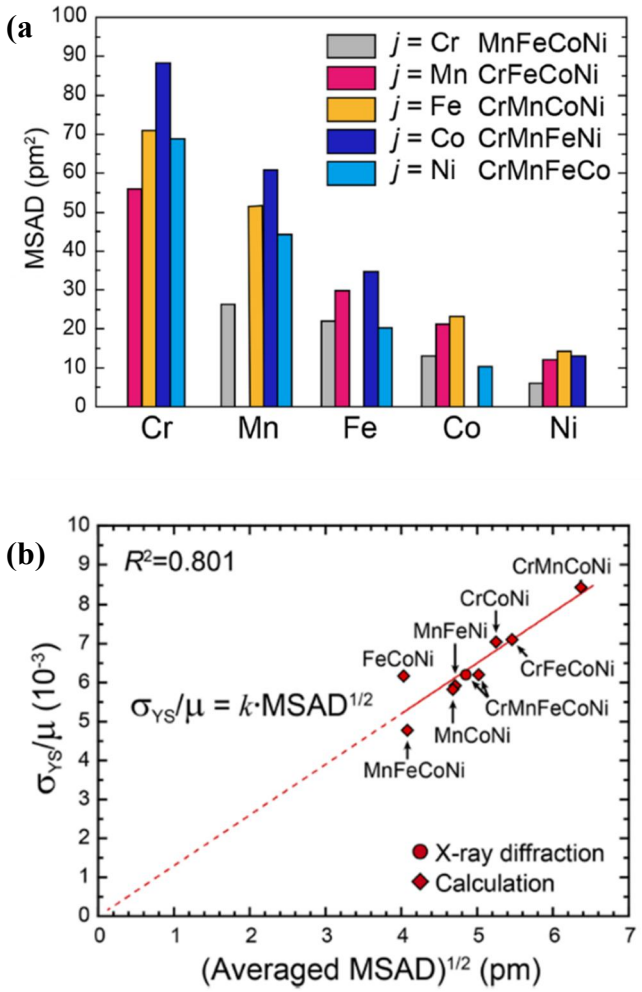

Figure 1.16 (a) MSADs of individual alloy component for five different quaternary HEA obtained by first-principles total-energy calculations for SQSs with the 5x4x4 and 4x4x4 FCC supercells, respectively. (b) The correlation between the yield strength at 0 K normalized by shear modulus and calculated mean-square atomic displacement (MSAD) of individual alloys [26]. Reprinted from ref. [26] with permission through "CC BY 4.0".

(a)

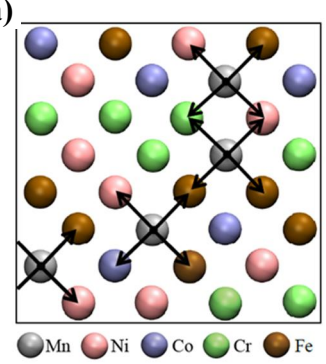

(b)

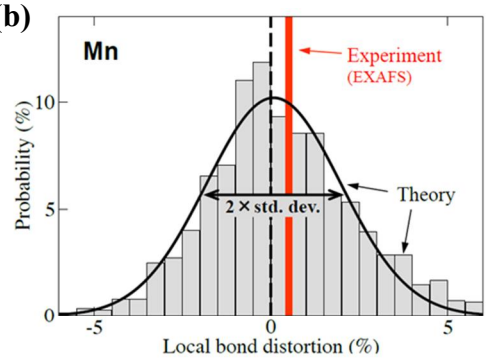

(c)

Mean distortion (in %)

	Fe	Co	Ni	Cr	Mn
Fe	0.34	-0.72	-0.06	0.18	0.22
Co	-0.72	-0.43	-0.08	-0.67	-0.22
Ni	-0.06	-0.08	0.04	0.02	0.12
Cr	0.18	-0.67	0.02	0.66	0.54
Mn	0.22	-0.22	0.12	0.54	0.71

Standard deviation (in % of distortion)

	Fe	Co	Ni	Cr	Mn
Fe	1.58	1.21	1.15	2.09	1.99
Co	1.21	1.14	1.03	1.88	1.40
Ni	1.15	1.03	0.89	1.38	1.16
Cr	2.09	1.88	1.38	3.06	3.01
Mn	1.99	1.40	1.16	3.01	2.74

Figure 1.17 (a) Projected the employed special quasi-random structure (SQS) supercells onto the (100) planes. The black arrows indicate the nearest neighbor bonds for the Mn atoms, which is utilized to extract the distribution of the local bond distortion shown in (b). (b) The lattice distortion histogram of Mn-bonds in CrMnFeCoNi via the first-principle calculation. The theoretical results are further fitted by Gaussian function and the red solid line indicates the experimentally-measured average distortion. (c) Mean bond distortion and standard deviation between alloy elements in the CrMnFeCoNi HEA [28]. Reprinted from ref. [28] with permission through “CC BY 4.0”.

1.4.2 Sluggish Diffusion Effect

The sluggish diffusion effect was originally introduced to explain nano-precipitation in HEAs upon solidification. Figure 1.18 presents a bright-field (BF) TEM image of the as-cast AlCrFeCoNiCu HEA, showing a fairly complex microstructure [27]. In detail, the HEA consists of an inter-spinodal plate with a disordered BCC phase (A2) and a spinodal plate with an ordered BCC phase (B2) that, interestingly, contain nano-precipitates of different sizes. Due to the lattice distortion, the delayed atomic movement during the phase transformation process leads to this type of nano-precipitation in HEAs. This qualitative explanation of sluggish diffusion in HEAs has motivated many researchers to attempt to investigate the diffusion in HEAs.

Due to the various atomic-scale chemical environments in HEAs, the interaction energy state, referred to as the seven-bond interaction energy (SBIE) state, can vary at individual lattice sites, as indicated by the number of bars in Figure 1.19(a), which are significant greater in number in the $CrMn_{0.5}FeCoNi$ HEA than ternary alloys [13]. Specifically, the diffusion barrier in a multi-component system should be considered as structurally (1) the lattice distortion strain energy and (2) the packing density and thermodynamically (3) as the cohesive energy corresponding to the vacancy formation and atomic movement processes [35]. These contributions to diffusion in multi-component systems are investigated in detail below. First, the lattice distortion strain energy ΔU_{strain} is calculated by

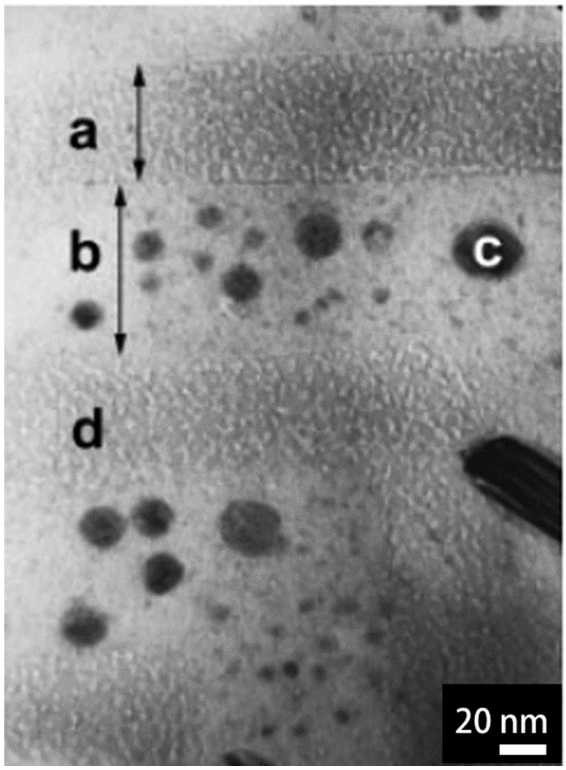

Figure 1.18 Bright field (BF) image of as-cast AlCrFeCoNiCu HEA consisting of an ineterspinodal plate with a disordered BCC phase and nano-precipitation in the interspinodal plate in region (a) and spinodal plate with an ordered BCC phase and nano-precipitation with FCC phase in a spinodal plate in region (b) [27]. Reprinted from ref. [27] with permission through "Copyright Clearance Center".

$$\Delta U_{strain} = (\bar{E}\delta)(2\bar{r})^2\bar{d}$$

$$\delta = \sqrt{\sum_{i=1}^{n} X_i \left(1 - \frac{r_i}{\bar{r}}\right)^2}$$

where δ is the lattice distortion with X_i as the fraction of the *i*th component and r_i and $\bar{r}$ are the *i*th and the average atom radii, respectively. $\bar{E}$ is the average modulus and $\bar{d}$ is the average displacement of atoms $\left(\bar{d} = \delta\bar{r}\right)$. With an increase in the number of alloy elements, the lattice strain energy increases with few inconsistencies for the quaternary and quinary alloys. Secondly, the cohesive energy Ω_{ij} of the *i*th and *j*th components is determined by Miedema's thermodynamic model

$$\Omega_{ij} = \frac{\Omega_{ii} + \Omega_{jj}}{2} - \Delta H_{ij}^{mix}$$

Therefore, the cohesive energy increases with the number of alloy elements, indicating the suppression of bond breaking for vacancy formation and atomic movement. Lastly, in multi-component systems, the packing density increases due to the mixing of various sizes of alloy elements. By considering the contributions of the lattice distortion strain energy, cohesive energy, and packing density, the activation energy for diffusion can be calculated as follows,

$$\Delta Q = \left(\Delta U_{strain} + \Delta H^{mix}\right)\frac{S'}{S}$$

where S and S' denote the packing density and the size-dependent density, respectively. As a result, when the number of alloy elements increases, the

activation energy for diffusion also rises, suggesting slower diffusion in HEAs.

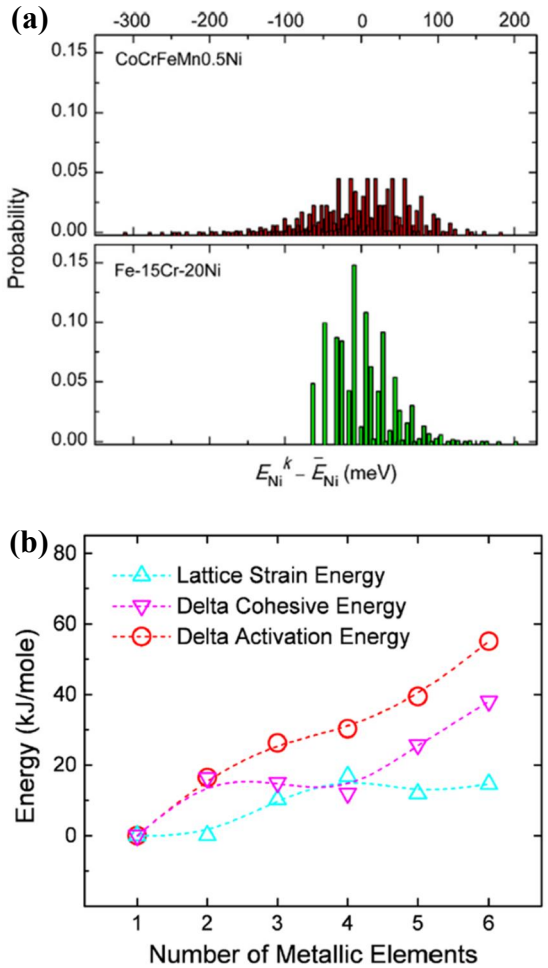

Figure 1.19 (a) Probability distributions of seven bond interaction energy (SBIE) for Ni in $CrMn_{0.5}FeCoNi$ HEA and Fe-15Cr-20Ni alloy.[13] Reprinted from ref. [13] with permission through "Copyright Clearance Center". (b) Calculated lattice distortion strain energy, cohesive energy and activation energy for Cu diffusion in/through nA alloys (n: number of alloy elements) [35]. Reprinted from ref. [35] with permission through "CC BY-NC-ND 3.0".

However, because the activation energy for diffusion is not compared with the experimental case and given that numerous assumptions are used when calculating the barrier, these results appear slightly ambiguous. Therefore, the experimentally obtained energy barrier for diffusion should be investigated in HEAs.

The diffusion coefficients of the individual alloy elements in CrMnFeCoNi HEA are measured using a diffusion couple. The diffusion coefficients are determined with the temperature and then the activation energies for diffusion are calculated using

$$\mathrm{D} = D_0 exp\left(-\frac{Q}{RT}\right)$$

where Q is the activation energy for diffusion and D_0 is a pre-exponential factor in each case. The activation energy is normalized by the melting temperature T_m for the diffusions of Cr, Mn, Fe, Co and Ni in different pure metals and alloys, as shown in Figure 1.20 [13]. To investigate the sluggish diffusion in HEAs, the diffusion coefficients of individual alloy elements in the CrMnFeCoNi HEA are compared with those in pure Fe, Co, Ni, and in Fe-15Cr-20Ni, Fe-15Cr-20Ni-Si, and Fe-15Cr-45Ni, and Fe-22Cr-45Ni alloys. Among the pure metals and alloy systems in this study, the Q/T_m values in the CrMnFeCoNi HEA are the highest, providing direct evidence of sluggish diffusion in HEAs. From these results, a schematic diagram of the variations of the lattice potential energy (LPE) and the mean differences (MDs) during the migration of an atom in pure metal and in the Fe-Cr-Ni and

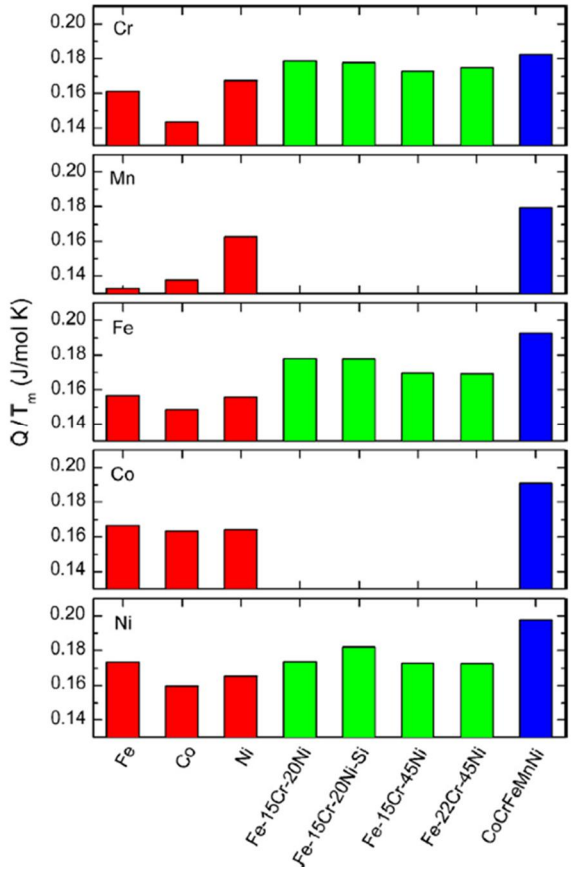

Figure 1.20 Normalized activation energies of diffusion for alloy elements like Cr, Mn, Fe, Co and Ni in different pure metals and alloys [13]. Reprinted from ref. [13] with permission through "Copyright Clearance Center".

HEA systems are presented in Figure 1.21. Due to the single-bond configuration in the pure metal, the MD would be zero; however, because the LPE values of the two lattice sites L and M are different for alloys, the values of the energy barrier E_b for two atomic jumps with opposite directions are different. Thus, lattice sites with low LPE values provide atomic traps to prevent diffusion. This means that the large fluctuation in LPE results in stronger trapping sites and a lower diffusion rate in the HEA. Furthermore, because vacancy formation and migration enthalpies are related to local atomic interactions, they are different from one lattice to another. Thus, changes in the LPE can cause variations in the diffusion kinetics.

The cocktail effect in the core and how it affects HEAs implies that the alloy properties can change significantly with composition changes and changes in the alloying conditions [20]. Unfortunately, this concept has been controversial and, therefore it is omitted in this dissertation. Instead, the irradiation behavior of the FCC HEA, corresponding indirectly to the aforementioned sluggish diffusion, is primarily covered in this dissertation.

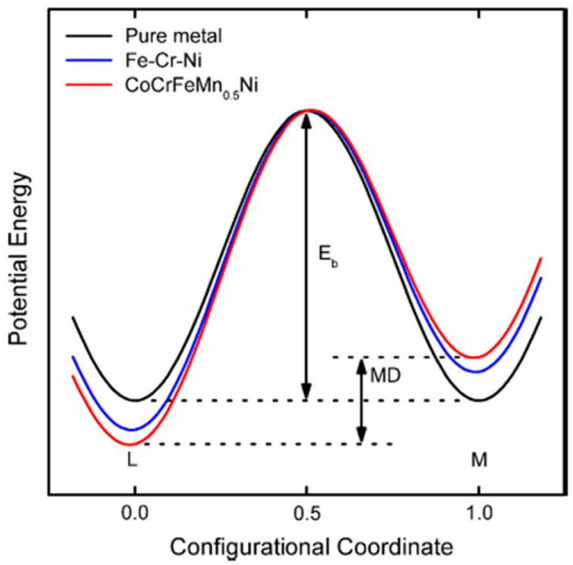

Figure 1.21 Schematic diagram of the variation in LPE and mean difference (MD) during the migration of an atom in pure metal, Fe-Cr-Ni and $CrMn_{0.5}FeCoNi$ HEA. E_b is energy barrier for a migration [13]. Reprinted from ref. [13] with permission through "Copyright Clearance Center".

Chapter 2. Experimental Procedure

2.1 Sample preparation

2.1.1 Casting and Post Processing

Ingots were prepared by arc melting high purity Cr(99.99%), Fe(99.99%), Co(95.95%), Ni(99.99%) and Cu(99.99%) under a Ti-gettered Ar atmosphere. The ingots were then melted at least five times to improve homogeneity under high vacuum using arc-melting apparatus (SAMHAN vacuum development Co. Ltd.; Figure 2.1(a)) After that, ingots were suction cast into a water-cooled copper mold to obtain plate type of 2.5 mm x 6 mm x 50 mm. As-cast $Cr_{20}Fe_{20}Co_{20}Ni_{20}Cu_{20}$ HEA was homogenized at 1100℃ for 24 hours in Ar atmosphere, followed by furnace cooling using furnace with gas purifier and gas flow controller (Figure 2.2). Furthermore, $Cr_{24}Fe_{25}Co_{24}Ni_{22}Cu_5$ alloys were suction cast, cold-rolled to 50%, and annealed at 1000℃ for 24 h with water quenching (Figure 2.1(b-c)).

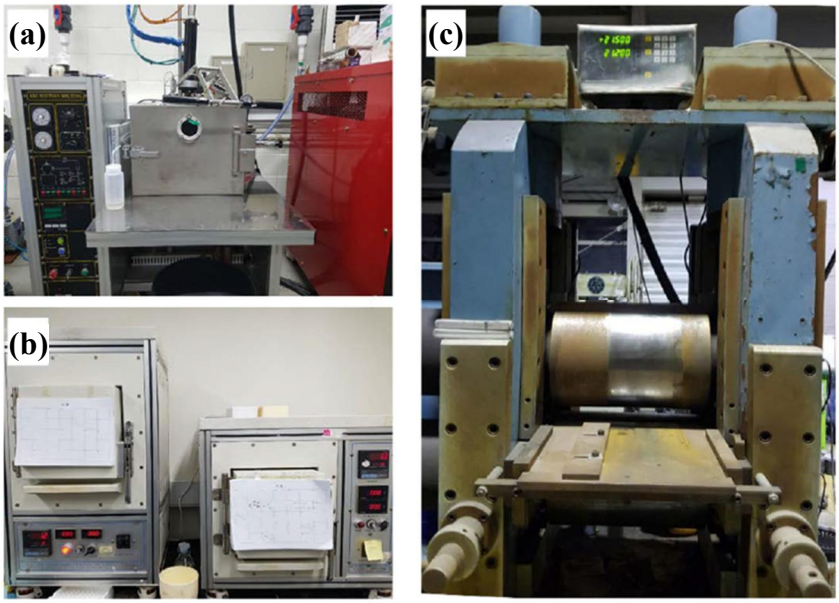

Figure 2.1 An overview of equipment for sample preparation. (a) The arc-melting instrument, (b) box-furnace, and (c) rolling machine.

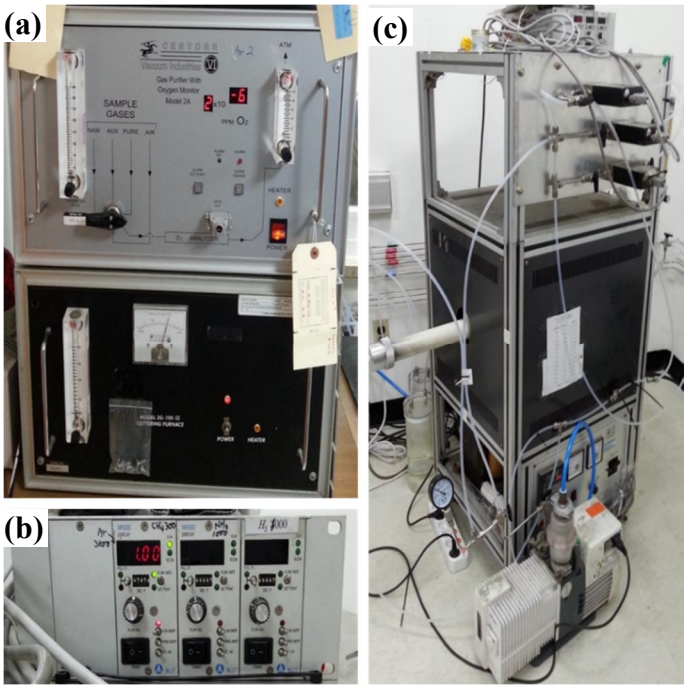

Figure 2.2 Furnace instruments for the homogenization process. (a) The gas purifier, (b) the gas flow controller (MFC) and (c) the furnace in KIST.

2.1.2 TEM Sample Preparation

Thin foils of $Cr_{20}Fe_{20}Co_{20}Ni_{20}Cu_{20}$ alloy for TEM were fabricated using a dual-beam focused ion beam (FIB) (Thermo-Fisher Scientific; Helios Nanolab 600). PIPS and electro-jet polishing were also tried but, Cu-rich phase are disappeared during milling or the thickness of TEM samples was so thick to be difficult to observe the microstructure due to faster milling rate of Cu. To avoid the Ga^+ ion damage, low energy cleaning was performed at 5 kV of accelerating voltage in FIB. Besides, the TEM samples of single phase $Cr_{24}Fe_{25}Co_{24}Ni_{22}Cu_5$ alloys were prepared by double-sided milling at 3.5~4.0 keV acceleration voltage using PIPS (Gatan; PIPS I 691).

Furthermore, cross-sectional view and plane view TEM samples were also prepared using the dual-beam FIB (Thermo-Fisher Scientific; Helios Nanolab 600). Especially, the plane view TEM sample preparation was described as below (Figure 2.3). Firstly, the region of interest (ROI) was selected and then, the Pt layer was deposited on the ROI, protecting the original surface during subsequent FIB imaging and milling. To remove the ROI from the bulk, an 'invert barn' shape is FIB milled free of the surrounding material. Then, the lift-out technique was used to remove the 'barn' and after 90° rotation of the sample holder using tilt holder placed it on a grid, showing the side of barn was placed up. The Pt protective layer was deposited again on top area of barn shaped sample and the sample was further milled as a form of lamellar. And then, final thinning then was performed for

electron transparency.

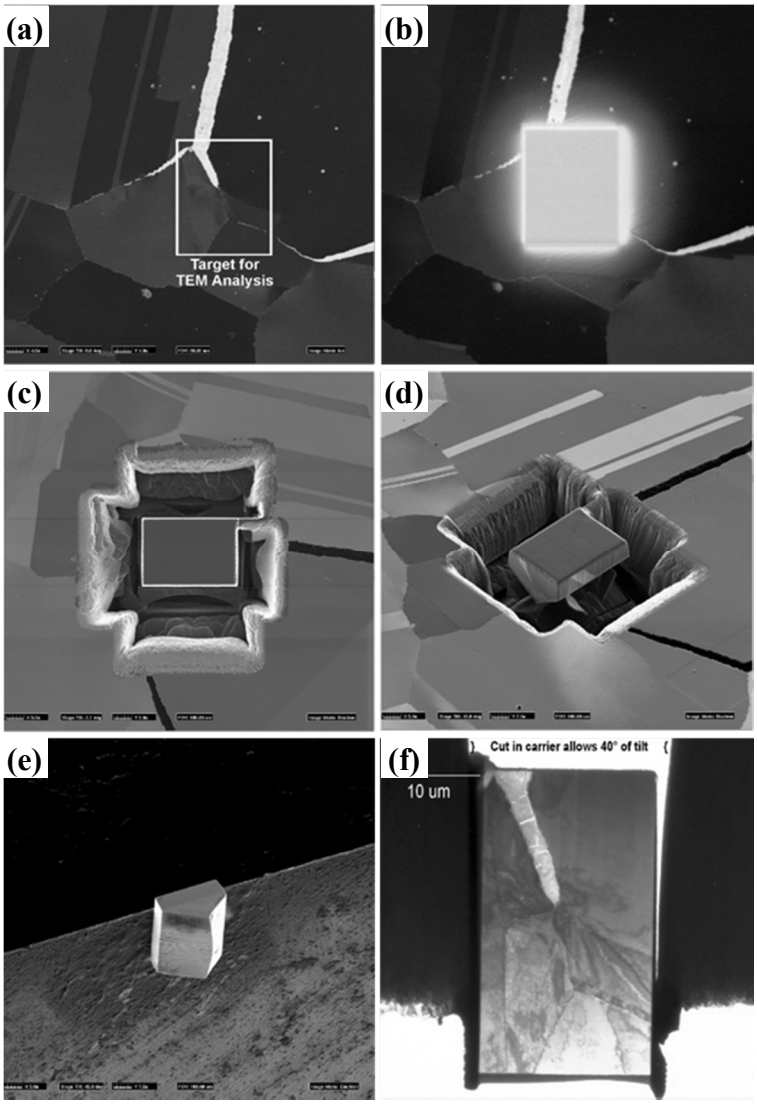

Figure 2.3 Plane view sample preparation using FIB. (a) Area selection. (b) Pt deposition over the region of interest as a protective layer. (c) Top views and (d) off-axis views of the sample milled free of the surrounding material after the trench and U-cut. (e) Attachment of the sample on the grid. (f) Fine milling for electron transparency [25].

2.1.3 Sub-micron Pillar Fabrication

The dual-beam FIB was also used to fabricate STEM-EDS tomography sample and the sub-miron sized pillar for compression. Firstly, electron back-scattered diffraction (EBSD) (Oxford; CHANNEL5) was performed. Secondly, for STEM-EDS tomography, (122) plane for rolling direction (RD) was selected to get the images at (100), (110) and (111) planes by tilting (Figure 2.4(a-b)). Additionally, for compression pillar test, (100) plane for normal direction (ND) was chosen. Thirdly, the lamellar with specific crystallographic orientation was picked up, transferred and attached on the Mo grid (Figure 2.4(c)). Furthermore, it was milled with cylindrical shape (Figure 2.4(d)), performing the multi-step milling with the subsequent decrease in beam current and the pillars were finally fabricated (Figure 2.4(e)). For compression pillar test, cylindrical shaped micro-pillars were prepared in ~ 380 nm for diameter and ~ 2 μm for height with ~5.2 aspect ratio and 3° for taper angle.

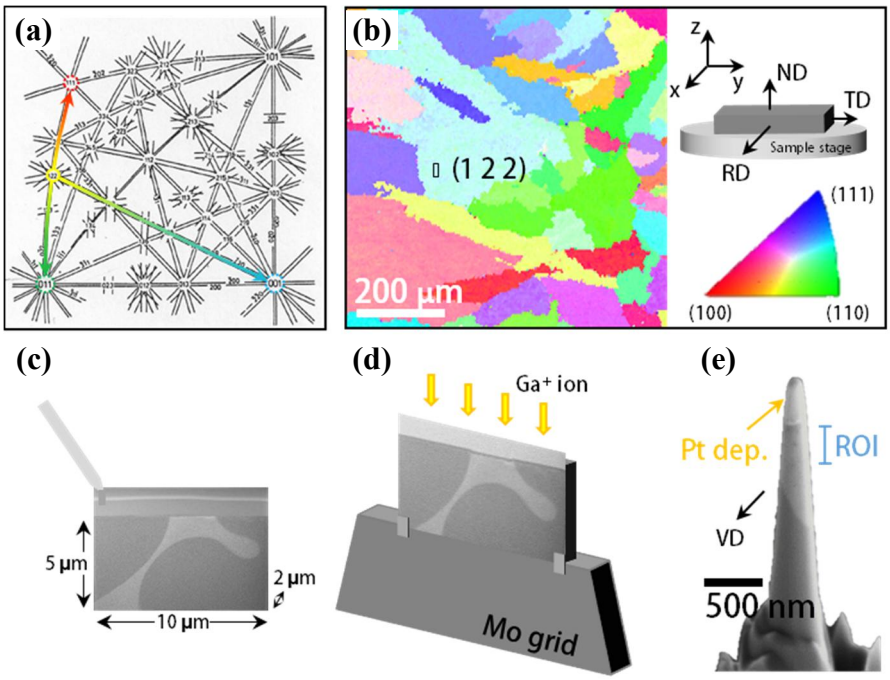

Figure 2.4 Sample preparation procedure for STEM-EDS tomography. (a) Selection of $(122)_{RD}$ plane to obtain images at (100), (110) and (111) plane by tilting. (b) Picking a lamellar with $(122)_{RD}$ plane. (c) Moving to a Mo grid. (d) Conical tip fabrication by coarse and fine milling. (e) Final tip image. x, y and z represent the coordination of sample stage and RD, TD and ND indicate the sample coordination.

2.2 Microstructural Characterization

2.2.1 X-ray Diffraction

The structure of the as-cast and homogenized samples in Section 3.2.1 and 3.4.1 were first examined by X-ray diffraction (XRD) (Bruker; D8 Advance Sol-X) using monochromatic Cu Kα radiation (2θ = 10 - 80°) at 40 kV and 40 mA. Due to shallow irradiated region, the structure of the irradiated samples were determined using grazing incidence X-ray diffraction (GIXRD) (Rigaku; D-MAX 2500) using monochromatic Cu K_α radiation (2θ = 30 - 100°) with continuous θ/2θ scan at 40 kV and 150 mA at glancing angle is 2°.

2.2.2 EPMA & SEM

A JEOL JXA-8500F electron probe microanalyzer (EPMA) was used to observe back scattered electron (BSE) image and determine the composition in the investigated the alloy. The acceleration voltage and the probe current were set to 15 kV and 10 nA, respectively. The compositions of individual phase were acquired at 5 different region and were averaged. For BSE image observation, the dual-beam focused ion beam (FIB) (Thermo-Fisher Scientific; Helios Nanolab 600) was also utilized.

2.2.3 (S)TEM & TEM holder

Microstructure was characterized by transmission electron microscope (TEM) (Thermo-Fisher Scientific; Tecnai F20 at 200 kV) linked with an energy dispersive spectrometer (EDS). Qualitative EDS mapping was carried out using a Talos TEM (Thermo-Fisher Scientific; Talos F200X 80-200 at 200 kV) equipped with X-FEG and super-X EDS system with four silicon drift detectors (SDDs) (Bruker). Bruker Esprit™ software is utilized to acquire STEM-EDS mapping images. An Electron energy-loss spectroscopy (EELS) for the sample thickness using a log-ratio (absolute) technique and high resolution (HR) TEM were acquired using a Titan TEM (Thermo-Fisher Scientific; Titan S 80-300 at 300 kV). ASTAR™ and precession electron diffraction (PED) technique for hardware and data acquisition software package were performed using double tilt rotation holder (Gatan; 925 Double Tilt Rotation Holder). Additionally, tomography holder (Fischione; Model 2020 Advanced Tomography Holder) was utilized for STEM-EDS tomography. For in-situ heating experiment in high voltage electron microscope (HVEM), a heating holder (Gatan; Double tilt heating holder, model 652) was used.

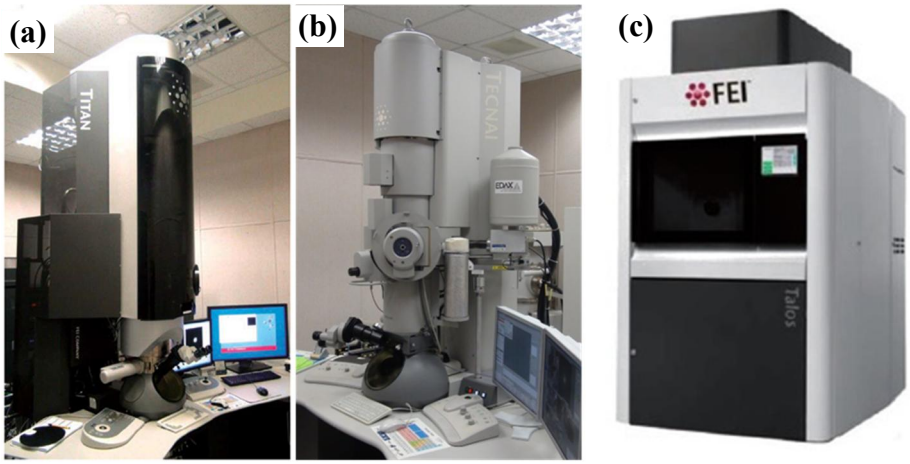

Figure 2.4 TEM instruments of (a) Titan S 80-300 for HR images, (b) Tecnai F20 for ASTAR-PED and TOPSPIN measurement, and (c) Talos F200X equipped with super-X EDS system for STEM-EDS mapping in KIST [1].

2.2.4 Orientation Mapping using PED

The orientation mapping was performed on FEI Tecnai F20 TEM using the ASTAR™ and PED (NanoMEGAS) for the hardware and data acquisition software packages.[43] The precession of the electron beam was performed with the angle of 1° from the optic axis and the scanning was conducted with 2.5 nm of step size. The diffraction pattern at each step was recorded by an external high speed camera and it was indexed automatically with the calculated diffraction patterns for Ni (a=3.524Å, Fm3m, (225)).

2.2.5 STEM-EDS tomography

Using a Fischione single tilt tomography holder, the HAADF and EDS-STEM tomography tilt series were acquired at the tilt range from -75° to 78°. TEM tomography software (ver. 4.1.2.4690, Thermo-Fisher Scientific) in Talos TEM (Thermo-Fisher Scientific) is utilized to acquire an EDS mapping image and each images is acquired upto ±50° with 3° interval and from ±50° with 1° interval. Data acquisition was acquired for 2 min using Bruker Esprit™ software. Inspect 3D software (ver. 4.1, Bruker) is used to construct acquired data in 3D by reconstructing a series of 2D projected images acquired at various tilt angles followed by 3D data processing. Amira™ software (ver.5.4.5) was utilized to visualize and calculate the volume fraction of the precipitates.

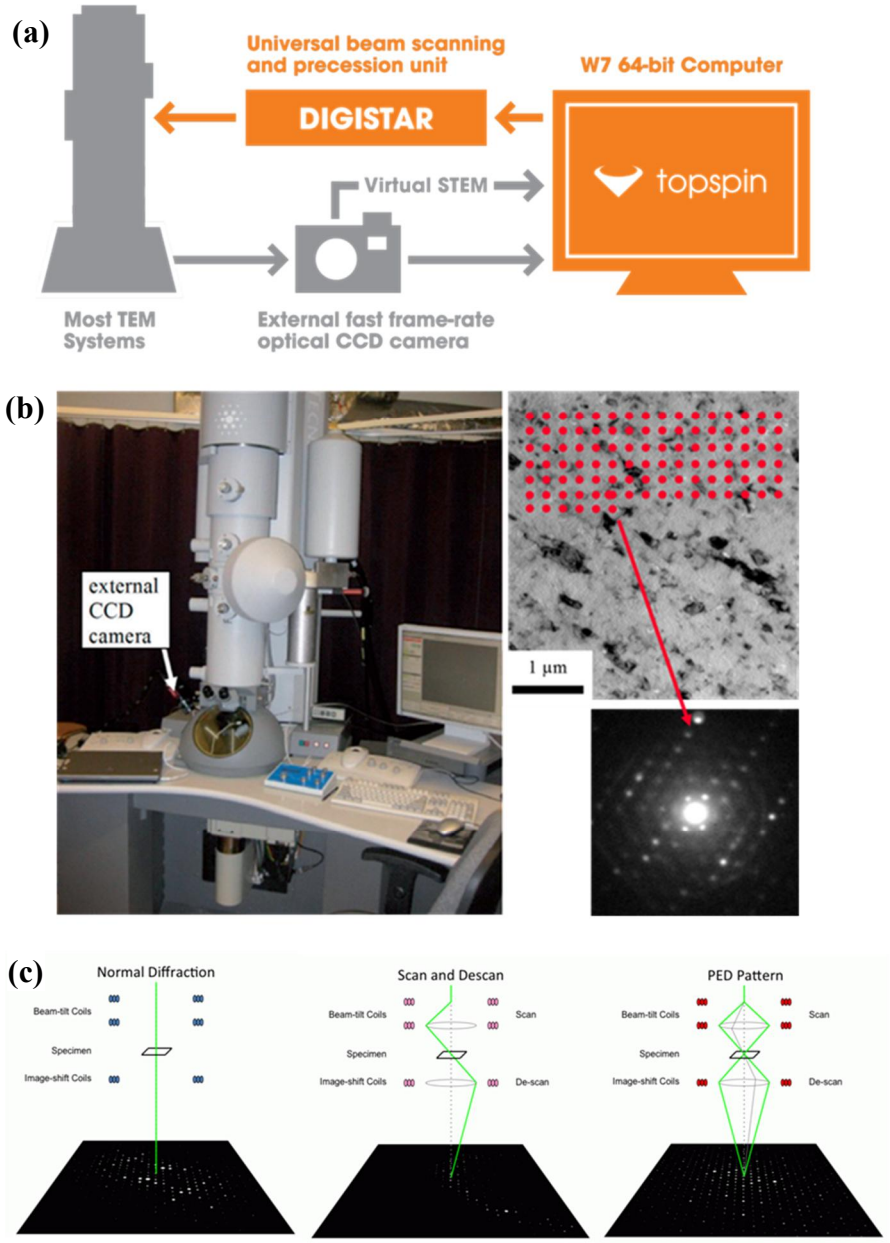

Figure 2.5 (a) Procedures for ASTAR™. (b) Automated crystal orientation mapping. (c) Geometry of electron beam in normal diffraction, scan and descan state, and precession electron diffraction [6]. Recomposed from ref. [6] with permission through "CC BY-SA 4.0".

2.2.6 Atom Probe Tomography

The elemental distribution was determined in detail with 3D atom probe tomography (3D-APT) technique. APT samples were prepared using a dual-beam focused ion beam (FIB) (Thermo-Fisher Scientific; Helios Nanolab 600). APT experiments were performed with two types of local electrode atom probe (CAMECA Instruments; LEAP 4000X HR in KIST & LEAP 4000X Si in Northwestern University). For as-cast and homogenized alloy, LEAP 4000X HR in KIST (Figure 2.7(a)) was utilized, applying laser energy of 50 – 70 pJ with 0.3% of detection rate at a pulse repetition rate of 160 - 200 kHz and at 33 K. LEAP 4000X Si in Northwestern University (Figure 2.7(b)) was used to investigate 3D structure and chemical information of irradiated alloy. In addition, the experiments were performed at 30 pJ of the laser energy, 1% of detection rate, 500 kHz of pulse rate, and 43 K of setting temperature. The LEAP data was evaluated using the software IVAS 3.6.14 provided by CAMECA Instruments.

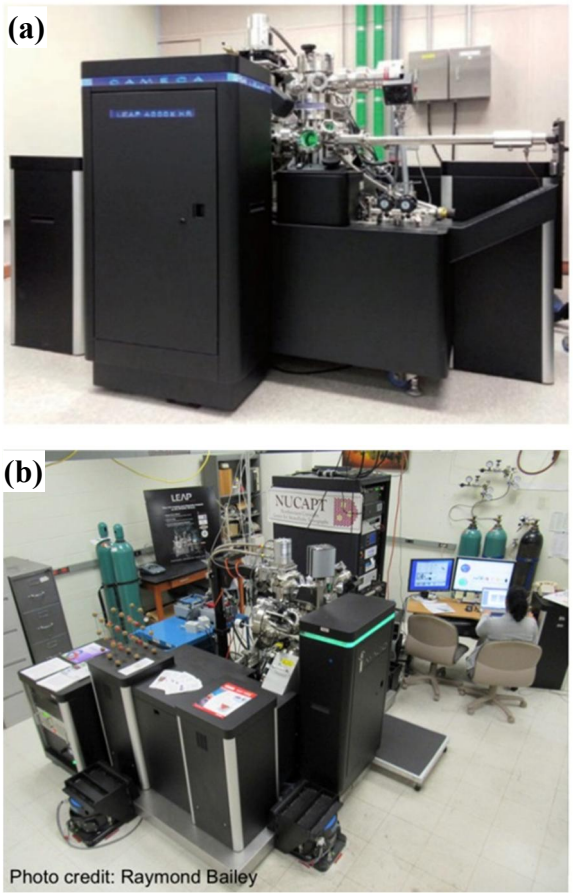

Figure 2.6 APT instruments of (a) LEAP 4000X HR in KIST and (b) LEAP 4000X Si in Northwestern University.

2.3 Thermal Analysis

2.3.1 Laser Flash Method

The laser flash method (LFA 457, NETZSCH) shown in Figure 2.8 was used to measure thermal conductivity from 298 K to 573 K under Ar atmosphere. The principle of the laser flash method was referred as below. At first, the front side of a plane-parallel sample is heated by a short laser pulse. And then, the absorbed heat induced propagates through the sample and causes a temperature increase on the rear surface. This temperature rise is measured versus time using an infrared detector. The thermal conductivity (κ) and in most cases the specific heat (C_p) can be ascertained using the measured signal.

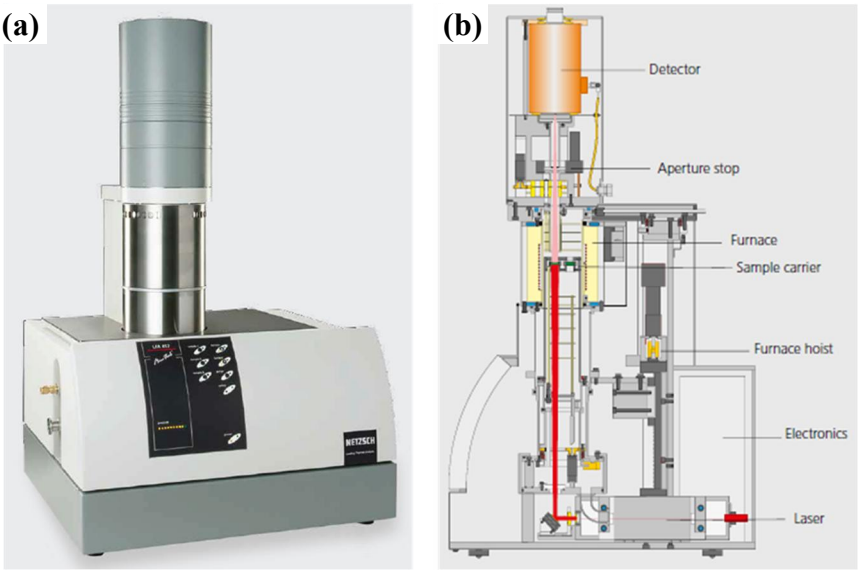

Figure 2.7 (a) Instrument for laser flash method to measure thermal conductivity κ of the materials (b) schematic diagram of the components in laser flash method [4].

2.4 Mechanical Analysis

2.4.1 Indentation Test

Nanoindentation tests were performed using a nanomechanical tester (Hysitron; TI 750 TriboIndenter). Indenting force was loaded up to a maximum load of 5 mN using a Berkovich type diamond tip in load control mode at a constant loading rate of 1 mN/s. The values of reduced elastic modulus and nano-hardness were obtained by averaging the results of 100 repeated tests. The hardness of un-irradiated and irradiated alloy were measured using micro-indentation (Emco-test; Dura Scan 70) with Vickers indenter. A series of ten measurements in 50 μm was carried out on individual sample with load 0.01 N.

2.4.2 Nano-pillar Compression Test

The compression tests were performed using Hysitron PI-85 picoindenter in a SEM (Thermo-Fisher Scientific; Quanta 250 FEG) (Figure 2.9). A flat diamond punch with 1 μm of diameter circular end was utilized. The compression tests were carried out by strain rate control mode.

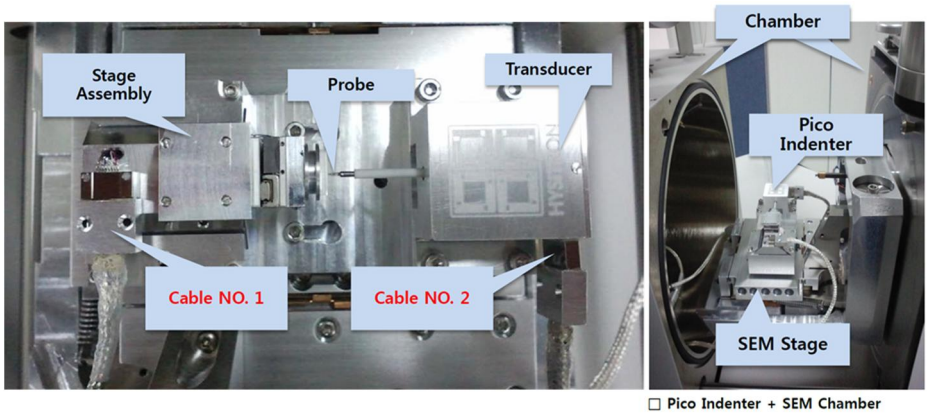

Figure 2.8 Overview of an in-situ indentation instrument (Hysitron; PI-85 Picoindenter) inside SEM [16]. Reprinted from ref. [16] with permission through "CC BY".

2.5 Irradiation Experiment

2.5.1 HVEM

The electron irradiation was performed using HVEM (ARM 1300S at 1.3 MeV) in Korea Basic Science Institute (KBSI) (Figure 2.10). Since the accelerating voltage is higher in HVEM than that of conventional TEM, it is well utilized for electron irradiation. As investigated in Section 4.3, individual HR images were obtained with 1.5 frames/sec and after acquisition the images were converted to movie file. Using TEM heating holder (Gatan; Double tilt heating holder, model 652), HR images were acquired at 150℃ and 400℃ during electron irradiation in real time. In order to calculate the defect density, the thickness of TEM samples was obtained via EELS measurement. All the defect clusters was observed at edge on state. Furthermore, the detailed experimental condition for electron irradiation was referred later in Section 4.2.

Figure 2.9 TEM instrument of ARM 1300S in KBSI for electron irradiation [29].

2.5.2 2 MV Tandem Accelerator

The alloy was irradiated using 13 MeV Cu^{6+} ions at room temperature in KIST, utilizing 2MV tandem accelerator (Figure 2.11). A water-cooled stage is utilized to reduce thermal annealing effect during irradiation. A raster beam is used to provide uniform irradiation at the 12 x 12 mm^2 of irradiation area. The frequency of the raster beam was 64 Hz for x direction and 513 Hz for y direction. The dose rate is 8.68×10^{14} ions/m^2·sec and the fluence is 1.19×10^{19} ions/m^2. Irradiation damage obtained from SRIM calculation [44] is converted into dpa under the Kinchin-Pease mode with 40 eV displacement energy [45]. The maximum irradiation dose was 2.4 dpa at 2.4 μm.

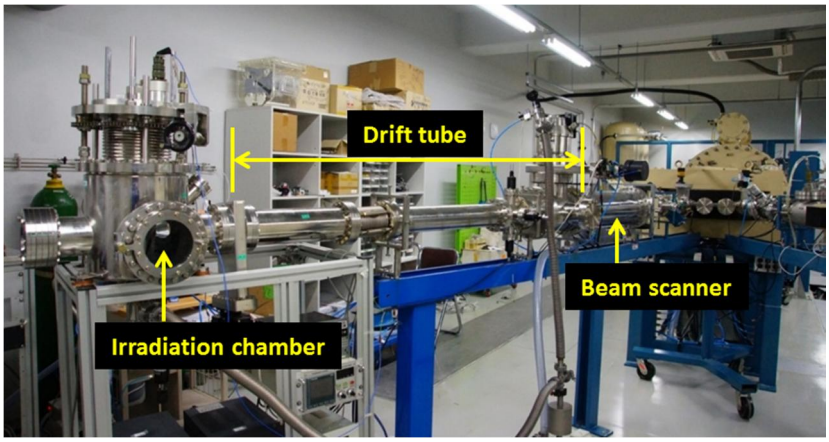

Figure 2.10 Instrument of 2 MV Tandem accelerator for ion irradiation [1].

Chapter 3. Precipitation during Solidification and Annealing and Its Effect on the Mechanical Responses

3.1 Introduction

The HEAs that are solid solution phase due to multiple alloy with similar atomic fraction provides not only solid solution strengthening but also increase in athermal stress resulting from the lattice distortion as referred in Section 1.4. Besides, due to high concentration of solute atoms in the HEAs, the barrier to dislocation movement cannot be easily overcome by thermal activation and, as a result, higher friction stress occurs during deformation [46]. Moreover, the single phase HEAs like CrMnFeCoNi show enhanced mechanical property resulting from nano-twinning [47, 48]. Furthermore, since the HEAs show superior mechanical properties [48-50] even at elevated temperature [51-58], they are attractive for structural applications. As the alloy design of HEAs leads the conventional alloy systems in the edge in the phase diagram to move toward center, lots of fascinating new materials could be developed. The HEAs have been studied to search the composition range with the single phase solid solution, maximizing solid solution strengthening by high concentration of solute atoms [32, 59, 60].

But, most HEAs shows multi-phase like segregation, ordering, chemical inhomogeneity and so on (Figure 1.18), which makes difficult to apply in practical use. Using phase diagram, many researchers have tried to develop a

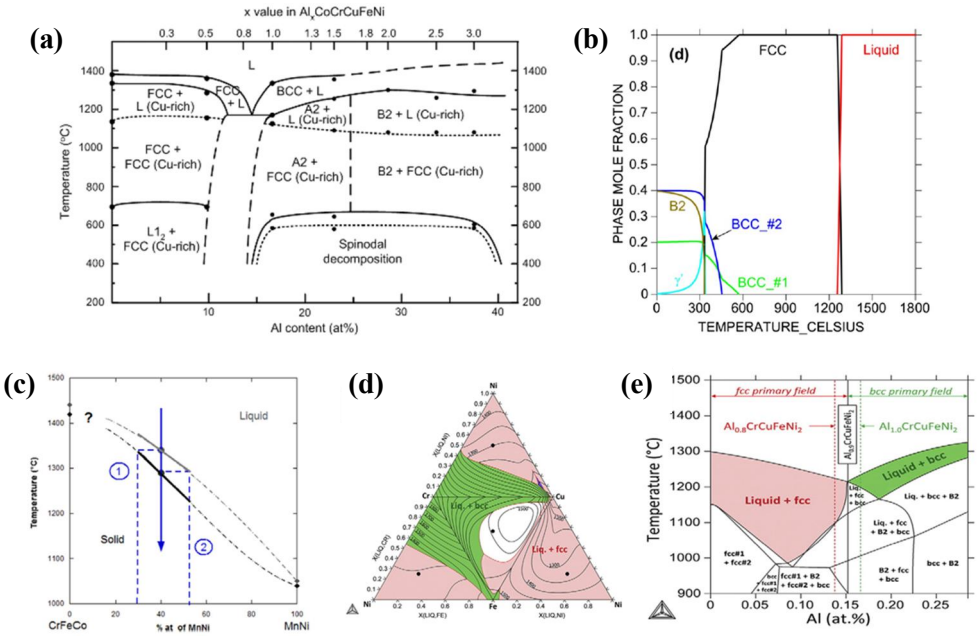

Figure 3.1 Various kinds of the phase diagram of multi-component systems. (a) Predicted phase diagram of $Al_xCrFeCoNiCu$ HEA with Al content ($0 \le x < 3$) [19]. (b) Calculated phase mole fraction as a function of temperature for CrMnFeCoNi HEA [32]. (c) Schematic phase diagram between CrFeCo and MnNi based on experimental results [36]. (d) Calculated tetrahedron of quaternary Cr-Fe-Cu-Ni system [38]. (e) Calculated isopleth for $Al_xCrFeNi_2Cu$ HEA ($0 \le x \le 2$) [38]. Reprinted from ref. [19], [36] and [38] with permission through "Copyright Clearance Center". Reprinted from ref. [32] with permission through "CC BY 3.0".

desired alloy by controlling the alloy composition and the processing condition; however, the thermodynamic database covers the composition range at near-edge region in the phase diagram. In spite of this difficulty, there has been an attempt to draw phase diagrams of HEAs [19, 32, 36, 38, 60-63]. Especially, the phase diagrams were constructed in order to search the composition with single phase solid solution [32, 60, 62] and mainly investigate the phase stability and phase evolution of HEAs [19, 36, 38, 61]. At first, the phase diagram was experimentally predicted in $Al_xCrFeCoNiCu$ HEA($0 \leq x \leq 3$) with Al content utilizing the microstructure and the phase transformation temperature. Unfortunately, it can't provide the composition of individual phase directly and only gives the information about the phase region. Based on this phase diagram, the phase formation sequence during solidification was determined [19]. Using the database for Ni based alloy, the phase diagram between temperature and mass fraction of the phases was also reported in $Al_{0.5}CrFeCoNiCu$ alloy. Unfortunately, since quantitative information is inaccurate on the relative fraction of disordered or ordered phase in HEAs, it is observed that there is discrepancy on the FCC ordering between the prediction and experimental observations [61]. Moreover, the vertical-sectioned phase diagrams were calculated in AlCrFeCoNi(Cu) system showing the phase stability by individual element and phase evolution sequence during solidification [38, 62]. Up to now, there have been limited to draw phase diagram using only experimental results or calculation and a few attempt to correspond experiment with thermodynamic information.

Strengthening mechanisms are categorized independently by solid solution hardening, grain boundary hardening, dislocation hardening, and precipitation hardening and so on. Since total strengthening is presented by the sum of individual contributions on the hardening, the mechanical property can be optimized via composite structure like precipitation [21, 64] and eutectic lamellar structure [65-67], apart from the solid solution strengthening. Despite the necessity considering each contribution on the hardening, a few works are reported in the HEAs with complicated microstructure. For example, the precipitation-hardened HEAs show improved mechanical property by $L1_2$ coherent nano-sized precipitate in the FCC matrix and this hardening attributes dominantly to the precipitation hardening [21]. Furthermore, the hardness increased, reached a peak point and then, decreased with aging, resulting from the same trend of the precipitate size [33]. Likewise various mechanical characterizations are proposed to investigate the contribution on the mechanical response like an indentation technique.

A $Cr_{20}Fe_{20}Co_{20}Ni_{20}Cu_{20}$ alloy is the simplest system among the early transition metal based HEAs and then, it was selected as a case alloy in this study. Furthermore, the microstructures like the composition, size and volume fraction of the precipitates and the coherency were investigated via multi-scale characterization like SEM, (S)TEM and APT. Moreover, the simplified vertical sectioned pseudo-binary phase diagram was presented to show the phase evolution sequences and the processing condition like annealing temperature was determined via the diagram. Furthermore, the contributions

o n t h e

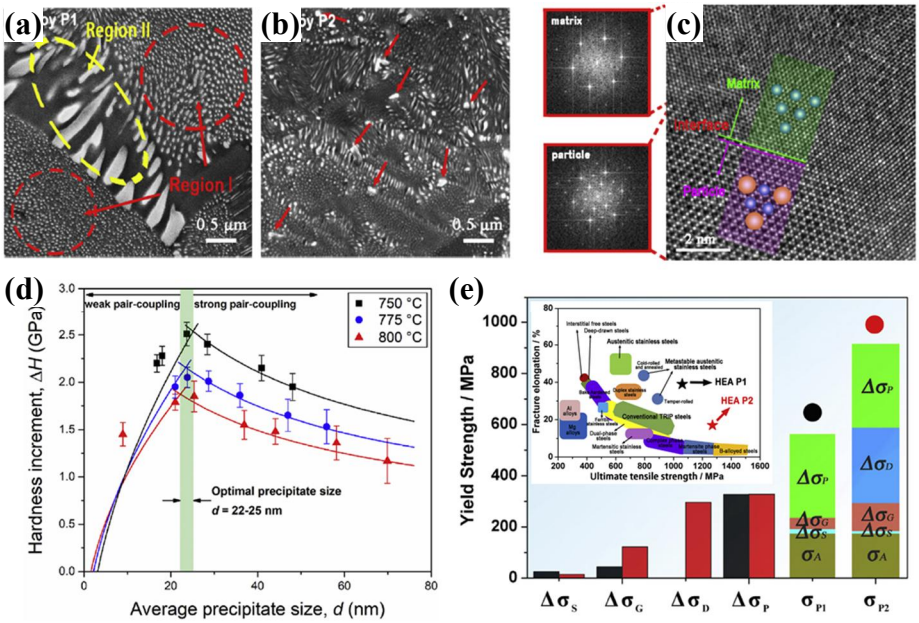

Figure 3.2 SEM images of $(CrFeCoNi)_{94}Ti_2Al_4$ alloy; (a) P1 alloy and (b) P2 alloy fabricated with different aging condition. (c) HR TEM image showing the interface between the nano-particle and FCC matrix and the corresponding Fast Fourier transformations (FFT)s of the P1 alloy [21]. (d) Hardness increment (ΔH) with the average precipitate size (*d*) for $(CrFeCoNi)_{94}Ti_2Al_4$ alloy aged at temperature between 750 and 800℃ [33]. (e) The contribution of the different hardening mechanism on the strength in $(CrFeCoNi)_{94}Ti_2Al_4$ alloy and the ultimate tensile strength-ductility map of various advanced steels including P1 and P2 HEAs (inset) [21]. Reprinted from ref. [21] and [33] with permission through "Copyright Clearance Center".

mechanical property were systematically investigated via nanoindentation before and after homogenization. Finally, the optimum procession condition was proposed to show excellent mechanical property. Consequently, an insightful guideline to design HEA as a structural application can be provided.

3.2 Solidified Microstructure

3.2.1 Hierarchical Microstructure Analysis

Microstructure of the as-cast CrFeCoNiCu HEA was primarily evaluated with XRD. It exhibited diffraction peaks corresponding to a FCC crystal with additional small peaks just next left to the main peaks, indicating that two FCC phases coexist in the as-cast alloy (Figure 3.3(a)). A back-scattered electron (BSE) image of the as-cast CrFeCoNiCu HEA showed a typical dendrite structure (Figure 3.3(b)).

Chemical composition of each phase was measured quantitatively by EPMA in Table 4. The dendrite phase with dark contrast consists of four main elements of Cr, Fe, Co and Ni (22. 8 at.% Cr-22.9 at.% Fe-23.2 at.% Co-20.7 at.% Ni-10.4 at.% Cu), while the interdendrite phase with bright contrast is Cu-rich phase (3.0 at.% Cr-3.4 at.% Fe-3.3 at.% Co-8.2 at.% Ni-82.1 at.% Cu). In brief, the CrFeCoNiCu alloy was composed of the dendrite with nearly even ratio of Cr, Fe, Co and Ni and one conventional Cu-rich solid solution phase, and both had FCC crystal structure as speculated in XRD data. Using XRD, the lattice parameters were measured to be 3.60 Å for interdendrite (FCC2) and 3.57 Å for dendrite (FCC1), respectively. Misfit ratio between dendrite and interdendrite was calculated as 0.85%, suggesting semi-coherent interface.

Further nanostructure was examined using TEM. A bright field TEM (BF-TEM) image (Figure 3.4) shows interphase region between the dendrite

and the Cu-rich interdendrite. The corresponding selected area diffraction pattern

`

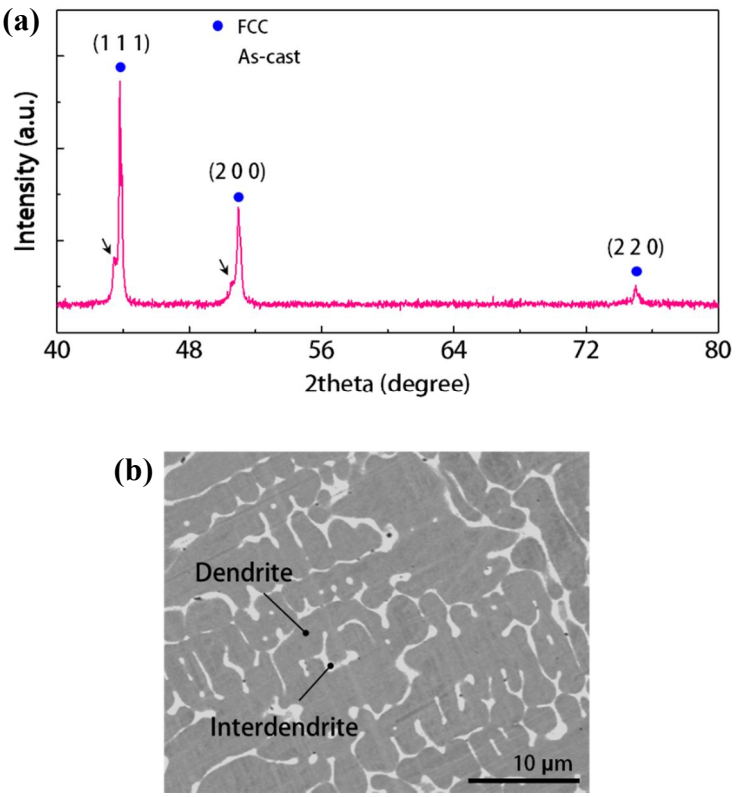

Figure 3.3 (a) XRD pattern and (b) BSE image of as-cast CrFeCoNiCu HEA.

	Dendrite	Interdendrite
Cr	22.8±0.2	3.0±0.5
Fe	22.9±0.2	3.4±0.5
Co	23.2±0.7	3.3±0.4
Ni	20.7±0.6	8.2±1.0
Cu	10.4±0.4	82.1±2.4

Table 2 Microscale chemical composition measured by EPMA of the as-cast and the homogenized CrFeCoNiCu HEAs.

(SADP) (inset) showed an [110] zone orientation of the FCC phase. It was noted that even though both phases are selected for the diffraction pattern, the elongated diffraction spots that the two diffraction spots of the dendrite and the interdendrite are overlapped were appeared due to same crystal structure with small misfit between two phases.

The microstructure of as-cast CrFeCoNiCu HEA was investigated and two FCC structures of CrFeCoNi rich dendrite and Cu-rich interdendrite with semi-coherent interface were observed. For here, the morphology and chemical information of the precipitates in the as-cast CrFeCoNiCu HEA, in detail. Besides, in the BF-TEM image shown in Figure 3.4, a coffee bean contrast with tens of nanometer size was observed in the Cu-rich interdendritic region and nano-scale dark grey contrast appeared in the dendritic region but complex morphology and contrast hampered to understand the general structure. Thus EDS elemental maps were obtained at the interface and showed that dendrite and interdendrite both contain nano-sized secondary phases indicating the partition of the CrFeCoNi and Cu (Figure 3.6). The 2^{nd} phases both had FCC structure and coherent orientation relationship with the corresponding matrix, thus induces no extra diffraction spot in the SADP (Figure 3.4).

Since precipitate is heterogeneously nucleated on vacancy and precipitates are difficult to nucleate adjacent to boundary and, as a result, precipitate free zone (PFZ) is formed near the boundary. The PFZ formed with a width of approximately 75 nm in the Cu-rich interdendrite side and nearly

16 nm in the dendrite side. Because the phase boundary is semi-coherent with 0.85% of

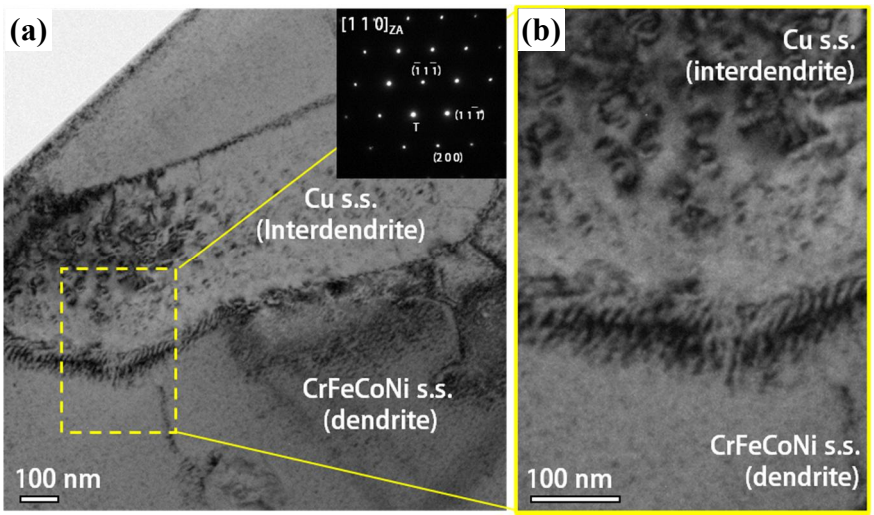

Figure 3.4 (a) TEM BF image and corresponding SADP along <100> FCC zone direction (inset) and (b) the magnified image from the yellow dashed area of as-cast CrFeCoNiCu HEA.

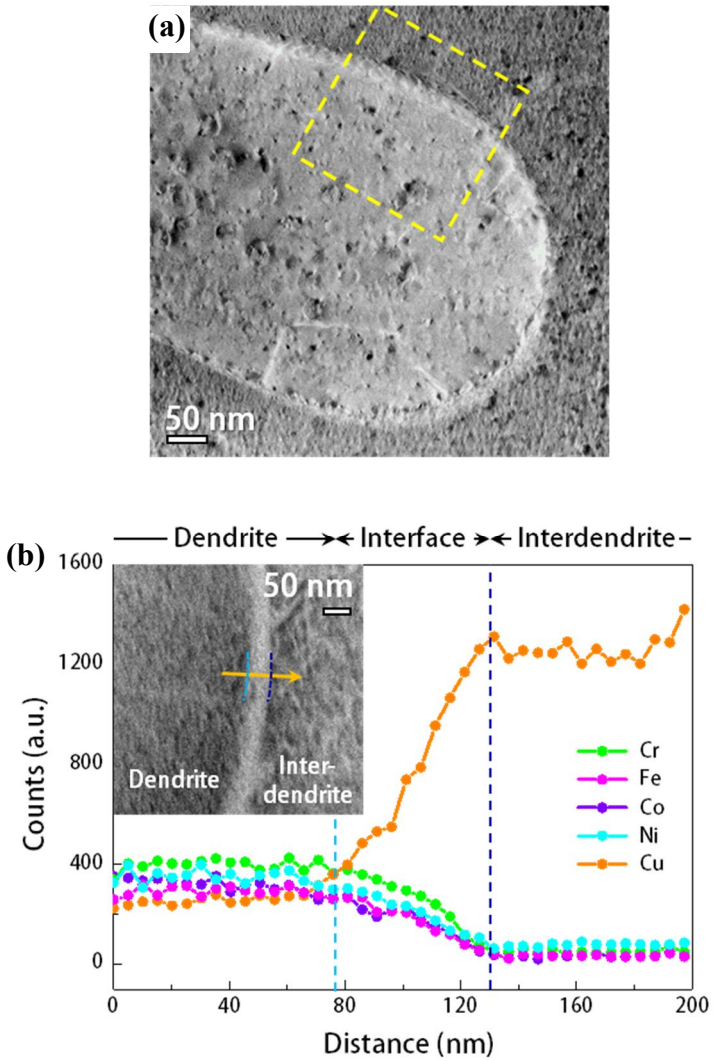

Figure 3.5 (a) STEM-annular dark field (ADF) image and (b) STEM-EDS line profile from dendrite to interdendrite and corresponding STEM-ADF image with the line profile.

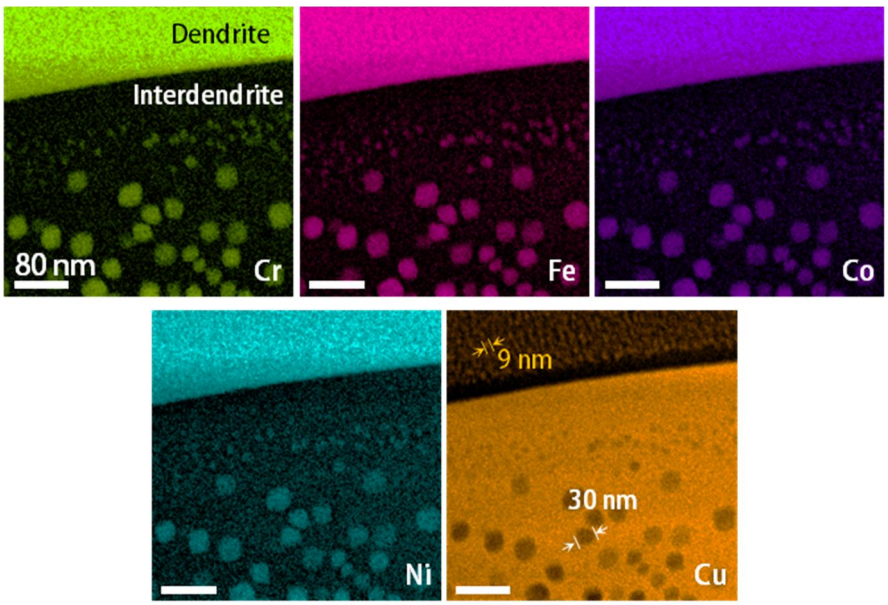

Figure 3.6 Elemental STEM-EDS mapping images for Cr, Fe, Co, Ni and Cu of the as-cast CrFeCoNiCu HEA.

misfit and both phases are FCC structure, especially stress and self-diffusion affected the width of PFZs. The boundary near interdendrite was applied by compressive stress and, as a result, the vacancies migrated dominantly toward the boundary near the interdendrite. Furthermore, the self-diffusion coefficient of the Cu-rich interdendrite was higher compared with that of the dendrite. From these two reasons, the width of PFZ was wider in the interdendrite rather than in the dendrite.

3.2.2 Three Dimensional Microstructural Characterization

The 2nd phase in the Cu-rich interdendrite region was CrFeCoNi-rich phase and also had the FCC structure having coherent crystallographic relation with the Cu-rich matrix; however, the shape of the 2nd phase in the interdendrite was not clear so, STEM-EDS tomography was utilized to determine the shape (Figure 3.7). Figure 3.8 shows Cu elemental map and overlapped Cr and Fe elemental map of the interdendrite at [001] zone axis during tilting for STEM-EDS tomography. The cuboid shaped 2nd phases were aligned along <100> direction and nearly 29 nm for length with approximately 6 vol%. In the CrFeCoNi dendrite region, more fine Cu-rich 2nd phases with a diameter of nearly 9 nm were uniformly distributed and the shape could not be determined due to the resolution limitation. As the 2nd phase were small enough to be embedded in the matrix even in thin foil TEM

sample, getting accurate limited. chemical composition of the 2nd phases without matrix effect by TEM-EDS was So 3D-APT analysis was performed to detect the local chemical composition of the 2nd phases in Figure 3.9. The insets in Figure 3.9(a-b) indicate Cu atom map of the dendrite delineated by 40 at.% Cu and Fe atom map of the interdendrite delineated by 14 at.% Fe, respectively. These isoconcentration surfaces allowed to generate averaged proximity histogram concentration profiles. Figure 3.9(a-b) display the proxigrams for the dendrite and interdendrite and the average compositions of the matrix and the 2nd phases in the dendrite and interdendrite were determined in Table 3. The composition of the dendritic matrix was 24.3 at.% Cr-24.7 at.% Fe-23.8 at.% Co-21.8 at.% Ni-5.4 at.% Cu and the 2nd phase in the interdendrite showed 24.0 at.% Cr-27.6 at.% Fe-23.2 at.% Co-21.0 at.% Ni-4.2 at.% Cu. Moreover, the volume fraction of the 2nd phase in the dendrite was directly calculated from the ratio of the total number of atoms contained within the 2nd phase to the total number of atoms collected and the average atomic density of the two phases [68]. As a result, the volume fraction of the 2nd phase was nearly 15%. It was noteworthy that Cu is completely partitioned from CrFeCoNi and the composition of the 2nd phase in the interdendrite is close to that of the dendritic matrix and vice versa. To summarize, as-cast CrFeCoNiCu HEA had a simple FCC crystal structure but had two chemically separated phases which contain the other phase as the 2nd phase resulting in an interesting composite structure.

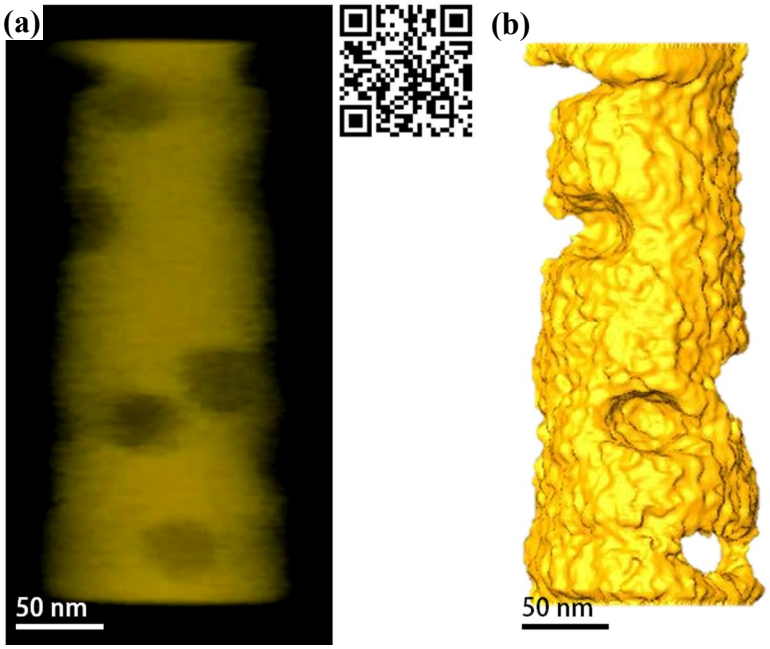

Figure 3.7 (a) STEM-EDS tomography reconstruction and (b) reconstructed volume using Amira™ software.

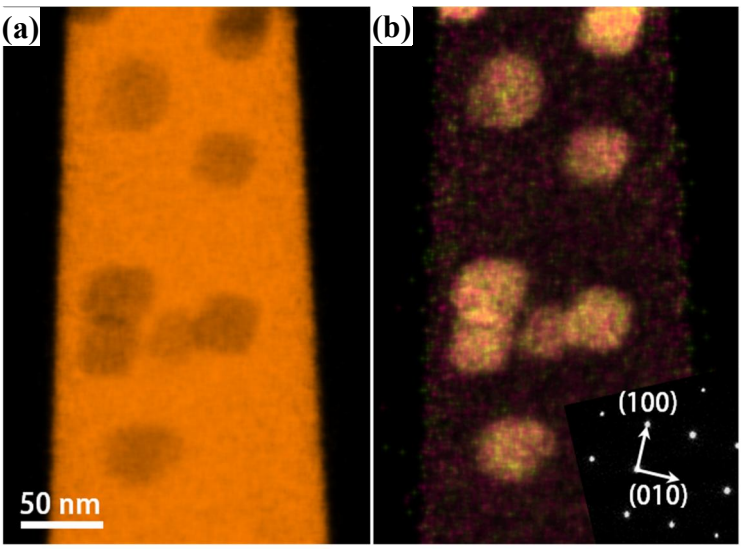

Figure 3.8 (a) Cu and (b) overlapped Cr and Fe elemental EDS mapping images and corresponding selected area diffraction pattern along <100> in the as-cast interdendrite of CrFeCoNiCu HEA.

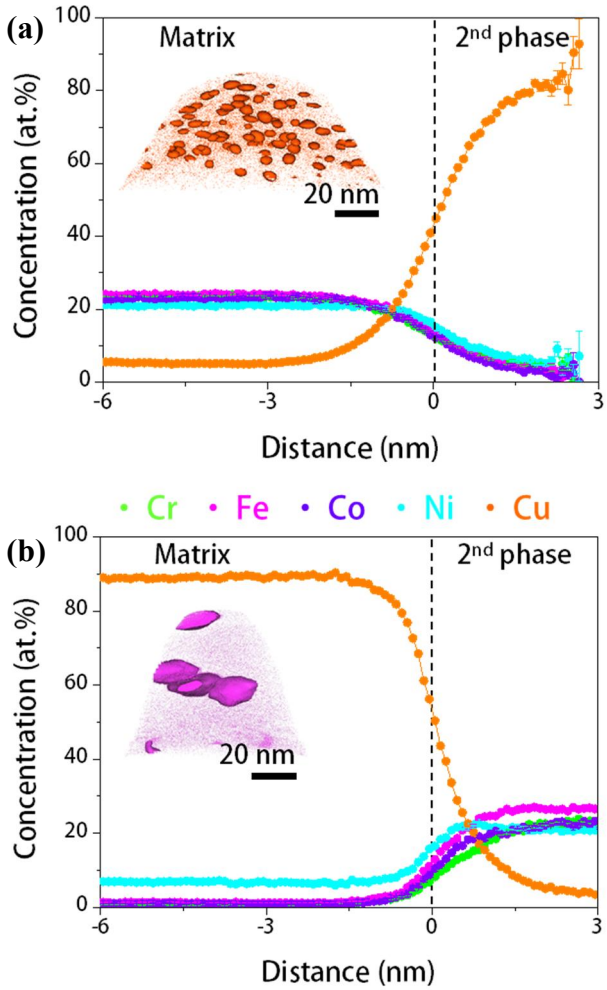

Figure 3.9 (a) APT reconstruction showing the 2nd phase of as-cast dendrite delineated by 40 at.% Cu and proxigram corresponding to 40 at.% Cu shows describes the chemically partitioning of alloy elements. (b) APT reconstruction illustrating the 2nd phase of as-cast interdendrite delineated by 14 at.% Fe and proxigram showing similar composition of 2nd phase in dendrite with interdendritic matrix and similar composition of dendritic matrix with the 2nd phase of interdendrite.

	Dendrite (at.%)		Interdendrite (at.%)	
	Matrix	2nd phases	Matrix	2nd phases
Cr	24.3±0.2	4.5±0.9	0.6 ± 0.1	24.0 ± 1.1
Fe	24.7±0.2	2.9±0.9	1.2 ± 0.1	27.6 ± 1.5
Co	23.8±0.2	2.1±0.7	0.9 ± 0.1	23.2 ± 1.4
Ni	21.8±0.2	6.2±1.8	6.9 ± 0.3	21.0 ± 1.2
Cu	5.4±0.2	84.3±1.6	90.4 ± 0.4	4.2 ± 0.6

Table 3 Chemical compositions of the as-cast alloy measured by 3D-APT (at.%). The compositions are determined by average value from proxigram and the errors represent the standard deviation.

3.3 Solidification Sequence

3.3.1 Calculation and Reliability of Pseudo-binary Phase Diagram

In the previous section, we experimentally verified that $Cr_{20}Fe_{20}Co_{20}Ni_{20}Cu_{20}$ HEA separates into Cu-rich and Cu-depleted phases during solidification, resulting from the positive mixing enthalpy of Cu with Cr, Fe, Co and Ni. Thus pseudo-binary phase diagram of Cu and CrFeNiCo was calculated by thermo-calc in order to intuitively understand the solidification path of the complex multicomponent system (Figure 3.10). The simplified pseudo-binary phase diagram would not be accurate enough to demonstrate the complex 5-element system, but it could provide a sketch on the solidification behavior roughly. In the pseudo-binary phase diagram, a miscibility gap exists upto 1487℃ even above liquidus line due to the large positive heat of mixing enthalpy between Cu and the others. The expected melting temperature of Cu and CrFeCoNi are 1085℃ and 1416℃, respectively. The solubility of Cu element in the CrFeCoNi solid solution is below 9 at.% and CrFeCoNi solid solution is soluble upto 3.8 at.% in Cu at 400℃.

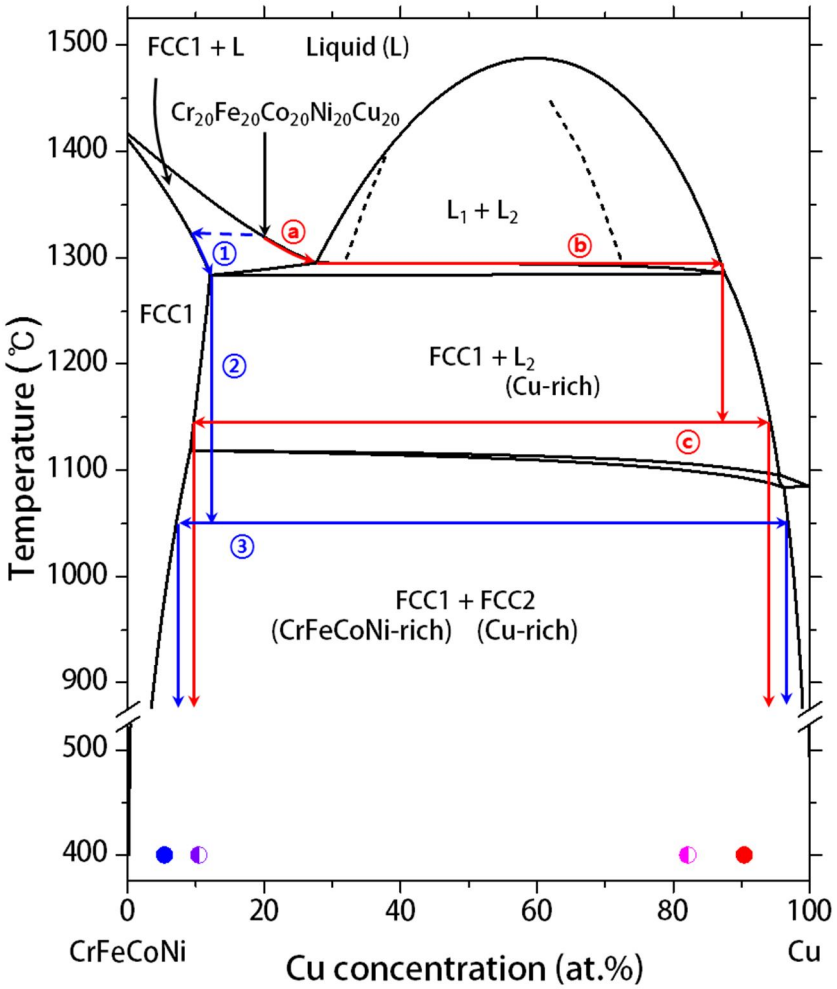

Figure 3.10 Calculated pseudo-binary phase diagram of CrFeCoNi/Cu high entropy alloy with spinodal decomposition presented by dot line (---). Solidification path is drawn with blue solid lines for the dendrite (—) and red solid lines for interdendrite (—). Composition of the dendrite (◐), interdendrite (◐) including precipitates which are confirmed with EPMA analysis are marked by half open circles. The composition of the dendritic matrix (●) and interdendritic matrix (●) excluding 2nd phase, measured by 3D-APT, are presented by closed circles.

3.3.2 Origin of the 2nd Phase Formation upon Solidification

The solidification path of CrFeCoNi-rich dendrite and Cu-rich interdendrite can be drawn in the pseudo binary phase diagram.(Figure 3.10) Since the casting method used in this study which has much lower cooling rate than rapid solidification, it would position between equlibrium and nonequilibrium state. Here, we assumed that 1) there is no back-diffusion from solid to liquid, 2) solidification occurs in the condition between equilibrium and Scheil equation, and 3) three phase regions, (FCC1 + L_1 + L_2) and (FCC1 + FCC2 + L_2), are too narrow to be ignored. The solidification process of each phase of $Cr_{20}Fe_{20}Co_{20}Ni_{20}Cu_{20}$ HEA was explained as below.

(1) Solidification sequence of the dendrite

① Nucleation of primary CrFeCoNi-rich dendrite: $Cr_{20}Fe_{20}Co_{20}Ni_{20}$-$Cu_{20}$ liquid solidified with a primary dendrite with hypo-monotectic reaction above ~1300℃. Then, coring occurred passing through (FCC1 + L) region and the composition of the dendrite followed the solidus line of (FCC1 + L) phase.

② Growth of CrFeCoNi dendrite: The dendrite growed passing through (FCC1 + L_2) region and Cu-rich phase was still in liquid state.

③ Precipitation of Cu-rich 2nd phase: The three phase region (FCC1 +

FCC2 + L_2) at around 1100℃ was too narrow to be ignored. Below ~1100℃, the solubility decreased and thus nano-scale Cu-rich 2nd phases were evolved by precipitation.

(2) Solidification sequence of the interdendrite

ⓐ Formation of Cu-rich interdendrite in liquid state : The composition of Cu-rich liquid followed the liquidus line of (FCC1 + L) region.

ⓑ At ~1300℃, the liquid changed into solute-rich L_2.

ⓔ Precipitation of CrFeCoNi: Upon cooling from (FCC1 + L_2) region to the (FCC1 + FCC2) region, CrFeCoNi phase precipitated from L_2.

As a result of hierarchical phase separation, CrFeCoNiCu HEA exhibited an interesting composite structure. In micro-scale, it had dendritic composite structure with FCC1 (CrFeCoNi-rich) and FCC2 (Cu-rich) phases. Down to nano-scale, FCC1 dendrite contained the 2nd phase with FCC2 and FCC2 interdendirte included FCC1 precipitate.

3.4 Microstructural Evolution upon Annealing

3.4.1 Multi-scale Microstructure Characterization

The calculated phase diagram was utilized to select annealing condition that allows the composition of the matrix unchanged within 5 at.% Cu and the

size and composition of the precipitates to diversify. Thus homogenization treatment was performed in CrFeCoNiCu alloy at 1100℃ for 24 hours under Ar atmosphere followed by subsequent furnace cooling. After annealing, the dendritic CrFeNiCo-rich phase coarsened and spheroidized in order to minimize solid/liquid surface energy. (Figure 3.11 (a)) The dominant mechanism of the spheroidization is known to be recrystallization and coarsening of the dendrite arms.[69] Figure 3.11 (b-c) show the XRD results of as-cast and homogenized CrFeCoNiCu alloy with better peak resolution compared with Fig. 1(a). In spite of the structural evolution, no additional phase formation was detected in XRD analysis. Furthermore, the two FCC structure was still sustained, but the overlapped peaks separated to be distinguished clearly, indicating atomic redistribution occurred during homogenization. In fact, macroscopic chemical composition analysis by EPMA showed that Cu in the CrFeCoNi-rich dendrite depleted down to 8 at.%, whereas Cu concentration in the interdendrite and the spherical Cu-rich phase in the dendrite increases upto 89.2 at.% upon homogenization (Table 4).

To clarify the nanostructure, the EDS elemental maps and BF-TEM image are obtained from the dendrite and the interdendrite after homogenization in Figure 3.12. They revealed that there are two types of Cu-rich precipitates in the dendrite and CrFeCoNi-rich precipitates in the interdendrite, respectively. For the dendritic region, the larger one was disk-type with a dimeter of 128±48 nm and a height of 47±12 nm and it was aligned along <100> direction of the FCC dendritic matrix (Figure 3.12(a-b)).

The other one was finely dispersed spherical-type with the diameter of 28±24 nm (Figure 3.12(b)). On the contrary,

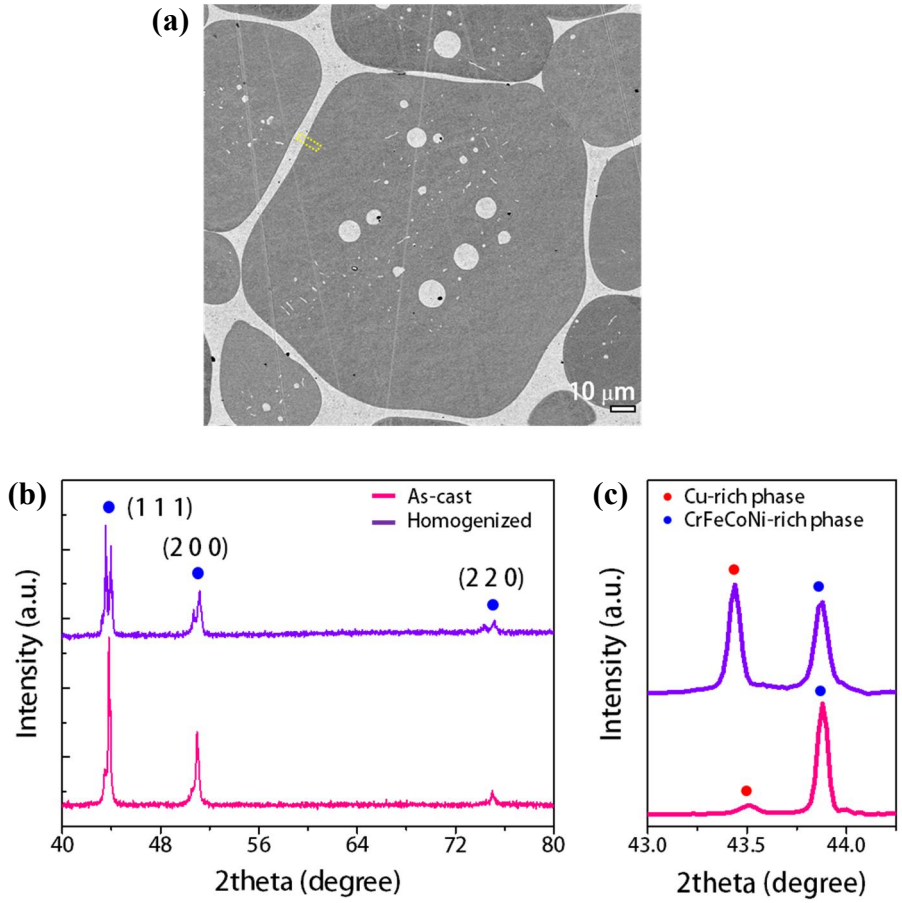

Figure 3.11 BSE image of CrFeCoNiCu HEA upon homogenization at 1100 ℃ for 24 hours with furnace cooling. The XRD pattern of as-cast and homogenized CrFeCoNiCu HEA (b) for whole scan from 40° to 80° and (c) at (111) plane from 43° to 44.5°.

	Dendrite	Interdendrite
Cr	23.4±0.3	1.0±0.2
Fe	23.4±0.3	1.7±0.3
Co	23.2±0.2	2.0±0.4
Ni	22.0±0.2	6.1±0.4
Cu	8.0±0.7	89.2±0.8

Table 4 Microscale chemical composition measured by EPMA of the homogenized CrFeCoNiCu HEAs.

one of the precipitates in the interdendrite was identified as cuboidal-shaped CrFeCoNi-rich phase with a side length of 49±16 nm in Figure 3.12(c) and the other was expected to be the thin disk shaped precipitates, which are GP zones, in Figure 3.12(d). In order to calculate the volume fraction of each precipitates, the thickness of the TEM samples was calculated as 124.4±29.3 nm using EELS measurement. Then, the volume fractions of the disk type and spherical shaped Cu-rich precipitates were 9.3% and 7.9%, respectively. Additionally, total volume fraction of the Cu-rich precipitates in the dendrite after homogenization was 17.2%, which is quite similar value with 15.5% of the precipitate fraction in the as-cast dendrite. Furthermore, for the interdendrite, the cuboidal shaped CrFeCoNi-rich precipitates were 1.5 vol% and thin disk shaped precipitates was too small to calculate the volume fraction, suggesting the decreased fraction of the precipitates in the interdendrite upon homogenization.

To determine the composition of the precipitates and the matrix quantitatively, 3D APT analysis was performed. The inset in Figure 3.13(a) shows three-dimensional reconstruction of Cu atom map from the dendrite region after homogenization. The iso-concentration surface was set as 8 at.% Cu. The iso-surface marked by 'A' in the inset represented disk shape Cu-rich precipitate. Figure 3.13(a-b) show proximity histogram from the disk-shaped Cu-rich precipitate, nano-scale spherical shaped Cu-rich precipitate, and the dendritic matrix, respectively. Moreover, the inset in the Figure 3.13(c) displays the Fe atom map from the interdendrite after homogenization

delineated by 14 at.% Fe. In the BF-TEM image in Figure 3.12(d), the morphology of the

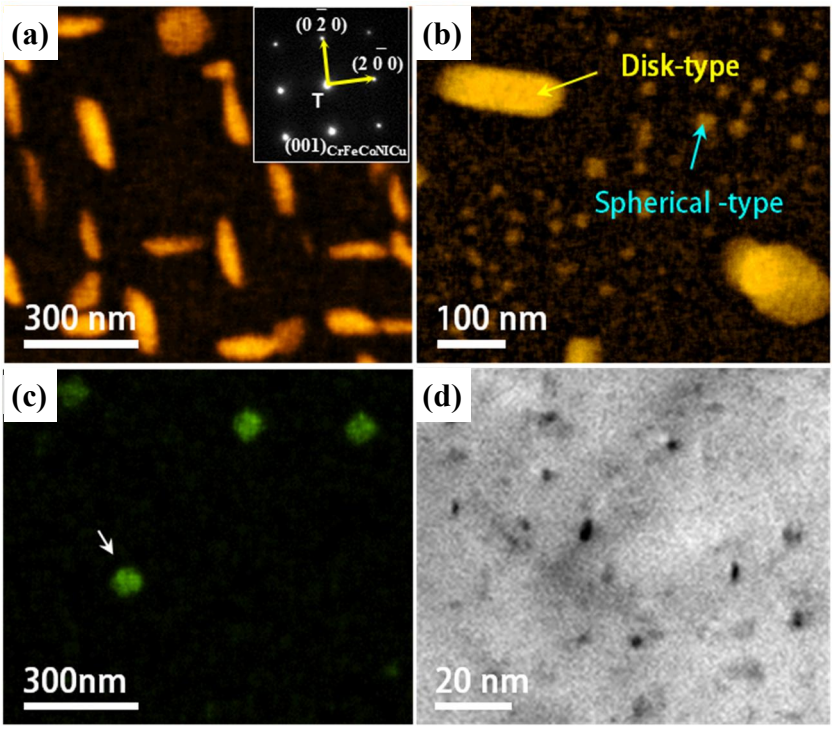

Figure 3.12 Cu elemental STEM-EDS mapping images of the dendrite in the homogenized CrFeCoNiCu HEA (a) observed at <100> FCC zone direction and (b) obtained at deviated zone direction. (c) Cr elemental STEM-EDS mapping image and (d) BF image of the interdendrite in the homogenized CrFeCoNiCu HEA.

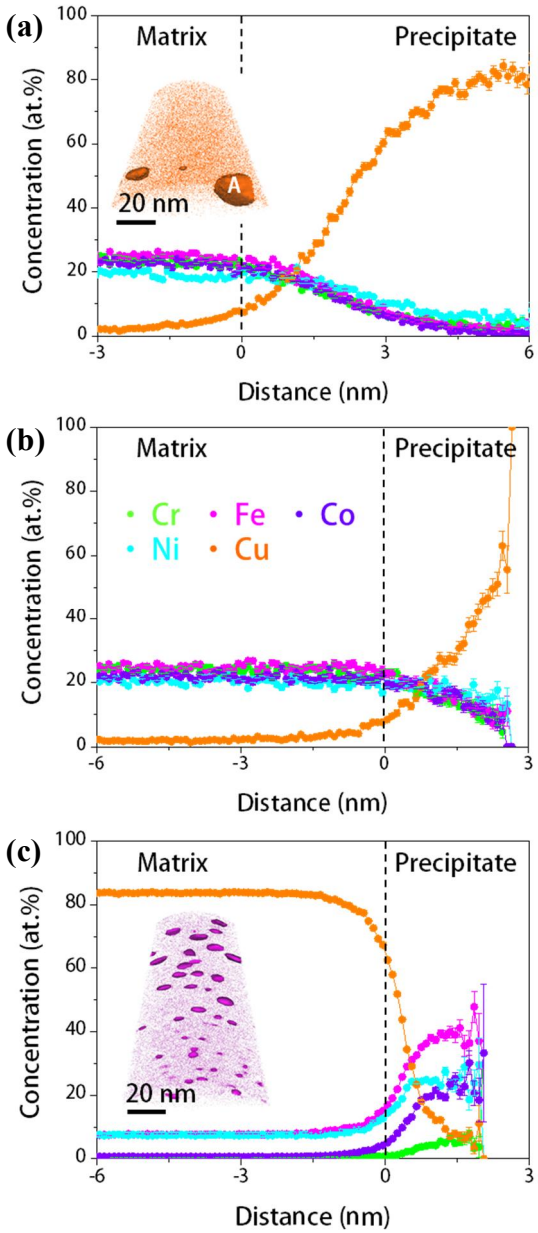

Figure 3.13 (a) APT reconstruction of the precipitates in the homogenized dendrite delineated by 8 at.% Cu and the corresponded proxigram of disk type Cu-rich precipitate and (b) the proxigram of nano-scale spherical shaped Cu-rich precipitates in the homogenized dendrite. (c) APT reconstruction delineated by 14 at.% Fe and the corresponded proxigram of nano-scale thin disk shaped CrFeCoNi-rich precipitates in the homogenized interdendrite.

precipitate in the interdendrite was not clear; however, it was confirmed that the precipitates were the thin disk shape with 8.7±1.4 nm for the width and 2.5±0.8 nm for thickness, which is determined by 1D concentration profile perpendicular to the precipitates.

The average compositions of the matrix and the precipitates in the dendrite and interdendrite upon homogenization were obtained from the proxigram in Figure 3.13 and STEM-EDS (Table 5). After homogenization, the composition of the dendritic matrix was 25.6 at.% Cr-26.6 at.% Fe-23.8 at.% Co-21.7 at. % Ni-2.3 at. % Cu that is similar with that of the as-cast dendritic matrix. In addition, the disk type and nano-scale spherical Cu-rich precipitates showed about 87.6±1.8 at.% Cu and 64.1±4.7 at.% Cu, respectively. Furthermore, the homogenized interdendritic matrix showed 1.0 at.% Cr-1.1 at.% Fe-0.8 at.% Co-7.1 at.% Ni-90.0 at.% Cu, which is determined using STEM-EDS and is quite similar with the composition of the as-cast interdendritic matrix. The composition of the homogenized interdendritic matrix, determined by APT, was little underestimated due to the instrument error. Moreover, due to the small volume fraction, the composition of the cuboidal CrFeCoNi-rich precipitates in the interdendrite cannot be investigated using APT. Instead, the composition of the cuboidal shaped CrFeCoNi- rich precipitates was determined as 24.5 at.% Cr-25.8 at.% Fe-24.9 at.% Co-20.3 at.% Ni-4.5 at.% Cu using STEM-EDS and it was similar with that in the as-cast interdendrite, indicating the precipitate growth upon homogenization not accompanied by the composition change.

Phase		Shape	V_f (%)	Analysis tool	Cr	Fe	Co	Ni	Cu
D	Matrix			EDS	20.1±1.0	25.2±1.8	28.1±7.7	21.3±3.9	5.3±1.0
				APT	25.6±0.4	26.6±0.4	23.8±0.4	21.7±0.4	2.3±0.1
	Cu-rich precipitate 1	Disk	9.3	EDS	1.1±0.4	2.0±1.4	1.6±0.8	6.6±1.1	88.7±3.0
				APT	3.5±0.7	2.4±0.8	0.8±0.4	5.7±1.3	87.6±1.8
	Cu-rich precipitate 2	Sphere	7.9	APT	4.7±2.0	10.4±2.9	8.5±2.7	12.3±3.1	64.1±4.7
ID	Matrix			EDS	1.0±0.8	1.1±0.4	0.8±0.5	7.1±1.1	90.0±2.3
				APT	0.1±0.01	7.5±0.2	0.7±0.03	7.9±0.1	83.8±0.3
	CrFeCoNi-rich precipitate 1	Cuboid	1.5	EDS	24.5±2.5	25.8±1.1	24.9±0.9	20.3±1.6	4.5±1.7
	CrFeCoNi-rich precipitate 2	Thin disk	-	APT	5.8±0.9	39.1±4.3	25.0±4.9	22.5±4.7	7.6±3.2

Table 5 Chemical compositions of the homogenized alloy measured by 3D-APT (at.%). The compositions are determined by proxigram. The errors represent the one-sigma statistical error.

Although the morphology and Cu content are different, they were both nano-scale Cu-rich FCC precipitates in CrFeCoNi-rich dendritic matrix and vice versa. As a result, the hierarchical composite structure of two phases with just one FCC crystal structure maintains from nano-scale to micro-scale even after homogenization.

3.4.2 Precipitation Evolution upon Annealing

In this section, the precipitation sequence was investigated using the morphology, size and composition of the precipitates based on the calculated phase diagram. Figure 3.14 shows a schematic diagram for the precipitation sequence in the dendrite and the interdendrite upon solidification and homogenization. Based on the phase diagram (Figure 3.10), Cu-rich phase was in the liquid state and CrFeCoNi-rich phase was in the solid state at the homogenization temperature 1100℃. At first, the elongated sphere shaped precipitates in the as-cast dendrite was largely changed into the disk shaped precipitate by the growth upon homogenization. Furthermore, the spherical precipitates with nearly 28 nm for diameter were evolved in the solid dendrite due to solubility change. Secondly, the cuboid precipitates in the as-cast interdendrite was grown into the cuboidal shaped precipitates with approximately 63 nm for length. Additionally, the nano-sized thin disk shaped phase was precipitated in the Cu-rich interdendritic matrix, resulting from the solubility change upon homogenization.

Growth rate of the precipitates is one of the evidence for the sluggish diffusion in HEAs. From obtained information in this study, the growth rates of the precipitates at 1100℃ were calculated.(Table 6) Before that, it was assumed that the precipitate is not grown under heating and cooling, suggesting the precipitate grows only for 24 h at 1100℃. For the dendrite, the precipitates with 9 nm of diameter were grown to 128 nm for the width and 47

nm for the height and then, the growth rates along and perpendicular to the disk were 0.83 Å/min and 0.26 Å/min, respectively. Furthermore, the cuboidal shaped precipitates in the interdendrite were grown from 29 nm to 64 nm upon homogenization and, consequently, the growth rate is 0.24 Å/min. Thus the growth rate of the incoherent interface was 3.5 times that of the coherent interface. According to the ref. [70], the FCC Co-rich precipitates were formed in a Cu-1 at. %Co alloy with FCC structure after aging at 800℃ and, as a result, the growth rate showed the range between 0.38 Å/min and 1.11 Å/min. The growth rate in this study was lower compared with that of the precipitates in the Cu-1 at.% Co alloy, which means the sluggish diffusion of the CrFeCoNiCu HEAs.

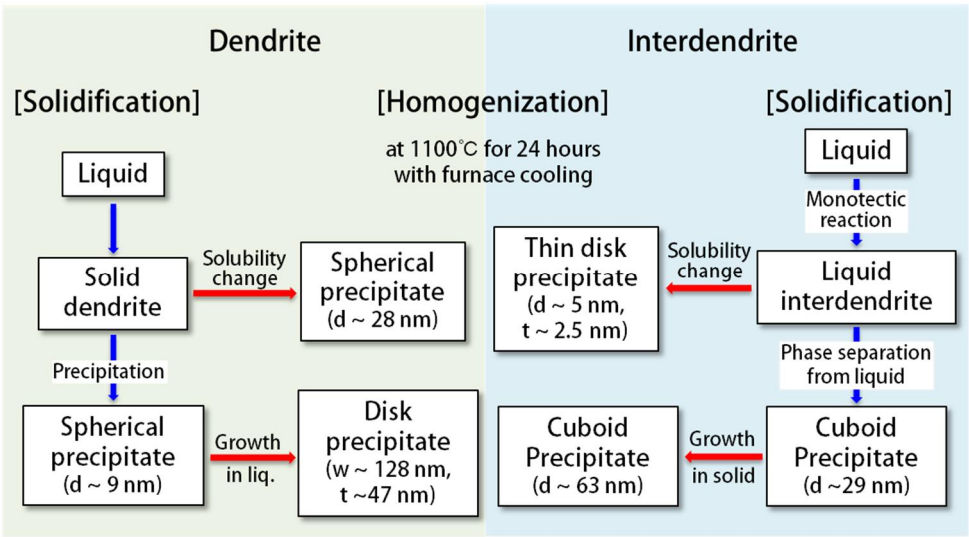

Figure 3.14 Precipitation path at the dendrite and the interdendrite of CrFeCoNiCu HEA upon homogenization at 1100℃ for 24 hours with furnace cooling.

	Dendrite			Interdendrite	
	As-cast	Homogenized		As-cast	Homogenized
Precipitate morphology	Elongated sphere	Disk		Cuboid	Cuboid
Precipitate size (nm)	9 (semi-coherent)	129 (semi-coherent)	47 (incoherent)	29 (semi-coherent)	64 (semi-coherent)
Growth rate (Å/min)		0.83	0.26		0.24

Table 6 Change in precipitate morphology, precipitate size, and growth rate of precipitates upon annealing.

3.5 Mechanical Responses of Solidified and Annealed CrFeCoNiCu HEA

3.5.1 The Role of Precipitation on Mechanical Property

In the previous section, the roles of the micro-scale second phase and the interface were investigated with reference to the mechanical response. Using nanoindentation tests, the mechanical properties were investigated further in the individual phases before and after homogenization. As a result, the effects of each of the factors on the mechanical responses are studied in this section. In addition, after the measurements, secondary electron (SE) images of the indents were obtained in order to assess the sites of the indents. However, due to the narrow width of the as-cast interdendritic region, despite the fact that the indents are in the interdendritic region, the deformation responses were affected by the dendritic region. Additionally, in order to study the effect of the precipitate on the mechanical response, the nano-hardness levels of pure Cu and $Cr_{24}Fe_{25}Co_{24}Ni_{22}Cu_5$ alloy were determined. The $Cr_{24}Fe_{25}Co_{24}Ni_{22}Cu_5$ alloy is abbreviated as 5Cu alloy henceforth. Cu-rich precipitates in the 5Cu alloy were not observed in STEM-EDS mapping images, and the STEM-EDS results were quite similar to those of the nominal composition (data not shown here). As a result, it was confirmed that the 5Cu alloy shows a single FCC phase without precipitates, which provides information about the matrix of the as-cast and homogenized CrFeCoNiCu HEA (Figure 3.15). Figure 3.16 and

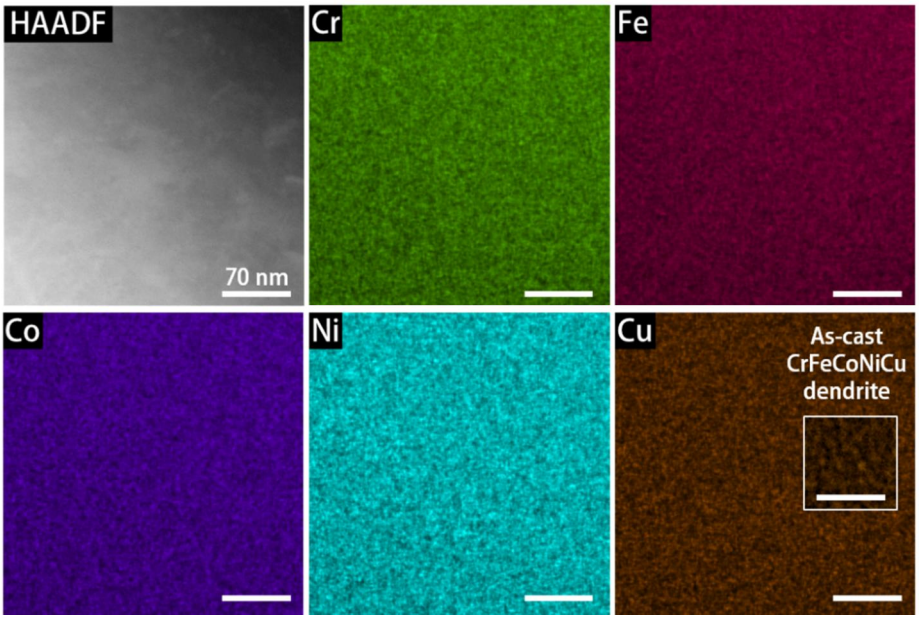

Figure 3.15 STEM HAADF image and elemental Cr, Fe, Co, Ni and Cu STEM-EDS mapping image of $Cr_{24}Fe_{25}Co_{24}Ni_{22}Cu_5$ alloy (5Cu alloy). The inset of Cu elemental image shows the chemical inhomogeneity of the dendrite in as-cast CrFeCoNiCu HEA.

Table 7 show the load-displacement curve and the nano-hardness values of each phase. The nano-hardness levels of the pure Cu, as-cast and homogenized interdendritic region were correspondingly 1.69±0.02 GPa, 2.35±0.11 GPa, and 1.79±0.07 GPa, indicating that CrFeCoNi-rich hard precipitates cause hardening. The sizes of the cuboidal precipitates increased from ~29 nm to ~63 nm in length and the volume fraction decreased considerably from 6.4% to 1.5%. As a result, thin disk-shaped GP zones formed from the interdendritic matrix. Usually, the GP zone is characterized by approximately two atomic layers for the thickness and about 10 nm for the diameter. Because extra stress was needed in order to move through the coherent zone for the dislocations, the hardness increased, and the GP zone can be utilized as a strengthening mechanism. The increased precipitate size and decreased volume fraction cause some spacing between the precipitates. Thus, the dislocations can easily bow and consequently the hardness is decreased. However, the thin disk-shaped precipitates caused the excess stress that allows the dislocations to move along the coherent interface, thus increasing the hardness. Consequently, the interdendritic phase was over-aged upon homogenization. Furthermore, the nano-hardness values of the 5Cu alloy, as-cast and homogenized dendrite were 3.08±0.18 GPa, 3.48±0.6 GPa, and 3.03±0.11 GPa, respectively. Interestingly, the soft Cu-rich precipitates can cause an increase in the nano-hardness. The spherical precipitates with diameters of approximately 9 nm increased greatly into disk-shaped precipitates with a width of approximately 128 nm and a height of nearly 47

nm. The volume fraction was 15.5% for the disk-type precipitates, which became 9.3%. The total volume fraction of the Cu-rich precipitates did not change; however, the volume fraction of the pre-existing spherical precipitates growing into disk-type precipitates decreased. As noted above, this trend for the pre-existing spherical precipitates led to a decrease in the nano-hardness due to over-aging. The nano-sized spherical Cu-rich phase precipitated from the dendritic matrix and the volume fraction was 7.9%. A GP zone formed from the interdendritic matrix upon homogenization; however, the nano-sized spherical precipitates grew from the dendritic matrix. This occurred because the vacancy formation energy of the pure Cu is low such that the vacancy concentration in the Cu-rich interdendritic region is relatively high [71, 72]. As a result, the growth of the precipitates was suppressed in the interdendritic region, in good agreement with the sluggish diffusion in the HEAs. Thus, the size, volume fraction and coherency are more important with regard to the mechanical properties than the intrinsic properties of the precipitates (Figure 3.17).

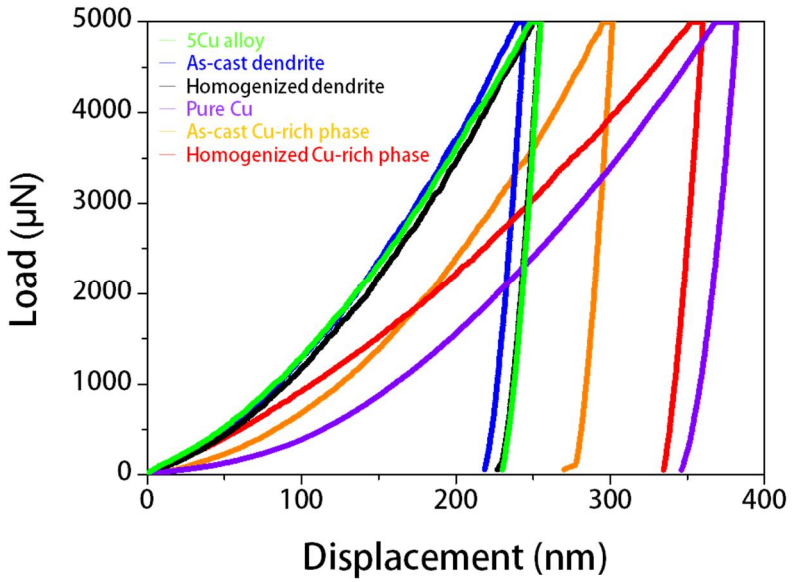

Figure 3.16 Displacement – load curves obtained from the nanoindentation tests of 5Cu alloy, pure Cu, both dendrite and interdendrite in as-cast and homogenized CrFeCoNiCu HEA.

	Dendrite			Interdendrite		
	5Cu	As-cast	Homogenized	Pure Cu	As-cast	Homogenized
H (GPa)	3.08 ± 0.18	3.48 ± 0.06	3.03 ± 0.11	1.69 ± 0.02	2.35 ± 0.11	1.79 ± 0.07

Table 7 Nano-hardness of 5Cu alloy, pure Cu, both dendrite and interdendrite in as-cast and homogenized CrFeCoNiCu HEA using nanoindentation.

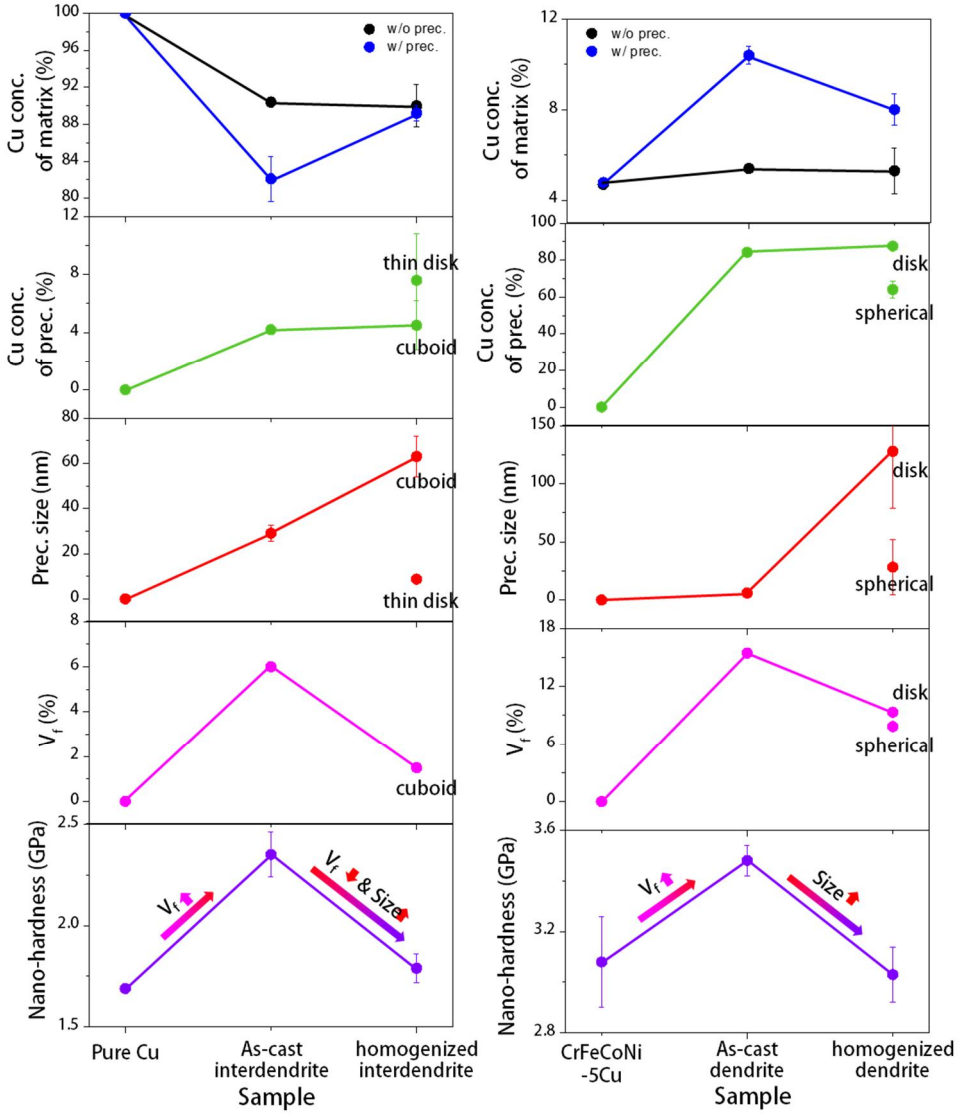

Figure 3.17 Contribution of the compositions of matrix and precipitates, precipitate size and volume fraction of the precipitates on the mechanical properties.

3.5.2 Composite Effect on Mechanical Property

In order to investigate the contribution of the soft Cu-rich phase and the misfit dislocations on the hardening properties, sub-micro-pillar compression tests were carried out. The alloys for the pillar tests were determined by $(CrFeCoNi)_{90}Cu_{10}$ and $(CrFeCoNi)_{80}Cu_{20}$, which are representative of dendrite and composite structures consisting of both dendrites and interdendritic regions, respectively. Each composition is marked by a half-open circle in purple and green in Figure 3.10. The nano-pillars oriented to the (100) plane are fabricated with a diameter of 380 nm. The pillars have higher aspect ratios (diameter to height) as compared to the ratio of 1:5 to reduce the lateral constraint [73]. Compression tests of submicron pillars of HEA were reported recently. Specifically, when the compression tests of micron pillars of CrFeCoNiCu HEA representative of a dendrite with the (100) zone orientation were performed, the pillars showed a size-dependent yield strength but were insensitive to the size effect, especially showing a multiple-slip condition [74]. Additionally, it has been reported that single-phase CrFeCoNiMn HEA with the dominant slip system of $(1\bar{1}1)[110]$ has high bulk-to-theoretical strength and hence weaker dependence of the yield strength with the diameter, resulting in low dislocation mobility [75].

Figure 3.18(a-j) presents a sequence of SEM images captured during the loading of a dendrite pillar and a composite pillar with dendrite (D) and Cu-rich interdendritic (ID) constituents at room temperature. Figure 3.18(a) and (f)

show a dendrite pillar and composite pillar consisting of dendrites and Cu-rich interdendritic regions before compression. Individual deformation processes are depicted in the extracted video frames presented in Figure 3.18(b-e) and (g-j). Figure 3.18(k) shows typical engineering stress-strain curves obtained from a dendrite and a composite pillar with a diameter of approximately 380 nm. In Figure 3.18(k),), the yield strength of the dendrite pillar is nearly 0.65 GPa at a strain rate of approximately 1.77%, in good agreement with earlier work [74]. Interestingly, the composite pillar showed the curved elastic range, suggesting that the Cu-rich interdendritic region has lower yield strength than that of the dendrite. According to the literature [76], pure Cu(100) pillars with diameters of approximately 400 nm have yield strength levels of nearly 300 MPa and show a multiple-slip condition.

The slipping process is depicted in the extracted video frames shown in Figure 3.18(b-e), which present the creation of the slip band upon compression. A single slip was initiated, as shown in Figure 3.18(c, marked by the white arrow. Then, multiple slips were continuously created with uniform deformation. It was reported that a pure Cu pillar with the (100) plane orientation shows a deformation mode transition from a single slip to alternating slips and multiple slips upon an increase in the diameter. Specifically, it has been observed that a pillar with a diameter of 400 nm shows a multiple-slip condition [76]. Interestingly, unlike the HE pillar, a slip band was not created in the composite pillar upon compression, and barreling was observed at the interface between the dendrite and the Cu-rich

interdendritic region, as illustrated in Figure 3.18(g-j). Thus, whereas the pure Cu pillar [76] and the dendrite pillar in this study show multiple slips, the composite pillar shows much more ductile behavior but has a similar yield strength level, as depicted in Figure 3.18(k).

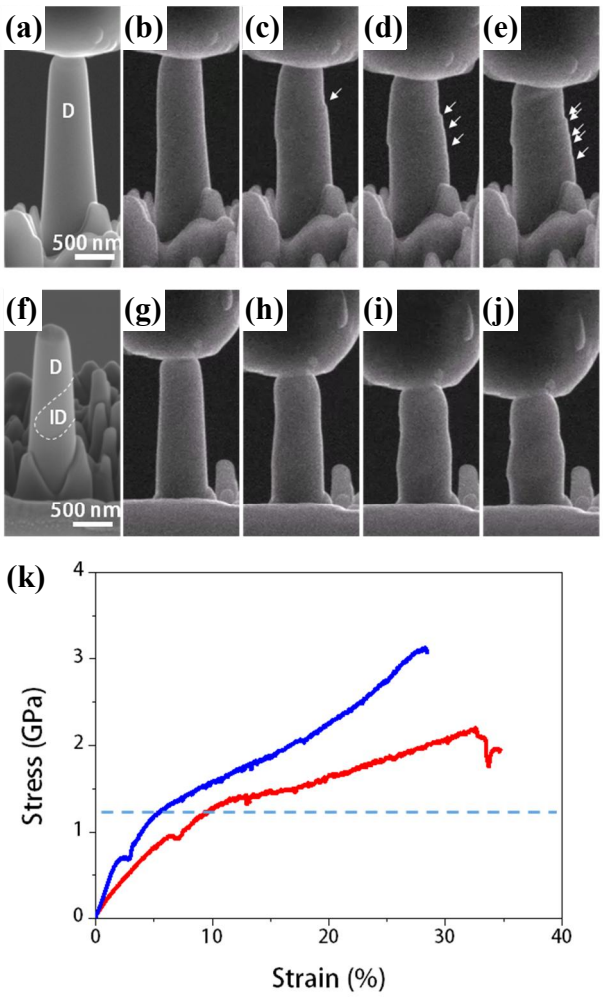

Figure 3.18 Sequence of SEM image captured during the loading of HE pillar and composite pillar with HE and Cu phase at room temperature; (a) Before, (b) 5 sec, (c) 10 sec, (d) 15 sec and (e) 20 sec for HE pillar and (f) before, (g) 5 sec, (h) 10 sec, (i) 15 sec and (j) 20 sec for composite pillar. Slip lines are highlighted by white arrows in (c-e). (k) Recorded strain-stress curves for HE pillar and composite pillar.

3.6 Summary

Multi-scale characterization with various analysis techniques was performed in this study to investigate the microstructural evolution of the CrFeCoNiCu HEA. On the micro-scale, the as-cast CrFeCoNiCu HEA showed a FCC structure consisting of CrFeCoNi-rich dendrites and a Cu-rich interdendritic region. Furthermore, nano-sized spherical Cu-rich precipitates in the dendrite and tens of nanometer-sized cuboidal CrFeCoNi-rich precipitates along the <100> direction in the interdendritic region were observed, respectively. In addition, CrFeCoNi and Cu were clearly partitioned and, interestingly, the composition of the dendritic matrix was quite similar to that of the precipitates in the interdendritic region during solidification, and vice versa. Due to the positive heat of mixing of Cr, Fe, Co and Ni on Cu, the pseudo-binary phase diagram between CrFeCoNi and Cu could be calculated. As a result, it was found that the Cu-rich precipitates were solidified from the dendritic matrix in the liquid state and that the CrFeCoNi-rich precipitates were separated from the liquid interdendritic region. Moreover, the homogenization condition was determined as 1100℃ for 24 hours based on the phase diagram. Hence, the dendrite was coarsened and spheroidized and the interdendritic area was thicker upon homogenization, sustaining the FCC structure in spite of the atomic redistribution. Moreover, the nano-sized spherical Cu-rich precipitates became disk-type precipitates and the cuboidal CrFeCoNi-rich precipitates grew into the interdendritic region upon

homogenization. Furthermore, due to the solubility change upon homogenization, tens of nanometer-sized spherical precipitates and thin disk-shaped CrFeCoNi-rich precipitates were formed in the dendrite and interdendritic regions, respectively. Additionally, the narrower PFZ near the side of the dendrite serves as evidence of the sluggish diffusion of the HEAs. Finally, the mechanical responses were investigated using nanoindentation. Regardless of the intrinsic properties of the precipitates, such as hardness, the mechanical properties were optimized in terms of the size, volume fraction and coherency of the precipitates. In this study, with the microstructure tailoring concept based on the phase diagram, the microstructure of the HEA could be controlled, which may offer insight into the excellent mechanical properties and phase stability of HEAs.

After this chapter, the radiation resistance of the dendritic phase, which is a high-entropy phase with an interdendritic phase in the CrFeCoNiCu HEA, is compared. To do this, the microstructural evolution is investigated with an increase in the scale of irradiation-induced damage (Figure 3.19). Specifically, the dynamics of defect clusters in the CrFeCoNiCu HEA are initially studied upon electron irradiation, after which the phase stability under ion irradiation, as determined by the competition between (1) radiation-enhanced diffusion and (2) ballistic diffusion, is investigated in terms of the microstructural evolution, i.e., (1) irradiation-induced grain subdivision and recrystallization and (2) precipitate dissolution.

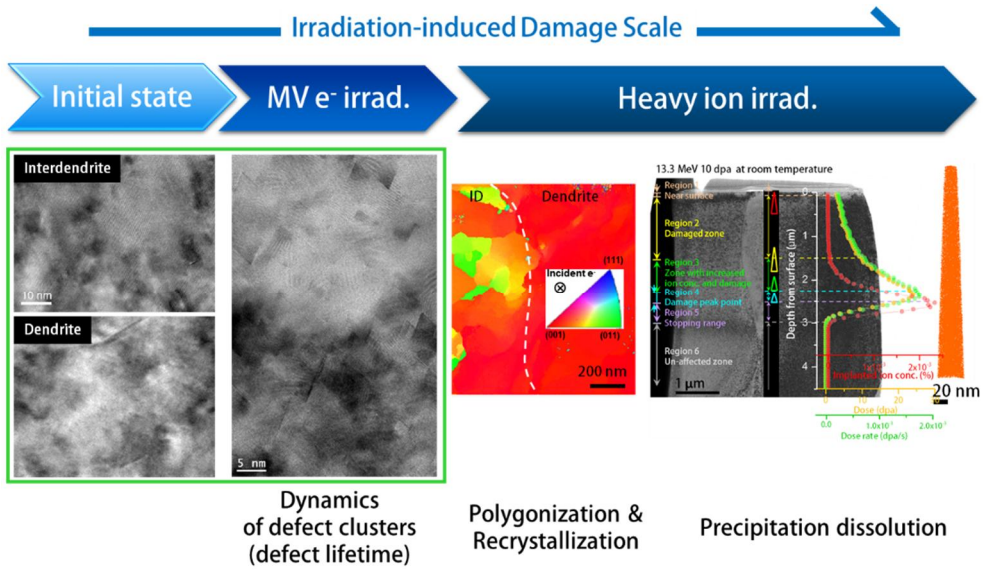

Figure 3.19 Research objectives: phase stability with increasing irradiation-induced damage scale.

Chapter 4. Kinetics of Defect Clusters upon MV Electron Irradiation

4.1 Introduction

As HEAs show complicated random atomic configurations and subsequent various atomic-scale chemical environments around atoms, they show good phase stability [77] and enhanced damage tolerance. Consequently, they have been attractive as structural materials at cryogenic and/or elevated temperatures [34, 49, 78-80] and have been applied as nuclear materials [81-95]. In practice, HEAs with high chemical complexity show excellent radiation tolerance, with useful outcomes after damage accumulation, void swelling, and radiation-induced segregation (RIS) as opposed to pure elements. In detail, with an increase in the number of alloy elements, the chemical disorder increases and, as a result, the (thermal) energy slowly dissipates in the early stage of irradiation, with few surviving defects. Furthermore, irradiation-induced void formation is attributed to the migration of interstitial clusters. Specifically, the short-range 3D motion of interstitial clusters leads to a significant increase in the vacancy-interstitial recombination rate, preventing void swelling. Lastly, the RIS is suppressed in more complex alloys due to the reduced interstitial migration caused by the lattice distortion. As noted in Section 1.3, nanostructured materials such as nanocrystalline [15, 31] as well as naolayerwd [96], nanoporous [97, 98], and nanotwinned [99-101] materials provide numerous defect sinks that reduce

radiation damage.

Given that the irradiated microstructure is closely related to the evolution of defects under irradiation, electron irradiation was performed using HVEM and the creation, annihilation, and growth of defect clusters were investigated under electron irradiation in this study. Specifically, in Section 3.2.1, both the dendrites and the interdendritic regions of the as-cast CrFeCoNiCu HEA show the FCC structure, providing evidence that both phases can be observed at the same time. Furthermore, the dynamics of defect clusters, in this case the size distribution of the defect clusters, is studied at room temperature and at elevated temperatures under electron irradiation.

4.2 Environments for Electron Irradiation

4.2.1 Dose Calculation

The electron dose rate in TEM is calculated using a detector in the form of a rectangular fluorescent plate with an accelerating voltage of 1250 kV, a convergent semi-angle and collection semi-angle of 0.5 mrad and 6.7 mrad, respectively, and magnification of 25,000. The current density measured in the detector is calibrated using a Faraday cup and a pico-ampere meter that can be inserted into the cross-over point site of the projection lens in the column. The measured beam current density is 480 pA/cm^2 without a specimen. The electron-irradiated area is approximately 3 cm in terms of the radius from the

center in the fluorescent plate, and 1 cm in the CCD corresponds to 400 nm in the real sample at this magnification. Thus, the irradiated specimen area is π x $(3 \times 400\ nm)^2 = 4.52 \times 10^6\ nm^2$ and the area of the beam current detector is 16 cm x 10 cm = 160 cm^2. Consequently, the total beam current is calculated by $(480\ pA/cm^2) \times 160\ cm^2$, where 1A = 1C/sec and 1C is $6.2415 \times 10^{18}\ e^-$. Thus, the total beam current is $4.8 \times 10^{11}\ e^-$/sec and the electron dose rate is $(4.8 \times 10^{11}\ e^- sec)/(4.52 \times 10^6\ nm^2)$, which is $1.06 \times 10^5\ e^-/nm^2 \cdot sec$.

4.2.2 Beam Heating Effect

When an electron is incident on the target material, momentum transfer by electron-ion interaction leads to atomic displacement. If the accelerating voltage is higher than the threshold energy for atomic displacement, atoms can be displaced from the original lattice sites. Furthermore, electrostatic charging indicates the primary electron absorption of an electrically insulating specimen, involving both elastic and inelastic scattering, and electron beam sputtering is a result of the sublimation of surface atoms and an electrostatic charge [7].

Most interaction of electrons with electrons results in energy losses in the form of heat generated in the irradiated material, giving rise to a local temperature increase compared to that of the surrounding temperature. The temperature increase can be defined as follows [7]:

$$I\langle E(eV)\rangle\left(\frac{t}{\lambda}\right)=\frac{4\pi\kappa t(T-T_0)}{\left[0.58+2ln\left(\frac{2R_0}{d}\right)\right]}+\pi\left(\frac{d^2}{2}\right)\varepsilon\sigma\left(T^4-{T_0}^4\right)$$

The temperature increase in an electron microscope is largely determined by the microscope conditions, the EELS spectrum, and the sample information. Influential microscope conditions such as the beam current and beam diameter are described above. The total beam current and the beam diameter here are 76.8 nA and 600 nm, respectively. The conduction length R_0 is defined by the balanced distance from the center of the incident beam diameter between the heat generation and the heat loss due to radial conduction and is set here to 1 μm. Secondly, using the EELS spectrum, the sample thickness t determined by the log-ratio absolute, the mean free path λ and the average energy loss <E> can be determined as having values of 123.4 nm, 66.8 nm, and 29.8 eV, respectively. Lastly, the emissivity of the material is assumed to be 0.3 and the measured thermal conductivity is 19.1 W/m·K at room temperature. As a result, the temperature increase ΔT is 0.24 K, indicating that specimen heating is negligible under electron irradiation at 1250 kV. Therefore, when electron irradiation is performed at 1250 kV, only the atomic displacement is considered in this chapter.

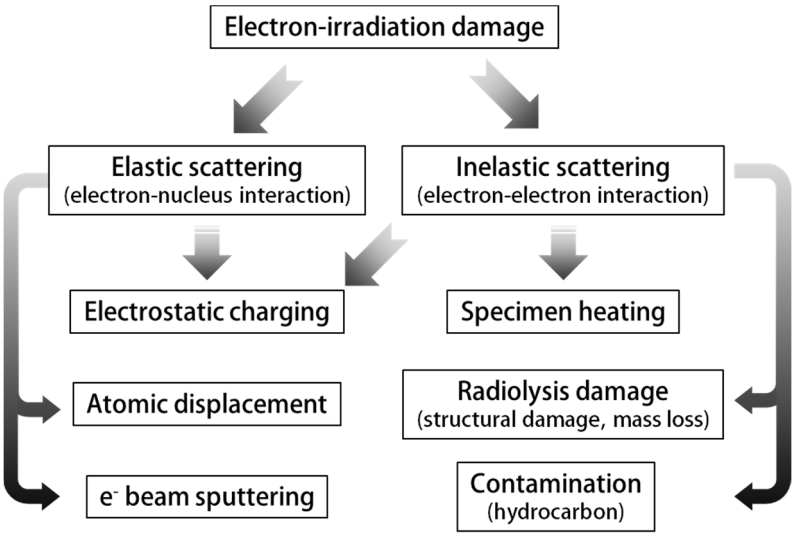

Figure 4.1 Classification of radiation damage under electron irradiation [7]. Reprinted from ref. [7] with permission through "Copyright Clearance Center".

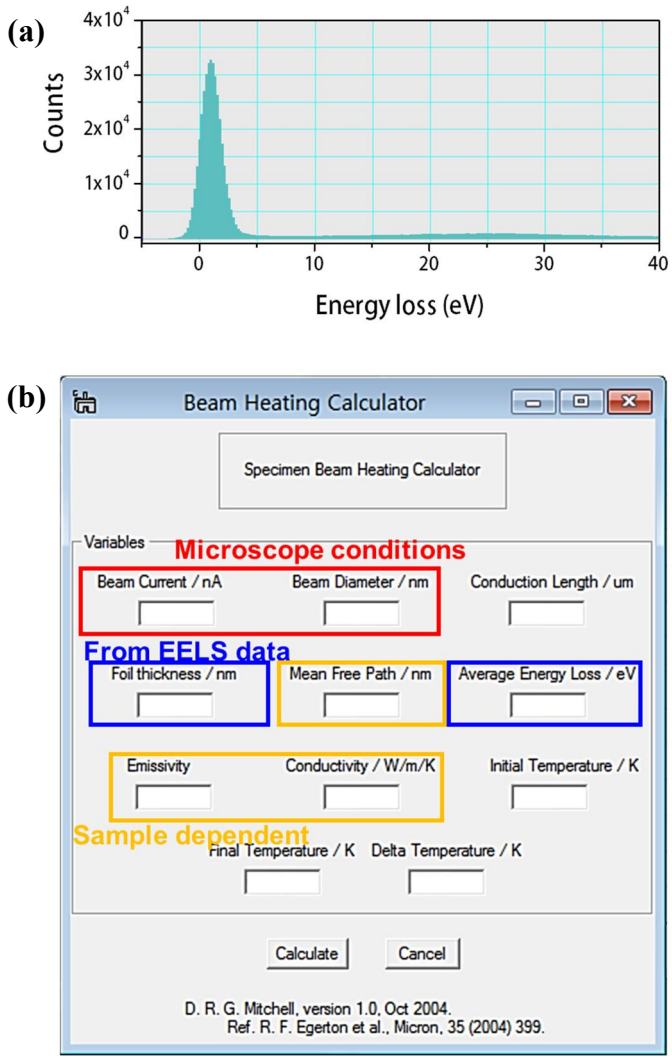

Figure 4.2 (a) EELS spectrum obtained by HVEM and (b) initial window of script 'Beam Heating Calculator' showing variables like microscope conditions, information from EELS data, and sample information.

4.3 Evolution of Defect Clusters

4.3.1 Type and Density of Defect Clusters

As shown in Figure 4.3, the type, average size, number density, and distribution of defect clusters in the dendrite and interdendritic region of the as-cast CrFeCoNiCu HEA were measured at 300 kV by a TEM. The images were obtained under a two-beam condition along diffraction vector g=<200> oriented with the [110] zone axis parallel to the electron beam. The SFTs were observed as open triangles bordered by {111} planes, and most SFTs were distributed in the interdendritic region. Dislocation loops lying on the {111} plane were visible, mainly in the dendritic region under the edge-on condition of the [110] zone axis. As a result, the dislocation loops were primarily visible in the dendritic region and the SFTs were the dominant defect clusters in the interdendritic region of the as-cast CrFeCoNiCu HEA. Unfortunately, the TEM sample was too thick for HR images to be taken. As a result, whether the defect clusters in the dendritic regions are dislocation loops or stacking faults could be investigated in detail. Accordingly, they were confirmed as dislocation loops using HVEM. The dislocation loops were quite uniformly distributed in the dendrite area; however, the distribution of SFTs was not uniform in the interdendritic region due to the imbalance of the defect concentration upon solidification. Furthermore, the average length of the dislocation loop was 8.10±4.12 nm, and the SFTs showed an average value of 2.83±0.97 nm in the interdendritic region. The number density of the

dislocation loops in the dendritic region was 7.55 x 10^{14} /m^2, while that of the SFTs in the interdendritic region was found to be 9.33 x 10^{14} /m^2, indicating two types of defect clusters in each phase with similar number densities before irradiation.

Moreover, the inside-outside contrast technique [102] was utilized to determine the nature of the dislocation loops. Using this technique, the thickness of the defects is changed by assigning a sign of g or s_g. In detail, when the s vector is changed from the positive to the negative direction, if the size of the defect decreases, the defect is considered to be extrinsic, and vice versa. As shown in Figure 4.4, with a decrease in the deviation vector s, the width of the dislocation loops increases, indicating an intrinsic type of defect cluster.

Subsequently, 1.25 MeV electron irradiation was utilized with HVEM and HR images were captured and observed near the phase boundary between the dendrite and the interdendritic regions at room temperature (Figure 4.5). The defect clusters in the shape of a very thin platelet were visible along the [111] direction on the [110] zone axis. If they are dislocation loops, extra half planes in the opposite direction appeared along the <111> direction at the center of the dislocation loops. Hence, the inverse FFT of the corresponding $(1\bar{1}1)$ and $(\bar{1}1\bar{1})$ diffraction spots in the FFT pattern (inset in Figure 4.5(b was obtained at the ROI denoted by the yellow dashed area in the figure. The extra plane observed at the end of defect clusters with b=1/3<111> is positive evidence of the dislocation loops, but they were not present at the center of

the defect clusters (Figure 4.5(c)). This occurred because the HR images were obtained too rapidly to adjust the focus to 1.5 frames/sec, even in an under-

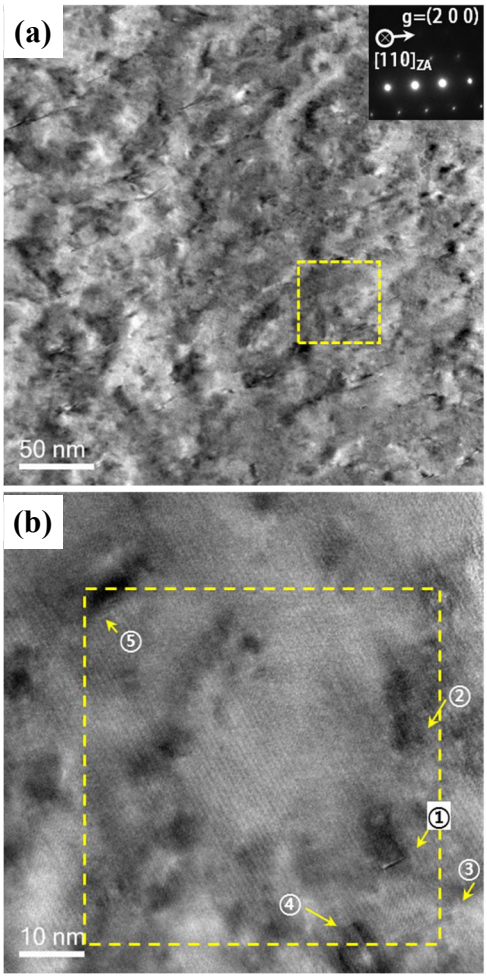

Figure 4.3 Distribution, average size, number density, and type of defect clusters in (a) the dendrite and (b) the interdendrite of as-cast CrFeCoNiCu HEA.

focus

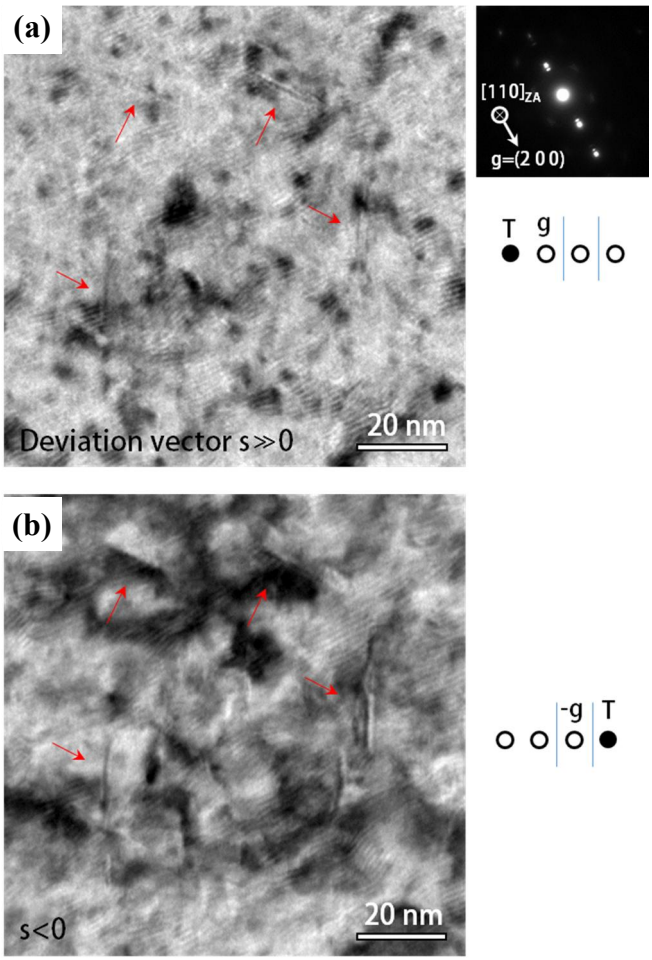

Figure 4.4 BF images at two beam condition and corresponding the SADP of (a) when the deviation vector s is much larger than zero and (b) when s is lower than 0.

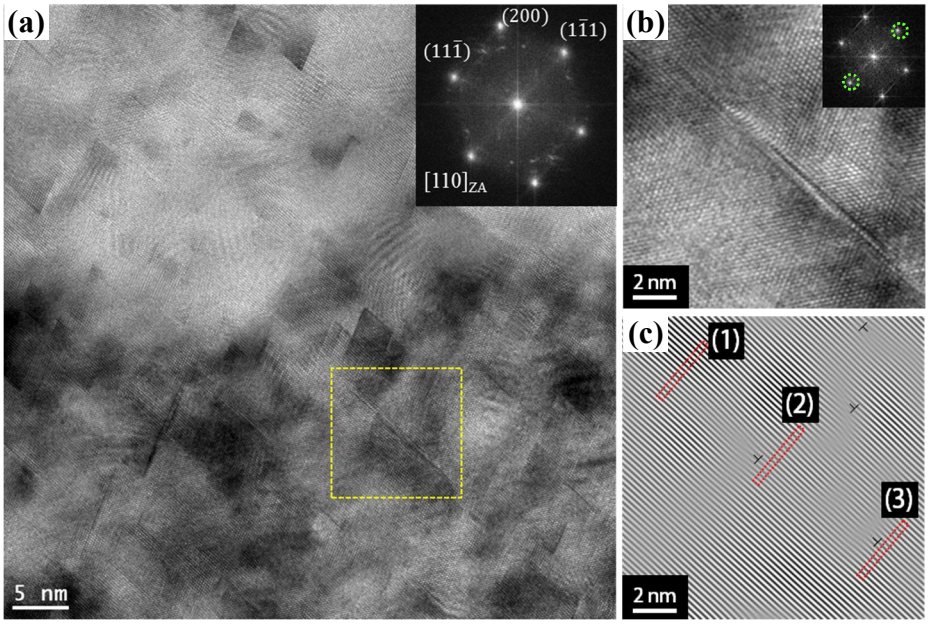

Figure 4.5 (a) HR image and corresponding FFT of electron irradiated CrFeCoNiCu HEA obtained by HVEM. (b) Magnified HR image of dislocation loop in marked area with yellow dashed line and corresponding FFT. (c) After masking spots marked by green dot line and then inverse FFT, the filtered image (b).

condition, and because the extra half planes were not easily recognized due to the strain field. Instead, the number of atomic layer with {111} plane was measured at the edge and center of the defect clusters from the intensity profile shown in Figure 4.5(b) (Figure 4.6). As a result, the number of atomic layers at the center of the defect clusters was slightly higher than that at the edge of the defect clusters, suggesting the presence of intrinsic-type dislocation loops. Therefore, it can be concluded that the dominant defect clusters in the dendritic region upon electron irradiation are intrinsic dislocation loops.

In addition, the number density of defect clusters in each phase was measured considering the irradiation time (Figure 4.7). The number density of the defect clusters is measured at the dendrites (Figure 4.7(a)) and at interdendritic region (Figure 4.7(b)) with the irradiation time using HVEM; the initial number density of defect clusters investigated at 300 kV TEM (Figure 4.3) is also indicated in Figure 4.7. The total number density is presented according to the summation of the dislocation loops and SFTs in each phase in Figure 4.7(c). It was found that the number density of defect clusters increase just after MV electron irradiation and then becomes saturated, indicating that the electron irradiation at room temperature shows a steady state. Furthermore, it was confirmed that the dislocation loops are the dominant defect clusters in the dendritic region and that the SFTs are mainly observed in the interdendritic region, similar to the findings pertaining to an unirradiated alloy (Figure 4.3). However, interestingly, SFTs were also

observed in the dendritic area and dislocation loops were visible in the interdendritic area. These phenomena can be explained by the conversion from SFT to dislocation loop [103], and vice versa in Figure 4.8. Moreover, the total number density of the defect clusters in Figure 4.7(c) was found to be quite similar to the dendrite and the interdendrite outcomes after irradiation.

As described in Section 2.5.1, after the acquisition of HR images at an average of 1.5 frames/sec, a video was created in order to show the dynamics of defect clusters in the CrFeCoNiCu HEA more clearly upon MV electron irradiation (Figure 4.9). In the video, while glissile defect clusters interacted with sessile defect clusters such as dislocation loops and SFTs, defect clusters were created, annihilated, grew, and shrunk individually.

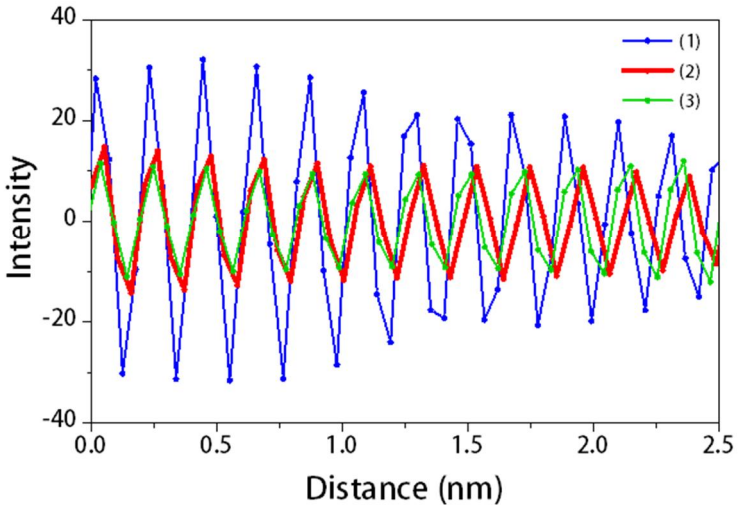

Figure 4.6 Intensity profile obtained at edge and center of defect clusters in the dendrite from **Figure 4.5**.

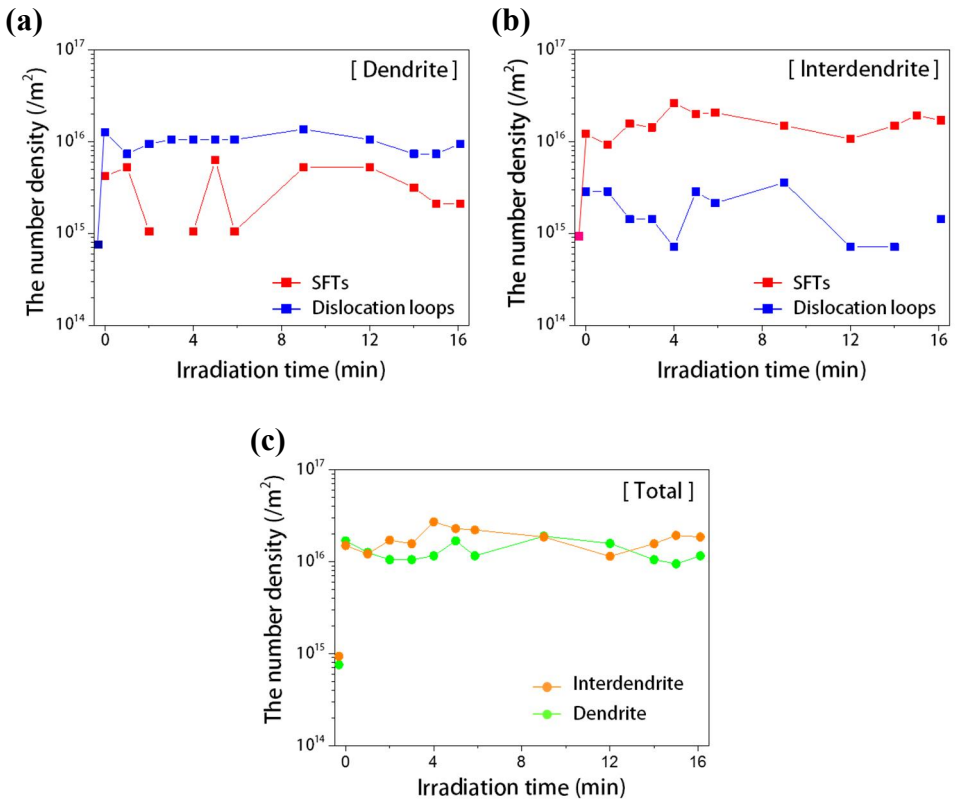

Figure 4.7 The number density of dislocation loops and SFTs with increasing irradiation time in both (a) dendrite and (b) interdendrite of electron irradiated CrFeCoNiCu HEA. (c) The total number density including all dislocation loops and SFTs with irradiation time.

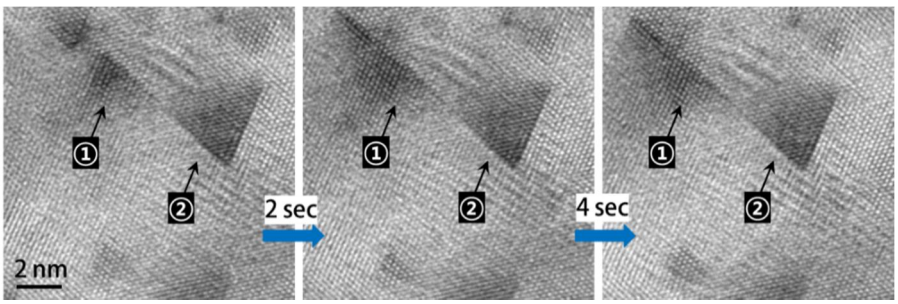

Figure 4.8 Repetitive conversion from SFT to dislocation loop and vice versa.

4.4 Growth of Defect Clusters

In the video, the defect clusters grew or shrunk upon the interaction of glissile defect clusters under electron irradiation (Figure 4.9). The growth or shrinkage of the defect clusters occurs at the Å level (Figure 4.10(a-b)), which is difficult to detect in HR images or with very rapid growth and/or shrinkage rates that are easily recognized. Consequently, the swift growth and/or shrinkage effects of defect clusters are covered in this chapter. Interestingly, the defect clusters grew rapidly or shrunk in the <111> direction. In detail, SFTs were grown or shrunk via the expansion of or contraction of a ledge along the <111> direction. Additionally, the growth or shrinkage of dislocation loops occurred along the <111> direction.

As shown in Figure 4.10(c), the similar growth or shrinkage rates of dislocation loops were likely to be independent of the matrix. Additionally, the growth rate of the dislocation loops deviated more in the interdendritic region compared to that by the SFTs. Furthermore, the average edge length of the defect clusters is presented with the irradiation time in Figure 4.11, indicating that the sizes of the defect clusters were similar even with an increase in the irradiation time, suggesting the steady state at room temperature under MV electron irradiation. This indicates that while individual sessile defect clusters grew or shrunk upon the interaction of glissile defect clusters and while the size of the sessile defect clusters fluctuated individually, the overall size of the sessile defect clusters did not

change even with longer irradiation times,

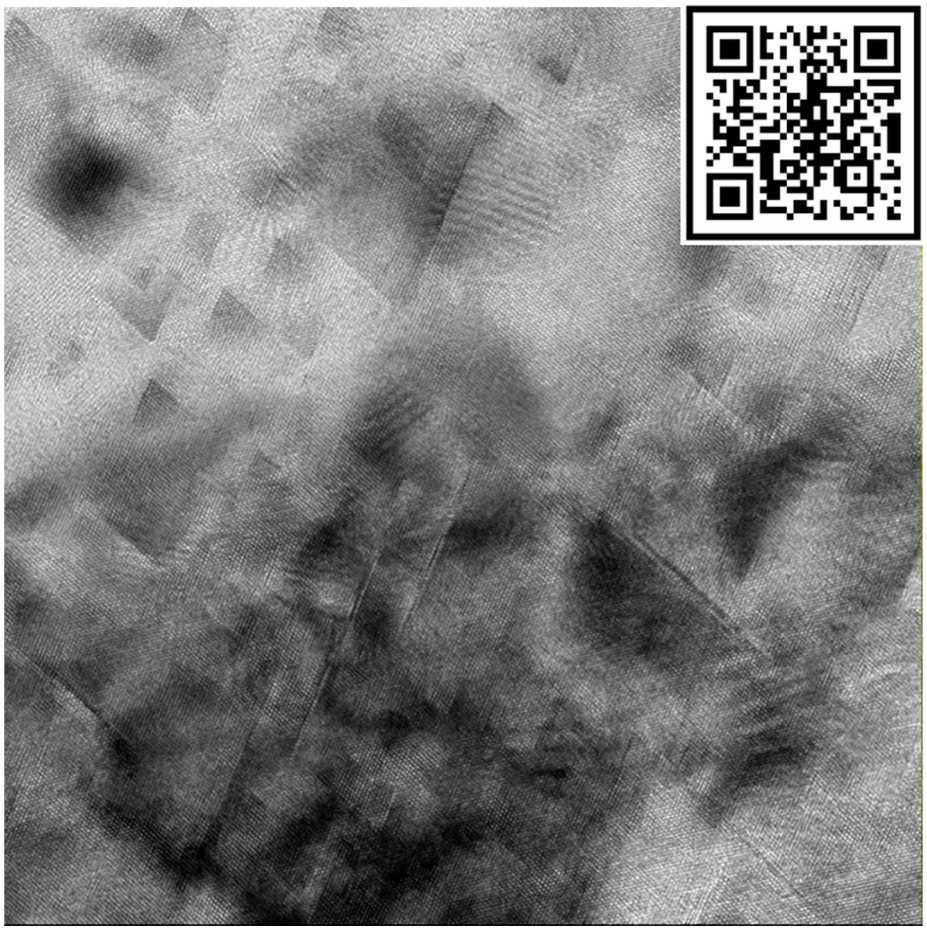

Figure 4.9 Movie for dynamics of defect clusters in CrFeCoNiCu HEA upon MV electron irradiation

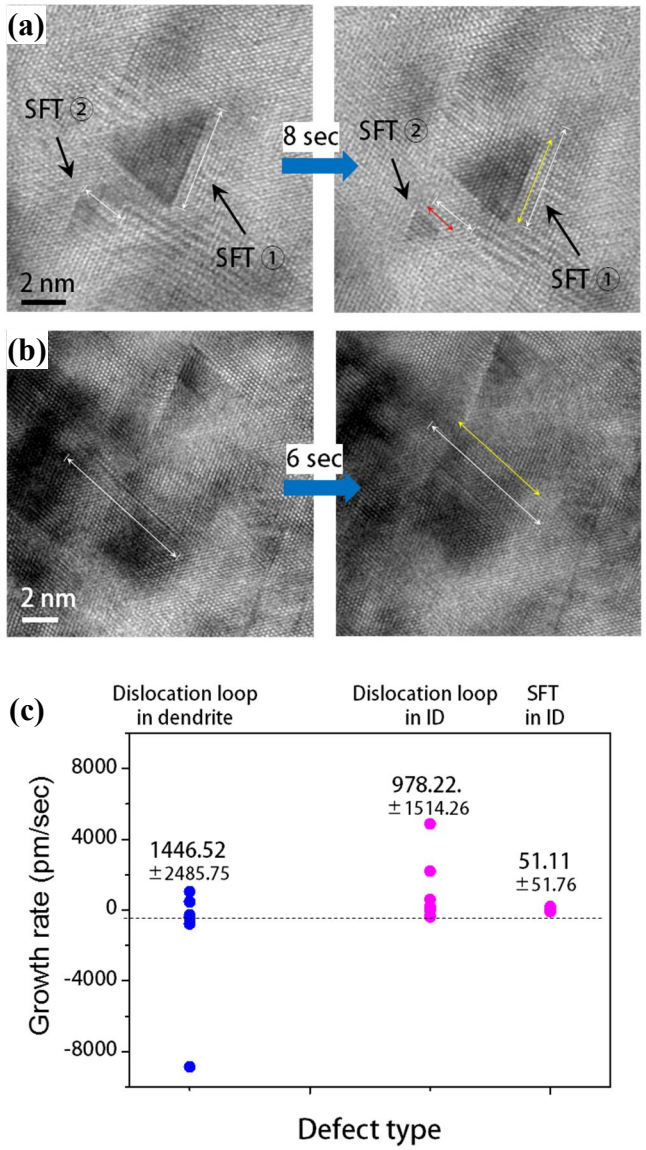

Figure 4.10 Snapshot images for growth or shrinkage of (a) SFTs in the interdendrite and (b) dislocation loop in the dendrite. (c) Growth or shrinkage rate of individual defect clusters in each phases.

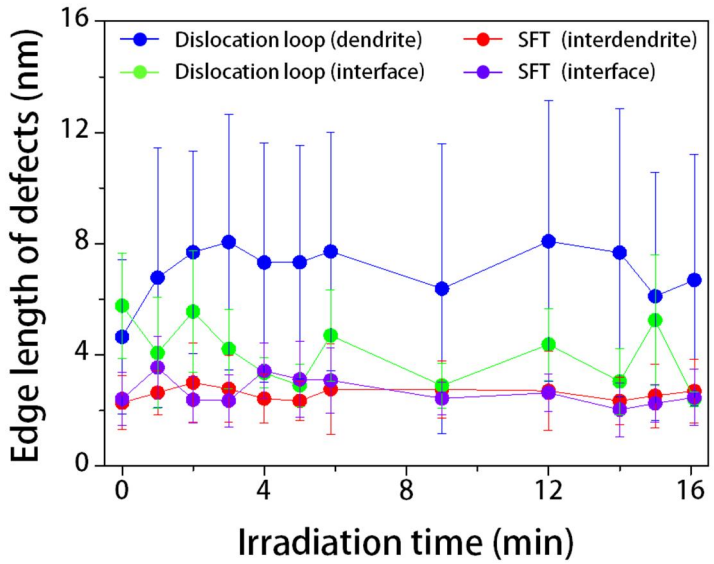

Figure 4.11 Averaged size of defect clusters in the different matrix with increasing irradiation time.

showing that electron irradiation at room temperature cannot provide sufficient energy to change the overall size of the defect clusters.

4.5 Lifetime of Defect Clusters

In order to investigate the stability of the defect clusters, the defect lifetimes were measured. A lifetime defined as the time interval during which the defect clusters are sustained upon electron irradiation. Furthermore, the defect lifetimes of dislocation loops in the dendritic regions were compared with those of SFTs in the interdendritic regions. Figure 4.12 shows representative HR images depicting the lifetimes of (a-c) SFTs in the interdendritic regions, (d-e) dislocation loops in the dendrite areas, and (f) measured defect lifetimes of individual defect clusters. As shown in Figure 4.12(a-c), two vacancy loops are created and after only 1 min, and they grew into SFTs. After a further 1 min and 56 sec under electron irradiation, one of them suddenly disappeared; however, most dislocation loops in the dendrite areas remained even after 10 min and 56 sec, as shown in Figure 4.12. In addition, the lifetimes of the sessile defect clusters are presented in Figure 4.12(f). The lifetimes of dislocation loops in the dendrite areas and SFTs in the interdendritic areas are indicated by the blue and red columns, respectively. The arrows on the tops of individual columns represent expected cases of longer defect lifetimes in practice. Specifically, these cases were relevant when the defect clusters were already in the initial stage of irradiation or when

they existed even after the observation. As a result, the lifetimes of dislocation loops in the dendritic regions were much longer than those of the SFTs in the interdendritic areas. This result suggests that the dislocation loops in dendrites are much more stable than SFTs in the interdendritic regions, thus providing evidence of enhanced radiation resistance in HEAs.

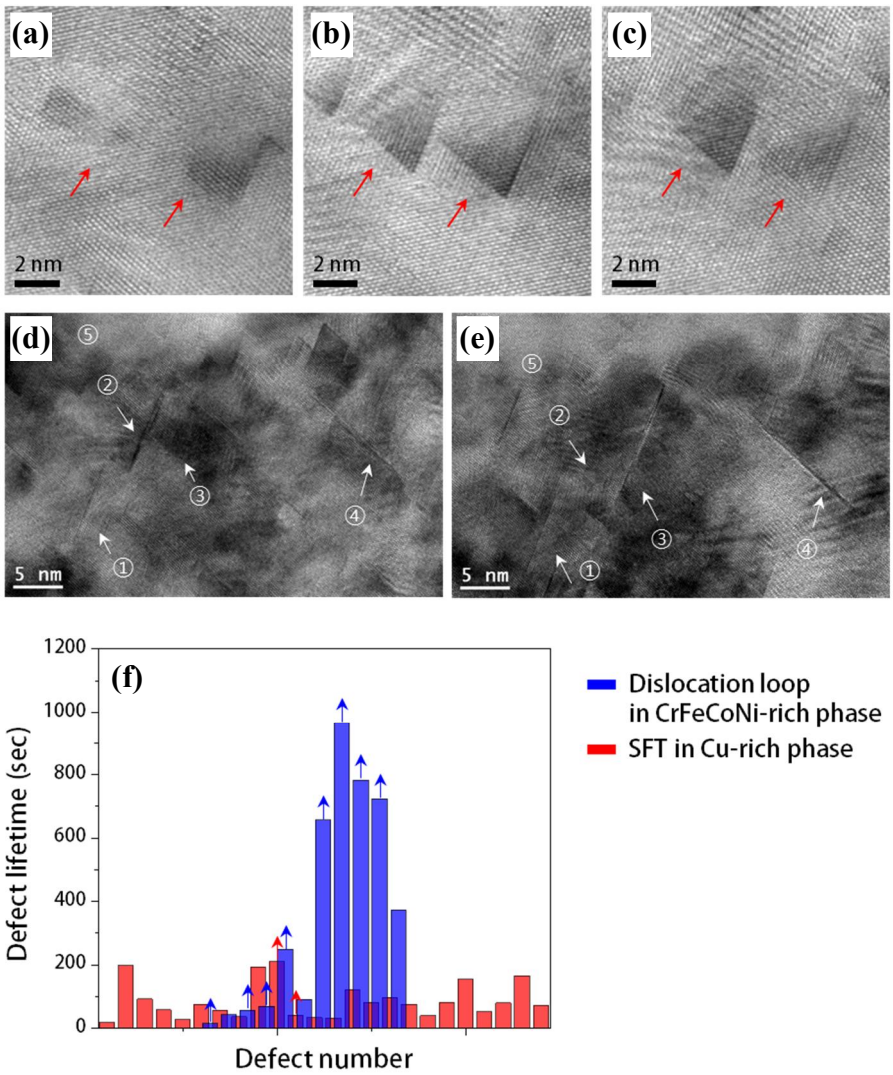

Figure 4.12 HR images of two SFTs in Cu-rich phase (a) at initial state, (b) after 1 min, (c) after 1 min 56 sec. HR images of dislocation loops in CrFeCoNi-rich phase (d) at initial state and (e) after 10 min 56 sec. (f) Distribution of defect lifetime in individual phases showing longer defect lifetime of dislocation loop in dendrite.

4.6 Evolution of Defect Clusters at Elevated Temperature

Thus far, the evolution and the dynamics of defect clusters have been investigated at room temperature under MV electron irradiation. Henceforth, the distributions of defect clusters in individual phases of CrFeCoNiCu HEA are studied at 150℃ and 400℃ under MV electron irradiation.

Figure 4.13 shows TEM BF images of defect clusters in dendritic and the interdendritic regions at 150℃ and 400℃ over a time of 30 min under electron irradiation. The dislocation loops in the dendrites are uniformly distributed even with an increase in the temperature, as shown in Figure 4.13(a-b). However, the SFTs in the interdendritic region were agglomerated and inhomogeneously distributed at 150℃ over 30 min, showing defect clusters shaped as a parallelogram as well as a defect-cluster-free region in Figure 4.13(c), respectively. The SFTs were so agglomerated that the SFTs and the dislocation loops were difficult to distinguish. Therefore, the size distribution of the defect clusters including both SFTs and dislocation loops are presented at an elevated temperature in Figure 4.14(g).

After further electron irradiation at 150℃, a BF-TEM image of the SFTs in the interdendritic region was taken, as presented in Figure 4.13(d). The defect-cluster-free area and the area in which defect clusters are agglomerated were expanded with a further increase in the irradiation time. The dislocation loops in the dendritic region showed a distribution at room temperature similar to that at an elevated temperature; however, the distribution of the

SFTs in the interdendritic region at room temperature displayed wholly different behavior from that at 150℃ under MV electron irradiation. The mobility of both interstitials and vacancies was enhanced at an elevated temperature; as a result, point defects actively interacted with the SFTs, resulting in the clustering of the SFTs.

Furthermore, in order to investigate the degree of defect stability upon an increase in the temperature under MV electron irradiation, the size distributions of the defect clusters in both phases were measured (Figure 4.14). First, the sizes of the SFTs and dislocation loops in both phases of the as-cast CrFeCoNiCu HEAs were measured in 300 kV TEM images (Figure 4.14(a) and (e)), after which the size distributions of the defect clusters were investigated at an elevated temperature under MV electron irradiation using HVEM. The defect clusters sizes in the dendrite area showed an asymmetric Gaussian distribution and were nearly unchanged, even with an increase in the temperature under MV electron irradiation. However, the sizes of the SFTs in the interdendritic region showed a fairly symmetrical Gaussian distribution at room temperature, whereas the size distributions of the SFTs were increasingly asymmetric at an elevated temperature under MV electron irradiation. These results suggest that the dislocation loops in the dendritic regions are more stable than the SFTs in the interdendritic region, even at an elevated temperature under MV electron irradiation

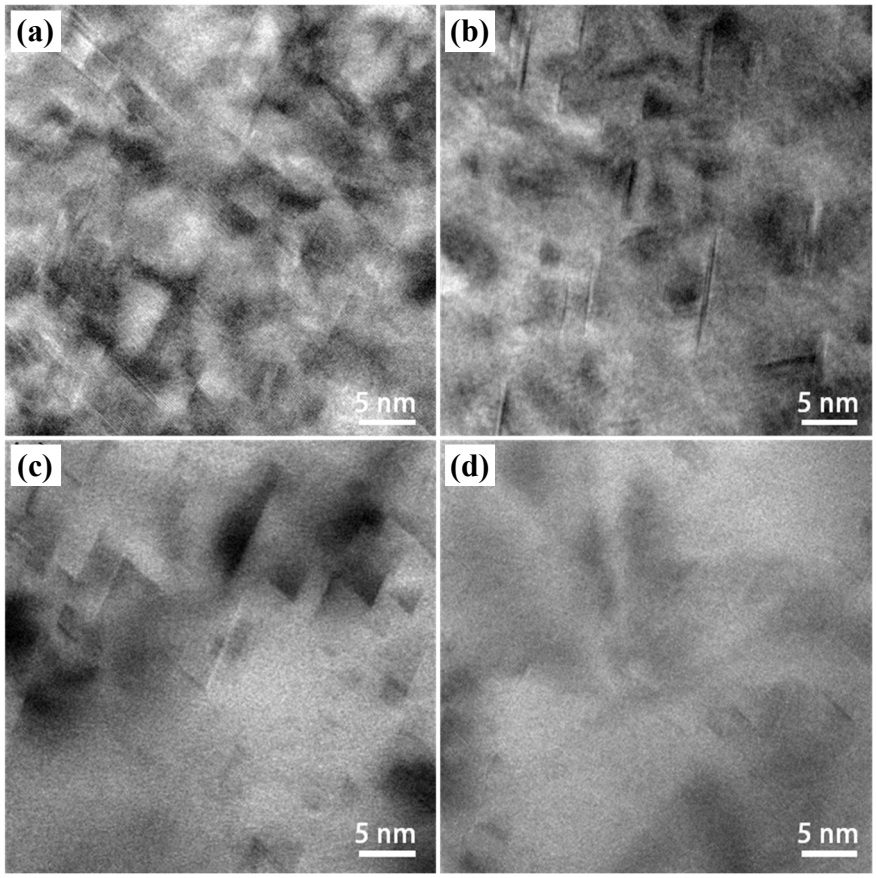

Figure 4.13 The BF images of the defect clusters in CrFeCoNi-rich phase (a) at 150℃ for 30 min and (b) at 400 ℃ for 30 min upon electron irradiation, The BF images of the defect clusters in Cu-rich phase at 150℃ (c) for 30 min and (d) for 100 min.

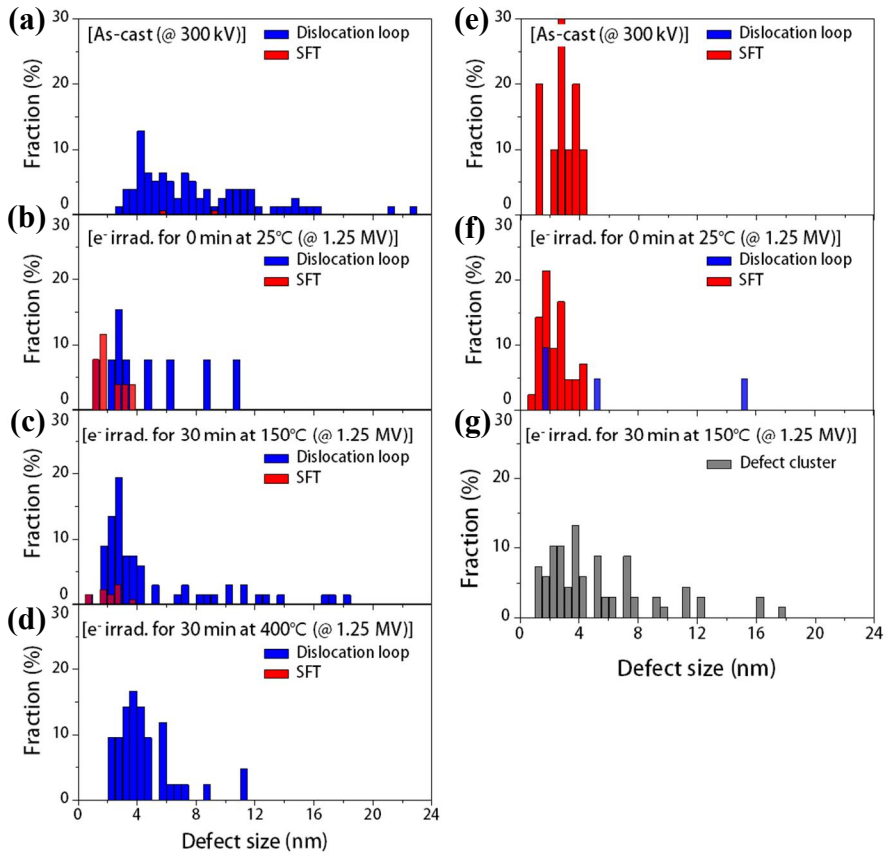

Figure 4.14 Size distribution of defect clusters in (a-d) dendrite and (e-g) interdendrite at elevated temperature.

4.7 Summary

In this chapter, the evolution and dynamics of the defect clusters of CrFeCoNiCu HEAs are assessed upon an increase in the temperature under MV electron irradiation in real time using HVEM. First, the dislocation loops were the dominant defect clusters in the dendritic area, and dominant defect clusters in the interdendritic region showed SFTs even at an elevated temperature. In addition, conversions of SFT to dislocation loops and vice versa were observed, showing that the SFTs and the dislocation loops also existed in the dendritic and interdendritic regions, respectively. Furthermore, it was confirmed that these defect clusters, SFTs and dislocation loops are all the intrinsic type. With regard to the dynamics of defect clusters, glissile defect clusters interacted with sessile defect clusters such as SFTs and dislocation loops and, consequently, sessile defect clusters were created, annihilated, grew and/or shrunk individually. With an increase in the irradiation time, the sessile SFTs and dislocation loops showed a steady state at room temperature under MV electron irradiation. Furthermore, the number density of the dislocation loops in the dendritic area was similar with that of the SFTs in the interdendritic region with the irradiation time. Additionally, individual SFTs and dislocation loops grew along the <111> direction with atomic level fluctuations or rapid growth/shrinkage rates, indicating that the growth rate of the defect clusters was independent of the matrix. In addition, the lifetimes of the dislocation loops in the dendrite were longer than those of

the SFTs in the interdendritic region, suggesting stable defect clusters in HEAs. Furthermore, the distribution of the dislocation loops in the dendrite was uniform even at an elevated temperature, unlike that of the SFTs in the interdendritic region, and the sizes of dislocation loops in the dendritic region did not change upon an increase in the temperature under MV electron irradiation. However, the size distributions of the SFTs in the interdendritic regions were broader at an increased temperature. These results suggest that the defect clusters in the HEAs are relatively stable, resulting in enhanced radiation tolerance in HEAs.

Chapter 5. Direct Observation of Irradiation-induced Polygonization and Dynamic Recrystallization

5.1 Introduction

The irradiation resistance of the materials can be evaluated not only by degradation of mechanical properties but also by microstructural changes such as radiation-induced segregation, dislocations, voids, bubbling, and swelling. Interestingly, under ion irradiation, increased compositional complexity in the HEAs resulted in suppressed damage accumulation [82, 84], mitigated segregation [86, 88-90] and restrained swelling [83, 85, 86, 91, 92].

Likewise, irradiation induces polygonization and dynamic recrystallization of the materials which are reported in various alloys systems of UO_2 [104, 105], zircaloy [106], W material [107], austenitic stainless steel [108] and Cu alloy [109, 110]. Mostly, the recrystallization was verified with orientation map by electron back scattered diffraction (EBSD), which is not enough to resolve fine grain structure unfortunately [111]. Bright field (BF) TEM imaging and corresponding selected area diffraction pattern (SADPs) analysis can visualize the fine (sub)grains[108]. However, point-by-point analysis in TEM is lack of time- and labor-efficiency and reliable statistical quantity of data. Grain orientation analysis technique using processed electron diffraction (PED) in TEM can visualize and quantify misorientation angles between nano-sized grains at one time scanning over a few micrometer range. New approach to apply the advanced technique to the irradiation research

field is expected to bring a step forward to understand the irradiation-induced recrystallization mechanism.

In this study, radiation resistance of the dendritic phase that is also high entropy phase, was examined in the microstructural point of view. As-cast CrFeCoNiCu alloy consisting of typical dendritic morphology with a CrFeCoNi-rich phase and a Cu-rich phase [112] was selected. Due to the composite structure, radiation induced microstructure evolution in CrFeCoNi-rich phase and Cu-rich phase having same crystal structure of FCC and orientation could be simultaneously and directly compared.

5.2 Irradiation Condition and Dose Calculation

Generally, displacement per atom (dpa) is widely used as standard unit for the amount of radiation damage. dpa is defined by the number of atoms displaced from their normal lattice sites as a result of energetic particle bombardment and is calculated by .

$$\text{dpa}\left[\frac{vacancies}{atoms}\right] = \frac{\text{Total vacancies}\left[\frac{vacancies}{\text{Å}\cdot ions}\right] \times \text{fluence}\left[\frac{ions}{cm^2}\right]}{Atomic\ density\left[\frac{atoms}{cm^3}\right]}$$

where total vacancies are presented by the summation of the number of vacancies formed by ions and recoil ions. The number of total vacancies is calculated via ‘stopping and range of ions in materials (SRIM) [44, 45] and the fluence is measured by ion extraction experiement. A ‘stopping and range of ions in materials (SRIM) [44, 45] (Figure 5.1) that is Monte Carlo

simultion is widely utilized in order to calculate the irradiation variables especially like the nubmer of total vacancies and implanted ion concentration profile. By controlling the type of ions, the energy of incident ions, and the incident angle to target material, and the target material, the number of total vacancies can be calculated using SRIM software. Specifically, Kinchin-Pease (K-P) model, which is the simplest, is used to calcuate atomic displacement. The K-P model is assumed that 1) when the incident energy is higher than threshold energy for displacements, the displacements are produced by a series of independent two body collisions between konck-on atoms and lattice atoms, 2) the energy transfer in the collision is based on the hard sphere model and isotropic scattering model, 3) additional energy is not needed for the atomic displacement, 4) annihilation does not occur, and 5) the atomic distribution in the target material shows not crystallographic orienation but random. These assumptions suggest the reliability issues for the calculation via SRIM software but, the issues are not considered in this dissertation.

Furthermore, the beam current for charge state of Cu ion is measured using ion extraction experiement, the current of Cu ions (Table 8). When incident energy of ions rises, the penetration depth increases and, as a result, there is advantage that the surface effect on the radiation damage decreases; however, the beam current that is the amount of extracted ions per unit time is different with incident energy of ions. So these are considered to select experimental condition.

Calculated implanted ion concentration and dpa via SRIM software

are overlapped with the cross-sectional TEM BF imge of irradiated CrFeCoNiCu HEA at room temperature and 1 dpa (Figure 5.2). The phase boundaries between the dendrite and the interdendrite are presented by white dashed lines. The TEM image was obtained with two beam bright field condition along diffraction vector g=<200> in order to see the defects effectively, so the dark contrast in the image stands for large number of irradiation induced defects. Accelerated heavy ion irradiation results in gradient damage upon the depth. The implanted Cu ion concentration increased gradually to become maximum at the depth of 2.6 μm and the associated damage was expected to be most severe around 2.4 μm. Passing the peaks, both decreased significantly and stopped at the depth of 3.0 μm where the dark contrast disappears. So it was confirmed that the calculated damage depth matches well with the experimental results. Based on the contrast in the BF-TEM image, the surface of the irradiated sample could be divided by three regions along the depth direction; grain-refined zone, damaged zone and un-affected zone.

So it is necessary to compare the microstructure evolution of the dendrite and the interdendrite simultaneously at a given depth to evaluate the irradiation resistance of the two phases.

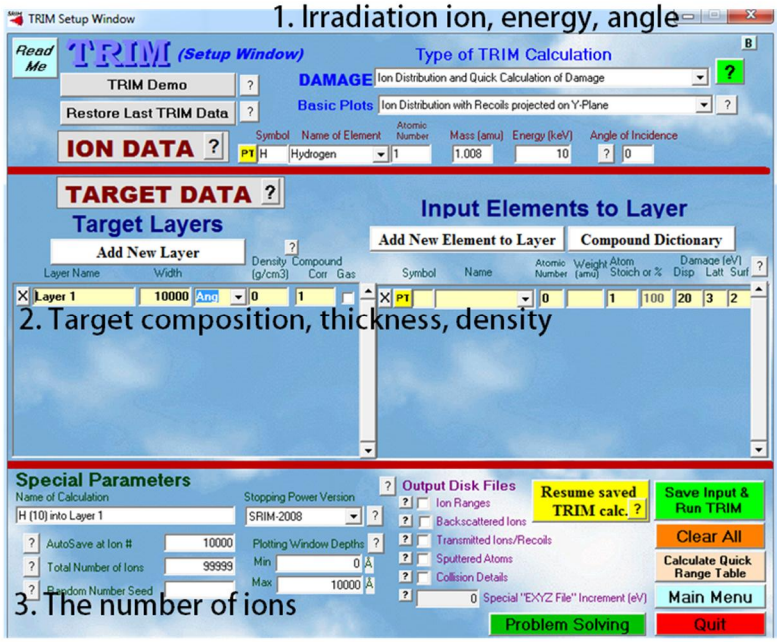

Figure 5.1 Screen in the beginning of TRIM setup window showing the variables like type, energy, and incident angle of ions, target information and so on.

Ion energy (MeV)	Charge state	magnet current	sample holder (nA)	Faraday cage when 4.5 μA (nA)	Faraday cage convert to 3.4 μA (nA)
5.7	2+	85.24	450	1000	756
7.6	3+	65.35	650	1250	944
9.5	4+	54.61	430	750	567
11.4	5+	47.71	220	420	317
13.3	6+	42.83	120	175	132

Table 8 Cu ion extraction experimental results in order to calculate the fluence using 2 MV Tandem accelerator.

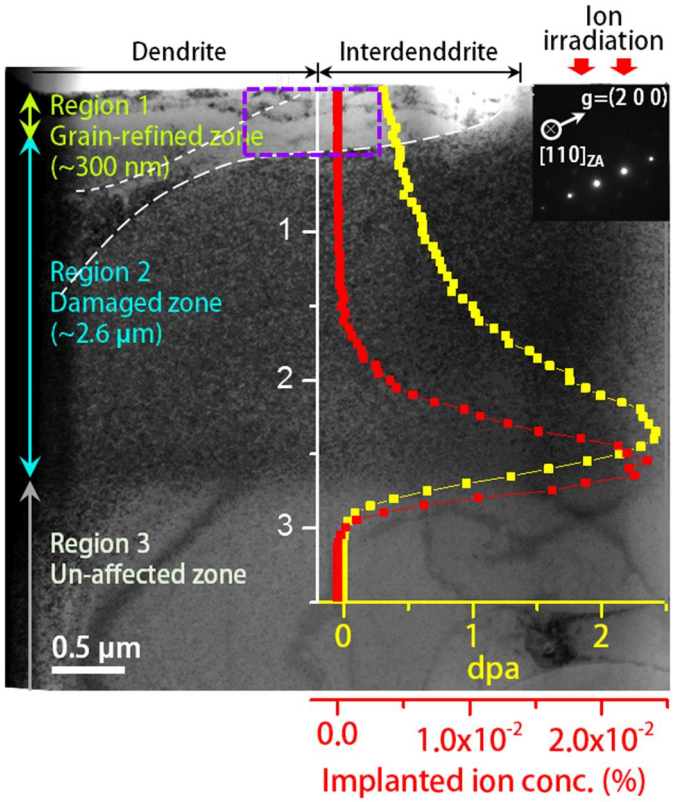

Figure 5.2 Cross-sectional BF-TEM image of irradiated CrFeCoNiCu HEA at room temperature and 1 dpa. This image is obtained with two beam condition along diffraction vector g=<200>. The dpa and implanted ion concentration are overlapped in the cross-sectional image. The white dashed line in the image indicates the phase boundary between dendrite and interdendrite.

5.3 Microstructural Evolution of Ion-irradiated CrFeCoNiCu HEA

5.3.1 Surface Morphology

Microstructure in the region 1 in Figure 5.2 was further analyzed along plane-view direction. First, the plane-view secondary electron (SE) images from surface microstructure of the dendrite and interdendrite were compared in Figure 5.2. As-cast CrFeCoNiCu alloy showed a typical dendritic structure with interdendritic Cu-rich phase (Figure 5.2). In the initial state, dendrite phase showed darker contrast in the SE image, but interdendritic Cu-rich phase became relatively darker after ion irradiation. It is supposed to be due to topographic and density change, considering the chemical composition of the phases would remained even after irradiation. Additionally, the Cu-rich phase swollen up and became porous, while the dendrite remained unchanged upon ion irradiation. So it could judge that the dendrite phase exhibits relatively high irradiation resistance by simple comparison of the surface microstructure.

Irradiated microstructure about 50 nm below the surface can be seen in Figure 5.4(a). Here, the preparation of the sample at a given depth parallel to the surface was key technique which was available by picking-up a plane-view FIB lamellar [25]. The Cu-rich phase still remained porous and deteriorated phase boundary was also observed. So it could be predicted that diffusion at the boundary occurred actively during irradiation. Going deeper about 200 nm from the surface by further FIB milling, the Cu-rich phase was

not porous anymore, but showed non-uniform contrast which is an indication of different crystallographic orientation in Figure 5.4(b).

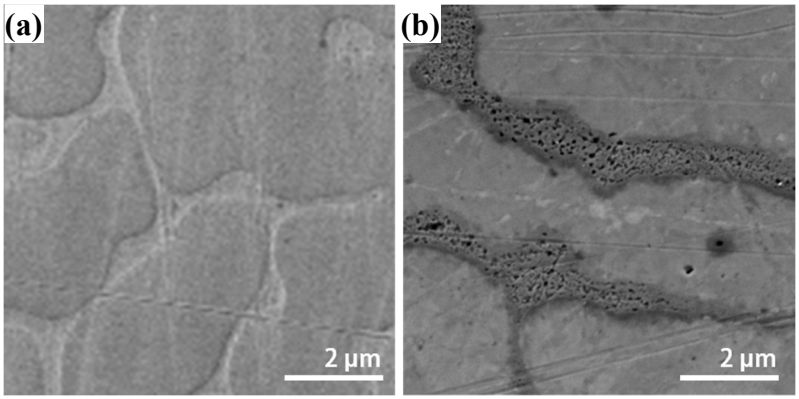

Figure 5.3 Surface morphology of (a) as-cast and (b) ion-irradiated CrFeCoNiCu alloys. The SE images showed contrast conversion of the dendrite and interdendrite after irradiation.

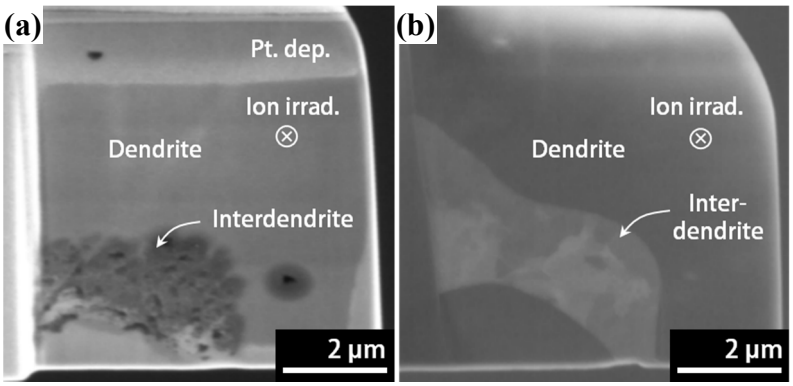

Figure 5.4 Plane-view SE images of (a) front side (near surface) and (b) back side (relatively far from the surface) of the lamellar.

5.3.2 Quantified Irradiation-induced Polygonization and Recrystallization near Surface using PED

In Figure 5.4(b), the grain subdivision and recrystallization showing the different crystallographic orientation are expected upon ion irradiation. Firstly, the grain subdivison and recrystallization are investigated via the cross-sectional TEM BF image (Figure 5.2) and purple dashed box region in Figure 5.2 is magnified in Figure 5.5. As a result, they occurred approximately below 300 nm from the surface in Cu-rich phase, showing faceted subgrain structure. Unfortunately, the morphology of sub-grains is difficult to be recognized due to lots of dislocations. Thus, sub-grain morphology and the misorientation between sub-grains are studied using PED. Figure 5.6(a) shows cross-sectioned STEM-annular dark field (ADF) image of irradiated CrFeCoNiCu HEA. The white dashed line indicates the phase boundary between the dendrite and the interdendrite. Viewing direction, which is electron-incident, is same with z direction in PED system. Additionally, the x axis in PED system corresponds to the normal direction (ND) of the sample. In order to clearly show grain morphology, the orientation maps along x axis and z axis in PED system are displayed in Figure 5.6(c-d). In the dendrite, the sub-grains are not formed but, in the Cu-rich phase that was single grain in as-cast state, shows grain subdivision followed by dynamic recrystallization after irradiation and the morphology of sub-grains are lath shaped.

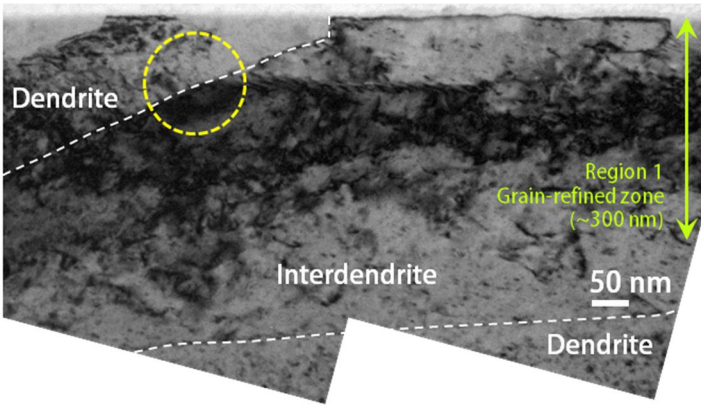

Figure 5.5 The magnified image obtained from the purple dashed area and green colored double arrow indicating the region 1 marked in **Figure 5.2**.

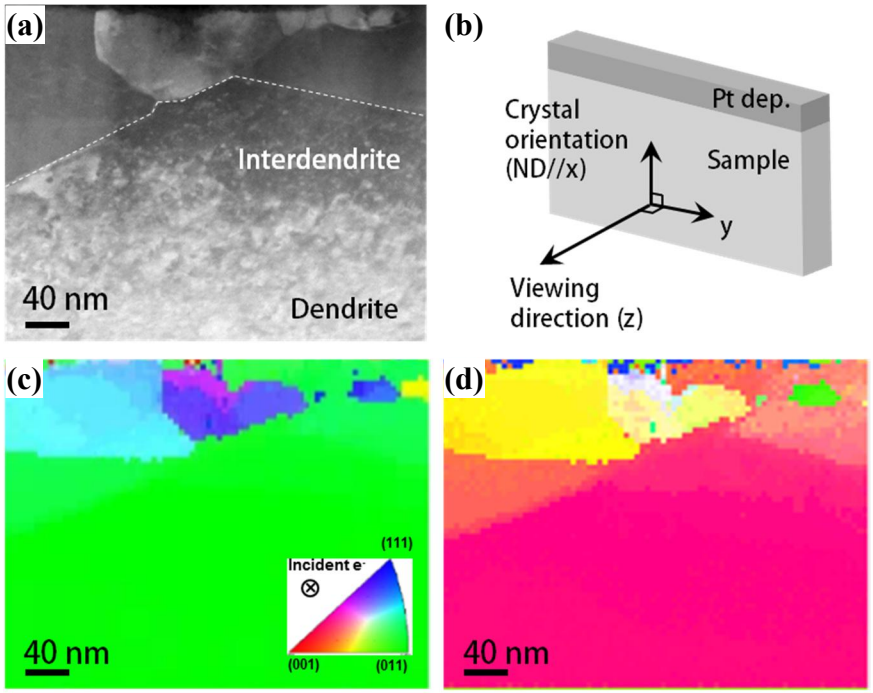

Figure 5.6 (a) Cross-sectional STEM-ADF image of irradiated CrFeCoNiCu HEA at room temperature and 1 dpa. (b) Schematic diagram of specimen coordination and PED coordination. An orientation maps along (c) viewing direction (z axis) and (d) normal direction (ND).

Microstructure in the region 1 in Figure 5.2 was further analyzed along plane-view direction. Using the plane-view TEM sample preparation, the microstructure can be easily investigated at the sampe depth in gradient material. The recrystallized microstructure about 200 nm below the surface was further analyzed using TEM. Interestingly, the irradiated Cu-rich interdendrite was not single grain, but fine grains were developed (Figure 5.7(a)). A SADP of the dendrite obtained from [110] direction exhibited slightly elongated diffraction spots which is an evidence of subgrains with low angle boundary (Figure 5.7(b)). But the SADP obtained from Cu-rich phase (Figure 5.7(c)) showed extra spots except the [110] spots, suggesting that the grains have high angle boundaries.

In order to understand the recrystallization behavior in the two FCC phases, the grain structure was mapped using PED. Inverse pole figure (IPF) maps (Figure 5.7(a-b)) was acquired from the yellow dashed box area in Figure 5.7(a). Figure 5.7(a) and (b) are obtained along z axis and x axis in PED system shown in Figure 5.6(b). The diffraction pattern showing (111) plane with dominant crystallographic orientation in the dendrite and the Cu-rich interdendritic phase was well corresponds to Figure 5.7(a). Furthermore, refined grains with different crystal orientation were clearly visualized in the Cu-rich interdendritic region. While the dendrite presented sustained grain structure, indicating relatively enhanced phase stability against ion irradiation compared to the Cu-rich phase. In order to evaluate the misorientation quantitatively, line profile across the phase boundary was acquired in Figure

5.7(c). In the dendrite region, only low angle boundary were observed. The angle between point ‘A’ and ‘B’ was 4°, and just a small hump was detected between ‘G’ and ‘H’. The low angle boundaries are evidence of subgrain formation by creation and coalescence of dislocations under irradiation [104, 105]. Whereas, abrupt orientation changes occurred in the Cu-rich phase. For instance, the misorientation at the phase boundary between ‘B’ and ‘C’ was 27° and the angle between ‘D’ and ‘E’ was 36°. In general, high angle boundary is determined as 15 to 20° [109] and subgrain is estimated under 10° tilted angle [108].

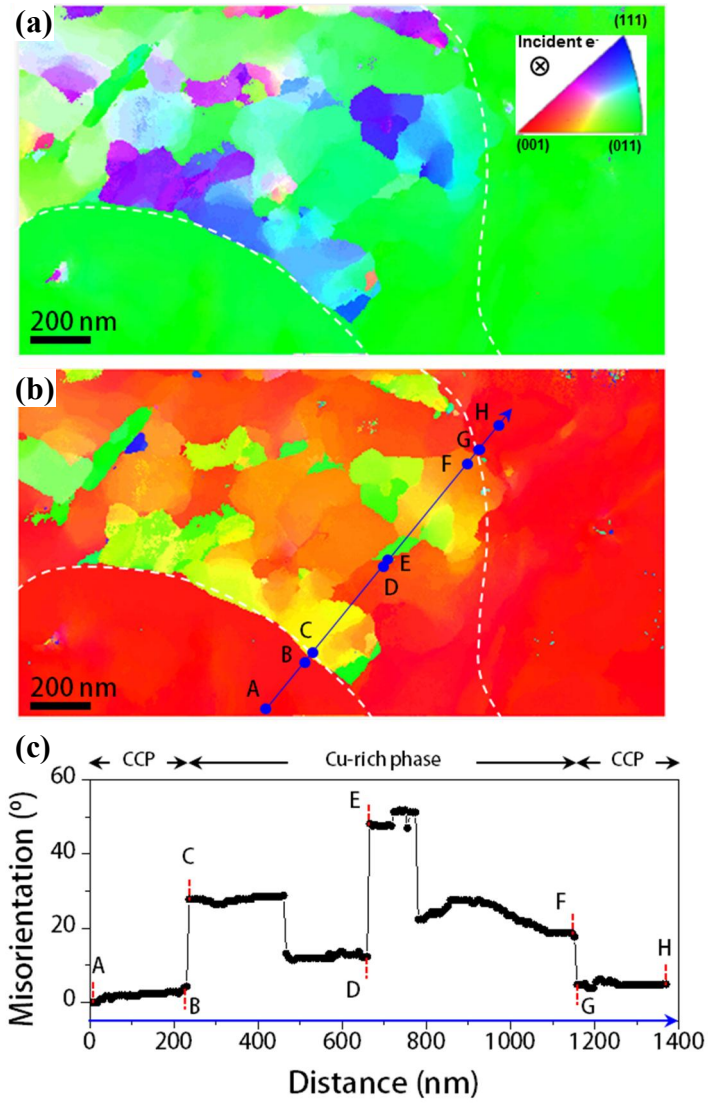

Figure 5.7 Orientation maps (a) along z axis and (b) along x axis in PED system revealing subgrain structure and recrystallization and (c) misorientation line profile along the blue line across the phase boundaries.

5.3.3 Mechanism for Suppressed Irradiation-induced Polygonization and Recrystallization in HEA

In order to investigate recovery effect by the irradiation-induced recrystallization, the GIXRD was performed. Figure 5.8 shows typical GIXRD of unirradiated and irradiated CrFeCoNiCu alloy. The effective x-ray penetration depth teff is determined by [113]

$$\frac{sin(\gamma)sin(2\theta-\gamma)}{\mu\{sin(\gamma)+sin(2\theta-\gamma)\}}$$

where γ is the X-ray angle of incidence, which is 2° in this study, and 2θ is the diffraction angle. μ is the linear absorption coefficient and the specific mass absorption coefficients for Cr, Fe, Co, Ni and Cu selected in ref. [114]. As a result, the effective penetration depth was around 200 nm. Furthermore, the peaks were identified as reflection of the FCC phase. Even after irradiation at 1 dpa, FCC phase was still sustained but, the full width at half maximum (FWHM) was decreased from 0.60° to 0. 54° at (111) plane and similarly, from 0.48° to 0.40° at (200) plane. According to the earlier work [115], dislocation, sub-boundary and internal stress affect the FWHM in XRD. When lots of dislocation are created upon irradiation, the internal stress is increased and, as a result, peak broadening is expected; however, the peak narrowing was observed in Figure 5.8. This was because the effective x-ray penetration depth of GIXRD in this study is around 200 nm, which provides the information about the grain-refined zone shown in Figure 5.2. Irradiation-induced

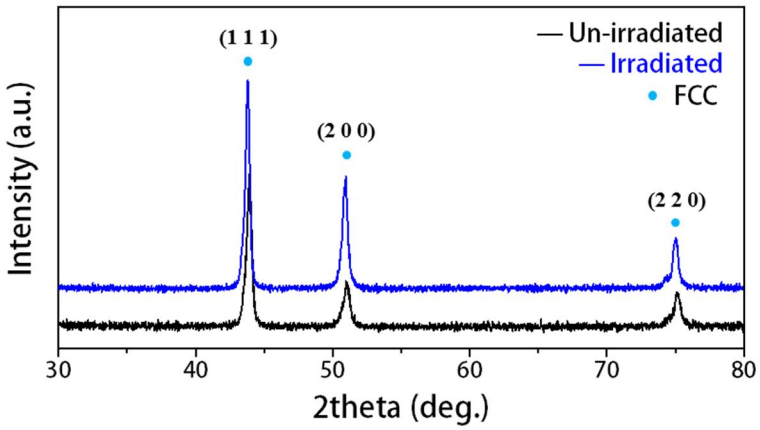

Figure 5.8 Typical GIXRD pattern from unirradiated and ion-irradiated CrFeCoNiCu HEA.

recrystallization occurred dominantly in the Cu-rich interdendrite not in the dendrite. Even though the contribution of the grain subdivision on the peak broadening in XRD is not quantitatively investigated, as the area fraction of the Cu-rich interdendrite is about 0.9, the peak broadening by the grain subdivision is negligible. Furthermore, since the implanted ion concentration was increased from 1.6 μm, peak shift by implanted ion can be negligible. In addition, dislocation climb activated by radiation-enhanced diffusion facilitated defect annihilation and, as a result, the defect amount was decreased, showing peak narrowing in XRD and quite largely recovery shown in the microstructure.

Dynamic recrystallization is defined as the nucleation and growth of new grains during deformation such as discontinuous/continuous dynamic recrystallization (DDRX/CDRX) and is affected by stacking fault energy (SFE), thermo-mechanical processing, initial grain size and so on [116, 117]. DDRX is usually observed in low SFE material like Cu, Ag, and austenitic steel. Upon straining, new strain-free grains are nucleated and grown by the expense of regions full of dislocations. Consequently, the necklace-like microstructure is observed at the boundary. Furthermore, CDRX is observed frequently in high SFE materials such as Al alloys, α-Fe and Ni. During deformation, cell or sub-structure with low angle grain boundaries are formed and the microstructure is progressively changed into high angle boundaries.

The dendritic phase in CrFeCoNiCu HEA shows sub-grain structure with low angle boundary, suggesting the CDRX. According to ref. [39], DDRX is

observed in pure Cu showing the necklace-like microstructure during compression at 573 K. In this view, it is expected that the Cu-rich phase in the CrFeCoNiCu HEA is observed with similar microstructure; however, in the Cu-rich phase, the equiaxed grains with high angle boundary were mostly observed near the phase boundary, whereas only gradual orientation tilt happened inside of the Cu-rich phase. This is a good evidence of CDRX occurred by ion irradiation. In the CDRX mechanism, new grains form by progressive increase of misorientations showing low angle boundary without recognizable nucleation. Thus grains with high angle boundary mainly form near the grain boundary where dislocation coalescence preferentially occurs. The nano-scale crystal orientation map of the plane-view surface after irradiation as shown in Figure 5.7 is a crucial key to characterize the radiation induced recrystallization mechanism.

The microstructure characterization of the CrFeCoNiCu composite with the dendrite (high entropy phase) and the interdendrite along cross-section and plane-view direction revealed that irradiation-induced degradation in the dendrite was relatively delayed. It can be discussed in terms of defect formation and recovery kinetics. Here, we would consider i) initial defect amount before irradiation and ii) subsequent recombination during cascade process, and iii) defect cluster's mobility.

(1) Initial defect amount

When an energetic ion is incident to the target material, the substantial

kinetic energy is transferred to the material and the atom is displaced from its initial lattice sites, leaving vacancy lattice sites. In the early stage of irradiation, vacancy formation enthalpy is determining terms of the radiation tolerance. It has been known that the HEAs exhibits excellent radiation resistance [81-95]. In detail, it was reported that defect accumulation was suppressed in the HEAs rather than pure Ni [82, 84]. Therefore, the vacancy formation enthalpy of the HEA is expected to be higher than pure elements. In fact, the calculated vacancy formation enthalpies was 1.89 eV for Ni vacancy in the CrFeCoNi alloy, which was higher than that of 1.41 eV for pure Ni [72] and 1.21 eV for pure Cu [71]. Thus, resulting defect density in the HEAs is lower than that in the Cu-rich phase in the initial step of the irradiation in this study.

(2) Defect recombination in the cascade

A sufficient kinetic energy of the displaced atom recoil to displace other atoms, leading to collision cascade. In addition, the kinetic energy can be converted to the thermal energy and dense collision leads to the region with extremely high temperature, called ‘thermal spike’. It is well known that the thermal spike is rapidly dissipated in the center of the cascade within a picosecond timescale, which is related to the thermal conductivity of the materials [118]. Since most vacancy-interstitial pairs are recombined in the cascade process, higher thermal conductivity of the materials provides the shorter time to recombine the defects, leads to suppressed defect

recombination and then, the amount of the survived defects after cascade process is higher. As a result, the dislocation loops can be observed in the BF–TEM image as shown in Figure 5.2.

In that context, thermal conductivities (κ) of Cu and CrFeCoNiCu alloy upon temperature were measured by laser flash method in Figure 5.9. Because the CrFeCoNiCu alloy is a composite exhibiting mixed properties of Cu and CrFeCoNi phases, $Cr_{25}Fe_{25}Co_{25}Ni_{25}$ quaternary alloy which is a single HEA [119] was also evaluated for comparison. As we expected, the CrFeCoNiCu HEA exhibited much lower diffusivity than Cu, at room and elevated temperature both. The κ of the CrFeCoNi HEA which shows pure properties of the CrFeCoNi-rich dendritic phase was the lowest in the set. Thus it was confirmed that a chemical complexity in the alloy results in the significant reduction in electron mean free path, which corresponds to decreased electrical and thermal conductivity [82]. Decreased thermal conductivity results in slow energy dissipation in the cascade and enhance the vacancy-interstitial recombination. As a result, survived defect cluster and its accumulation is suppressed.

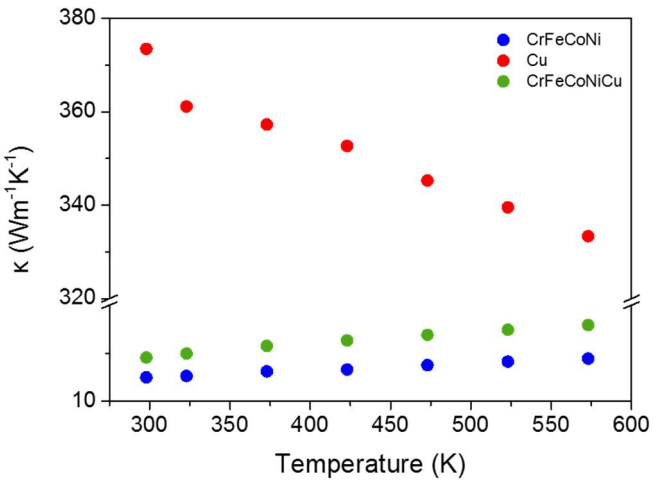

Figure 5.9 Thermal conductivity of CrFeCoNi, Cu and CrFeCoNiCu alloy.

(3) Mobility of defect clusters upon irradiation

The last thing to consider which is necessary for the recrystallization is dislocation rearrangement. Enormously created defect clusters raise up the internal stress, and thus recovery to reduce the free energy in the system occurs by dislocation rearrangement. As a product, cell structure with subgrains is developed, and then finally grains with high angle misorientation are evolved. The diffusivity under irradiation is presented by sum of thermal equilibrium term (D_{th}) and additional term due to increased vacancy concentration (D_v) [23, 120]. The dendritic phase (high entropy aphase) showed slower diffusion [13, 42], slower radiation enhanced diffusion due to the suppressed defect accumulation [82, 84] and as a result, slower dislocation mobility [121] compared to the Cu-rich phase.

Therefore, it can be concluded that high vacancy formation energy, low thermal conductivity and corresponding diffusivity in the CrFeCoNi-rich dendrite (high entropy phase) resulted in low defect concentration in the early stage of irradiation, less surviving defects after cascade reaction and slow defect mobility. Thus dislocation climb and coalescence are suppressed finally.

5.4 Summary

To summarize, CrFeCoNiCu alloy was irradiated with 13 MeV Cu ions at 1 dpa to compare radiation resistance of the CrFeCoNi-rich dendritic phase (high entropy phase) and Cu-rich phase in this study. Unlike the classical

research methods to study the irradiation induced microstructure, we utilized dual-beam FIB to observe the cross-section view and plane view of the two phases at a certain depth. Also, the microstructural evolution was visualized utilizing TEM-PED technique. Revisit to the irradiation induced microstructure evolution with those advanced analysis tools led a clear summary and a new insight. Cross-section view of the irradiated samples showed three different regions upon depth; grain-refined zone, damaged zone, and unaffected zone. The most outer region, grain-refined zone, was intensively characterized with plane-view structure. The extreme surface of the Cu-rich phase turned into porous and it recrystallized down to 200 nm below the surface. Using PED, the irradiation induced recrystallization was directly mapped in nanoscale and quantified the misorientation. High angle grain boundaries were developed mostly along the phase boundary. Peak narrowing in GIXRD and the gradient orientation in the recrystallized grain suggested that dislocation climb is activated by radiation enhanced diffusion and sub-grains and recrystallized grains are not fully recovered. So the ion irradiation seem to induce continuous dynamic recrystallization in the FCC phases of this study.

CrFeCoNi-rich dendrite (high entropy phase) exhibited suppressed microstructural degradation and thus was expected to have high resistance against irradiation. Its high vacancy formation energy decrease the defect concentration is low at the initial stage of irradiation. And low thermal conductivity and associated diffusivity favors defect annihilation, thus

surviving defect accumulation is limited. Finally, the low defect density and hindered dislocation mobility suppressed recrystallization in the dendrite. In this study, with simple comparison of the microstructure, we could double check the chemical complexity and sluggish diffusion in the dendritic phase (high entropy phase) increase the radiation resistance.

Chapter 6. Phase stability in CrFeCoNiCu HEA upon Ion Irradiation

6.1 Introduction

As described in Chapter 5, irradiation-induced recrystallization occurred in dendritic as well as in interdendritic regions of CrFeCoNiCu HEA due to radiation-enhanced diffusion. Microstructural evolution under irradiation occurs due to the competition between radiation-enhanced diffusion and ballistic diffusion [122].

Radiation-enhanced diffusion is attributed to the supersaturation of point defects, which are mainly vacancies. Therefore, the term interstitials is omitted henceforth. The diffusion coefficient of an atom is determined by the sum of the thermal equilibrium concentration of the vacancies,

$$D_{eq} = D_v C_{eq}$$

where C_{eq} is the equilibrium concentration of the vacancies at the irradiation temperature, D_v is the diffusion coefficient of a vacancy, and D_{eq} is the equilibrium diffusion coefficient in the absence of irradiation. Under irradiation, the diffusion coefficient D_{irrad} is expressed as [3]

$$D_{irrad} = D_v C_{eq} + D_v C_{irrad}$$

where C_{irrad} indicates the value of the vacancy concentration under irradiation. Because the concentrations of vacancies under irradiation are significantly greater than those produced thermally, the radiation-enhanced diffusion coefficients are much larger than the thermal diffusion coefficients. Here, it is

assumed that D_v is constant even under irradiation.

Furthermore, ballistic diffusion occurs due to collisions between irradiating particles and atoms in the target material. Qualitatively, ballistic mixing leads to more jumps of the atoms in the target material than the atomic jumps related to thermal diffusion in the absence of irradiation. In detail, according to the atomic model of thermal diffusion, the diffusivity is established as follows [23]

$$D = \frac{1}{6}\lambda^2 \Gamma$$

Here, Γ is the total jump frequency and λ is the jump length. When the distribution of the momentum transfers in the collision cascade is isotropic, the effective diffusion coefficient D* via a cumulative random-walk-like displacement process,

$$D^* = \frac{1}{6}R^2 F$$

where R is the root-mean square displacement of an atom in the collision cascade and F is the atomic displacement rate in dpa/sec. Therefore, if the number of jumps increases due to ballistic mixing, the diffusivity of an atom, D_{irrad}, is enhanced.

As described in Section 1.2 and Section 5.2, irradiation damage is affected by the dose rate as well as by the irradiating particle type, incident energy, dose and temperature. In particular, the dose rate is controlled by either the fluence, which changes with the irradiation condition, or by the

number of total vacancies, which changes with the depth. Among these two factors, the latter represents an easier means of controlling the dose rate with one sample. Thus, in Chapter 6, the dose rate effect on the precipitates upon a change of the depth is investigated. Given these outcomes, the phase stability of HEAs under irradiation is investigated in this chapter.

6.2 Irradiation Condition and Analysis from APT Data

6.2.1 Irradiation Condition and Dose Rate Calculation

As explained in Section 5.2, the dose, dpa, is established as shown below.

$$\text{dpa}\left[\frac{vacancies}{atoms}\right] = \frac{\text{Total vacancies}\left[\frac{vacancies}{\text{Å}\cdot ions}\right] \times \text{fluence}\left[\frac{ions}{cm^2}\right]}{Atomic\ density\left[\frac{atoms}{cm^3}\right]}$$

In this equation, the dose rate can be calculated by changing the fluence to the fluence per second. Moreover it is directly affected by the number of total vacancies; consequently, the trend of the dose rate with an increase in the depth is similar with that of the dose. As previously noted in Section 5.2, the current is 120 nA at 1 dpa under 13.3 MV of Cu ion irradiation. On the other hand, the current is set to 350 nA at 10 dpa under 13.3 MV of Cu ion irradiation in order to minimize the irradiation time. Consequently, the dose rates, dpa/sec, are 7.23 x 10^{-5} dpa/sec and 21.2 x 10^{-5} dpa/sec at 1.5 μm at 1 dpa and 10 dpa, respectively, as shown in Figure 6.1. These results indicate that the dose rate at 10 dpa is approximately three times the value of the dose rate at 1 dpa.

6.2.2 Precipitate Characterization via APT analysis

As mentioned in Section 2.2.6, the information pertaining to the precipitates in ion-irradiated CrFeCoNiCu HEA was gained upon an increase

in the depth using a 3D-APT device (Cameca Instruments; LEAP 4000X Si at Northwestern University) by repetitive milling followed by a data-acquisition step. These outcomes were then compared with those of precipitates in un-irradiated CrFeCoNiCu HEA using 3D-APT (Cameca Instruments; LEAP 4000X HR at KIST).

In detail, the size and the fraction of the precipitates were directly determined in three dimensions [123]. The radius, R, of an individual precipitate including n atoms in the reconstruction is identical to the radius of the volume equivalent sphere,

$$R = \left(\frac{3}{4\pi}\frac{n\Omega}{\eta}\right)^{1/3}$$

where Ω is the theoretical atomic volume and η is the estimated detection efficiency of 0.5 for the multichannel plate detector of the LEAP tomograph. The atomic volume, Ω, is calculated by

$$\Omega = \frac{a^3}{4}$$

where is the lattice parameter of the precipitate, which is determined from the XRD result. In addition, the value of 4 indicates the number of atoms in the FCC unit cell. Here, although the composition of the precipitates is changed, the lattice parameter is assumed to be unchanged upon irradiation. Additionally, the number of atoms, n, contained in an individual precipitate was determined by assessing the contents of an isoconcentration surface. The volume fraction, φ, of the precipitates was determined directly from the ratio of the total number of atoms within the precipitates relative to the total

number of atoms collected and the average atomic density of the two phases. The number density, N_v, was determined from the number of precipitates in the reconstructed volume.

6.2.3 Classification of Region in Irradiated Alloy

There were six regions defined according to the damage and the implanted ion concentration profile in more detail compared to that in Figure 5.2Initially, the region near the surface was affected by defect diffusion to the surface. Secondly, region 2 was a damaged zone characterized by an increased dose and dose rate and an unchanged implanted ion concentration. The third zone presented not only an increased implanted ion concentration but also increased damage. Region 4 showed a damage peak point, and the implanted ions stopped at region 5. Additionally, below the stopped range, the region was not affected by irradiation. Accordingly, four 3D-APT datasets were obtained from the surface to the damage peak points, as indicated in Figure 6.2.

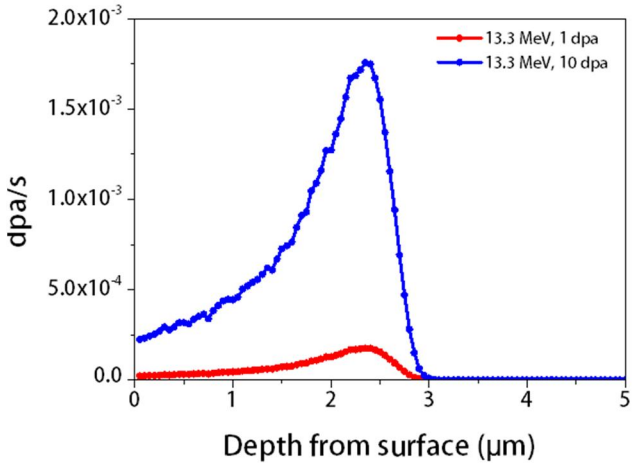

Figure 6.1 Calculated dose rate with increasing depth at 1 dpa and 10 dpa under 13.3 MV Cu ion irradiation.

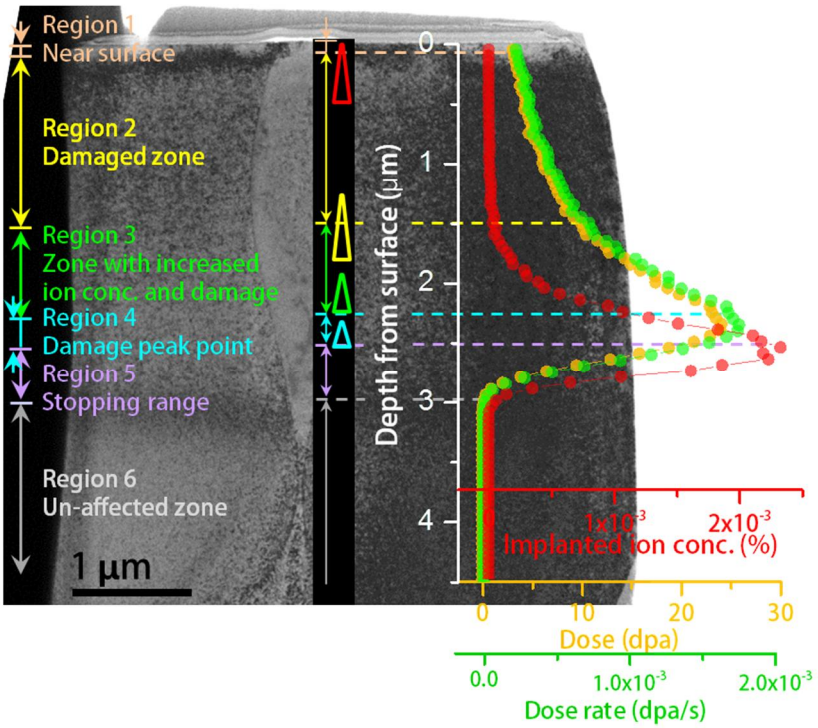

Figure 6.2 Cross-sectional TEM BF image of irradiated CrFeCoNiCu HEA at room temperature and 10 dpa. The dpa, dose rate and implanted ion concentration are overlapped in the cross-sectional image. The size and the area that reconstructed tip obtains of APT tip are marked in the image.

6.3 Precipitation Shrinkage and Dissolution under Ion Irradiation

As described in Section 3.2.2, the size, fraction, and composition of the precipitates in the dendritic area of the as-cast CrFeCoNiCu HEA were reassessed for a comparison with those of an irradiated alloy. The composition of the dendritic matrix of the as-cast CrFeCoNiCu HEA was 24.3 at.%Cr-24.7 at.%Fe-23.8 at.%Co-21.8 at.%Ni-5.4 at.%Cu, and the precipitates in the dendritic area were 4.5 at.%Cr-2.9 at.%Fe-2.1 at.%Co-6.2 at.%Ni-84.3at.%Cu, respectively. Additionally, the volume fraction of the precipitates was approximately 15% and the average size indicated a diameter of nearly 9 nm.

A 10-nm slice from the reconstruction Cu atom map in Figure 6.3 provides three-dimensional information about the precipitates from the surface to less than 380 nm. In Figure 6.3(b-c), the size and the volume fraction of the precipitates are shown to decrease significantly with an increase in the depth. Furthermore, as shown in Figure 6.4, while the un-irradiated alloy shows an 80 at.% Cu concentration, the Cu concentration of precipitates decreased to about 40 at.% with an increase in the depth upon irradiation. Additionally, it was well observed that there is chemical fluctuation and a broad interface between the matrix and the precipitate, suggesting chemical mixing during irradiation. These results provide evidence of precipitate shrinkage with an increase in the dose and dose rate.

A reconstruction atom map was then acquired from 1.62 μm to 1.85 μm

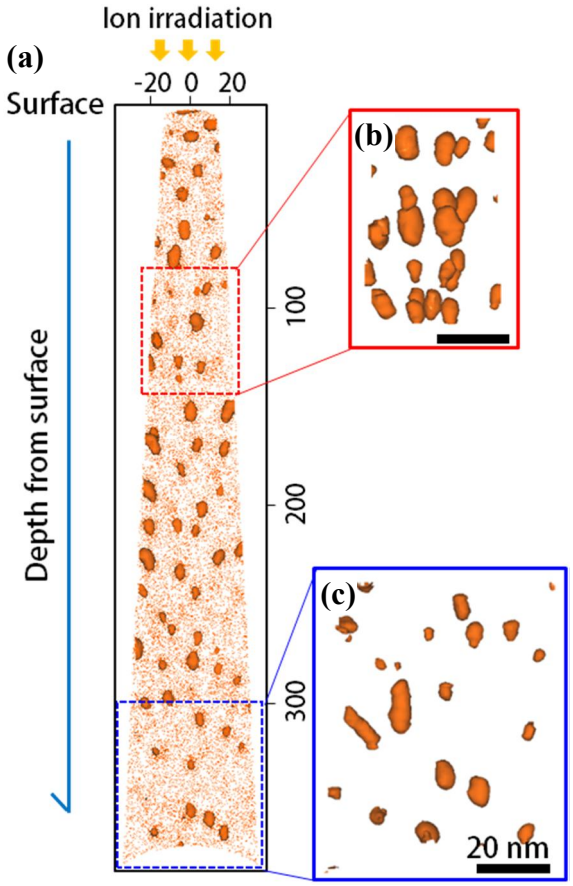

Figure 6.3 10 nm slice from an APT reconstructed Cu atom map showing the precipitates of irradiated dendrite delineated by 22 at.% Cu (a) from the surface to below 0.38 μm. Magnified isoconcentration surface images (b) from 80 nm to 144 nm and (c) 300 nm to 380 nm. Orange color (●) indicates the Cu element.

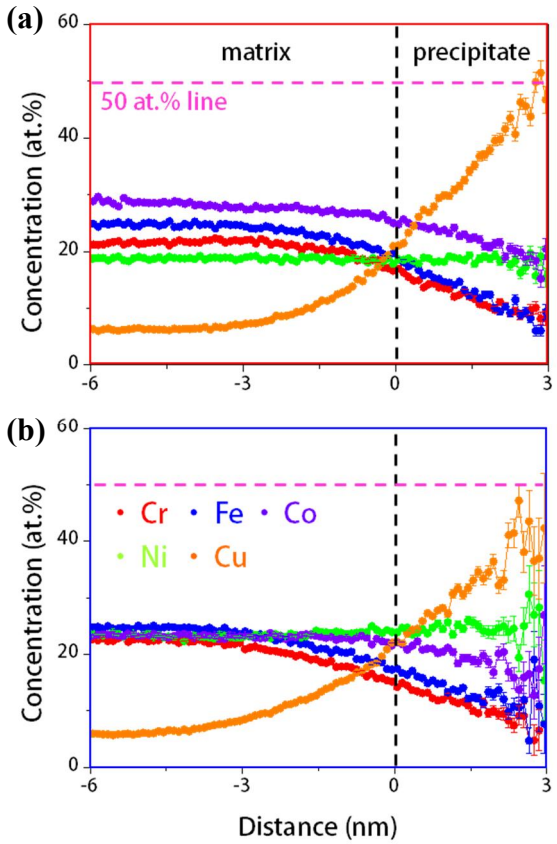

Figure 6.4 Proxigrams displaying the distribution of Cr (●), Fe (●), Co (●), Ni (●) and Cu (●) in the precipitates formed in the dendrite of CrFeCoNiCu HEA corresponding to (a) the red and (b) the blue dashed area in Figure 6.3.

(Figure 6.5(a)). It presented information about the damaged zone. Although the reconstruction atom map is delineated by 5 at.% Cu, precipitates were not clearly shown compared to the previous outcome. Additionally, it was difficult to determine the composition of the precipitates due to the chemical fluctuation in the proxigram (Figure 6.5(b)).

Therefore, the frequency distribution was utilized in order to determine the degree of atomic randomness statistically (Figure 6.6) [124]. The observed frequency distribution of this reconstruction tip in the entire area was in good agreement with the randomized distribution, showing that the alloy elements present a fairly random distribution. To investigate the randomness with the dose and the dose rate, the frequency distribution was investigated at the top and bottom regions. The deviation of an experimentally determined distribution from the calculated binomial distribution can be quantified by means of χ^2 statistics,

$$\chi^2 = \sum_{n=0}^{n_b} \frac{(e(n) - f(n))^2}{f(n)}$$

where e(n) is the number of blocks containing n solute atoms experimentally measured. In addition, the Pearson coefficient μ was introduced to explain the difference between the observed and the randomized distribution [124],

$$\mu = \sqrt{\frac{\chi^2}{N + \chi^2}}$$

where N is the number of blocks sampled. This allowed us to quantify the randomness of each element between 0 and 1. Additionally, a zero value of μ

indicated a random distribution, while a value close to 1 showed an association with the solute atoms. As a result, it was found that according to the profile, even when the bottom region is affected by implanted ions with an increase in the depth, most elements existed in a more random distribution, suggesting the nearly complete mixing of the alloy elements regardless of the implanted ions.

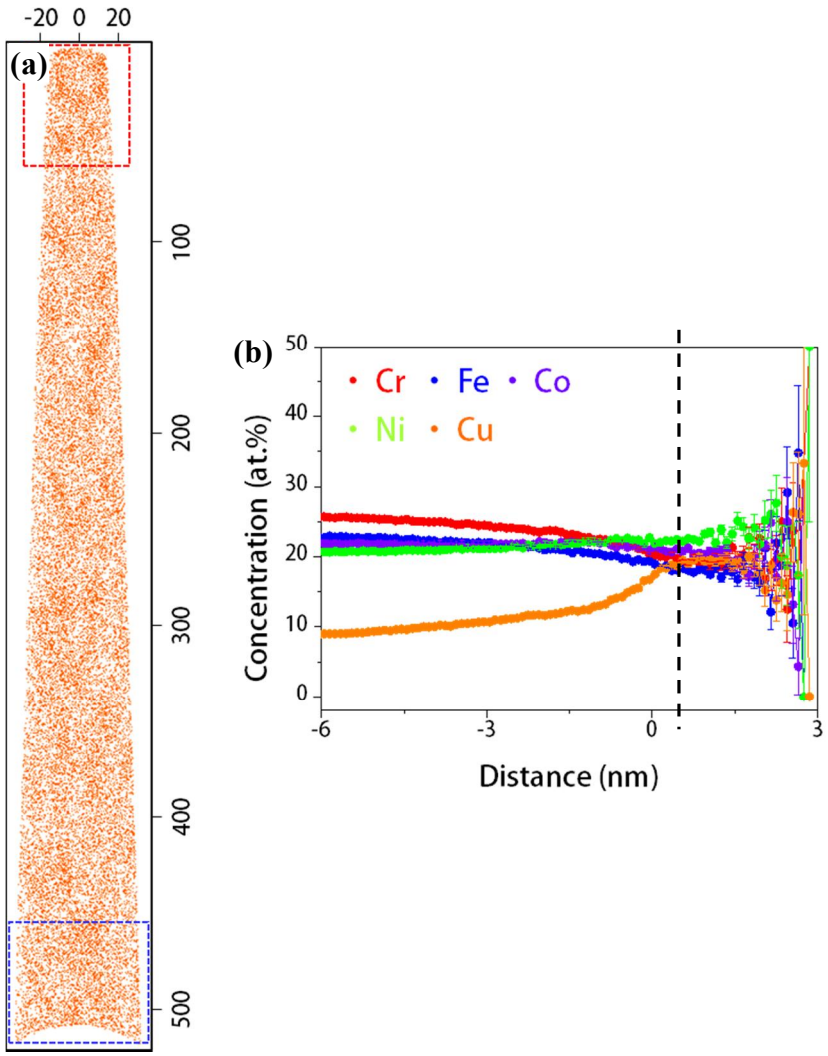

Figure 6.5 (a) 10 nm slice from an APT reconstructed Cu atom map delineated by 22 at.% Cu from 1.62 µm to 1.85 µm. (b) Proxigrams displaying the distribution of Cr (●), Fe (●), Co (●), Ni (●) and Cu (●) in the precipitates formed in the whole reconstructed volume.

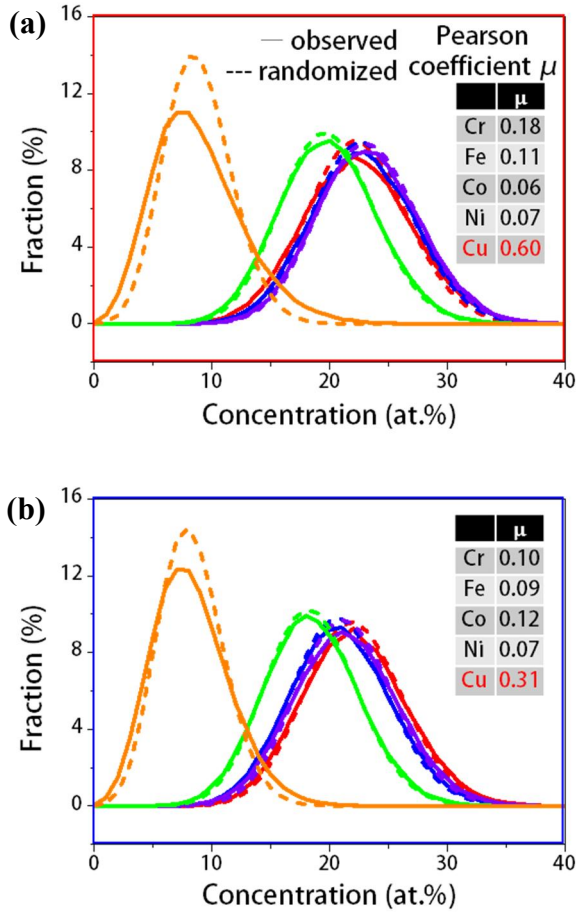

Figure 6.6 Frequency distribution and corresponding Pearson coefficient (inset) obtained at (a) top region marked by red dashed area and (b) bottom region marked by blue dashed area.

6.4 Determination of Effective Temperature

Driven processes such as severe plastic deformation and irradiation forces a system into a nonequilibrium configuration, producing various defects. A diffusion equation that explains atomic interdiffusion is constructed with two driving forces: (1) atomic collisions and (2) thermodynamic force [122]. For simplicity, the interdiffusion flux is presented as the sum of the ballistic flux and the diffusion flux driven by the gradient chemical potential. The effective free-energy density φ(c) is combined with Cahn's diffusion equation [125], as described below [122],

$$\varphi''^{(c)} = f'' + \frac{D_B}{M} = f'' + \frac{k_B T}{c(1-c)}\frac{D_B}{D}$$

where f˝ is the second derivative of the free energy per atom with respect to the concentration in a system with a uniform concentration c, M is the atomic mobility, c is the atomic fraction of the species, k_B is the Boltzmann constant, T is the temperature in kelvin, D_B is the ballistic diffusion coefficient, and D is the chemical-diffusion coefficient. Moreover, for application to a solid solution, the simplest model for the free energy of a solid solution is devised using a regular solution model, as follows:

$$\varphi(c) = \omega c(1-c) + k_B T[clnc + (1-c)\ln(1-c)]$$

Here, ω is the ordering energy. If D_B/D is independent of the atomic fraction of the species c, the change in the effective free energy by ballistic diffusion φ(c) can be determined by combining Cahn's diffusion equation and a regular

solution model. This is described below.

$$\varphi(c) = \omega c(1-c) + k_B T\left(1 + \frac{D_B}{D}\right)[clnc + (1-c)\ln(1-c)].$$

It is interpreted from this equation that ballistic effects increase the configurational entropy, which is equivalent to an increase in the temperature. Hence, according to Martin's law, *the equilibrium configuration of a solid solution at temperature T under irradiation flux which fixes the value of D_B/D to Δ is the configuration for which the same solid solution would have outside irradiation at a temperature that is defined as the effective temperature $T_{eff}=T(1+\Delta)$ with $\Delta=D_B/D$* [122]. Here, Δ is a function of the irradiation flux and temperature. Accordingly, the effective temperature, an imaginary temperature describing the thermodynamic states in a driven system, is determined by

$$T_{eff} = T\left(1 + \frac{D_B}{D}\right).$$

where the ballistic diffusion coefficient D_B and the irradiation temperature T are constant. This effective temperature can be applied when the condition after the driven process is saturated or when the microstructure becomes randomized, i.e., akin to those of an amorphous state or a fully solid solution.

Therefore, using a pseudo-binary phase diagram, the effective temperature of the dendrites in the CrFeCoNiCu HEA was determined in order to investigate the phase stability under irradiation (Figure 6.7) Based on the frequency distribution, the composition of the dendritic area under irradiation was approximately 8 at.%Cu (Figure 6.6), and the

microstructure under irradiation changed to an FCC1 solid solution phase region (Figure 6.5). Because the composition of the dendrites under irradiation was nearly 8 at.% Cu, the effective temperature was determined to range from 1000℃ to 1350℃. This range of the effective temperature was quite high, experimentally showing sluggish diffusion in HEAs.

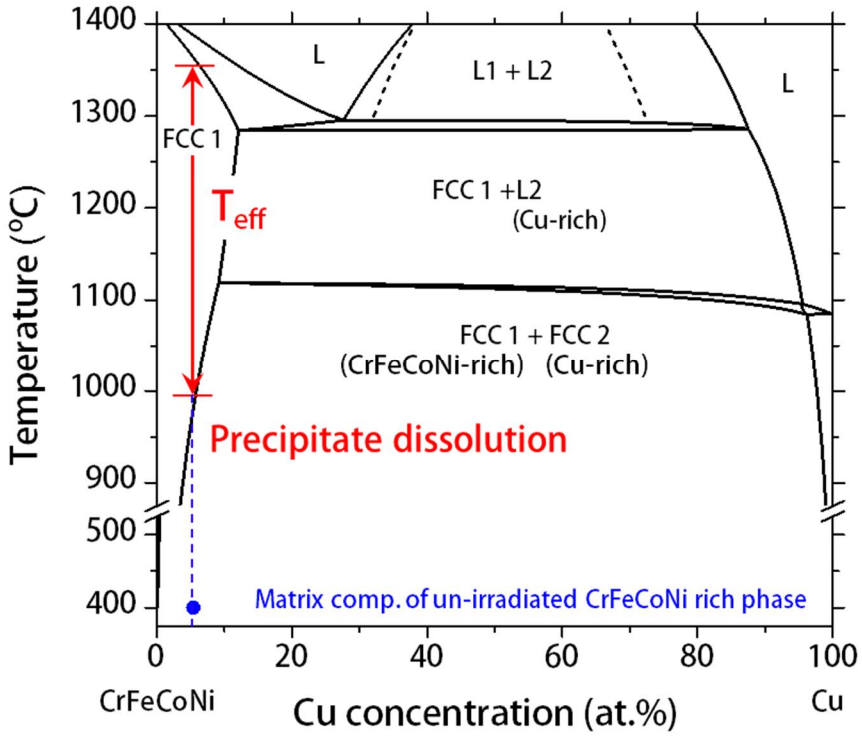

Figure 6.7 Determination of effective temperature using the composition of the precipitates measured by the frequency distribution.

6.5 Ostwald Ripening under Irradiation

In the previous section, the precipitates in the dendritic region of the CrFeCoNiCu HEA were completely dissolved into the matrix at the damaged zone under ion irradiation. When the implanted ion concentration and radiation damage increase with the depth, reaching nearly the peak points, precipitates were newly formed. The reconstruction atom maps (Figure 6.8 and Figure 6.9) provide information corresponding to region 3 in Figure 6.2. Figure 6.8 show the reconstruction Cu atom map and the proxigram delineated by 22 at.%Cu corresponding to region 3, showing increased implanted ion concentration and increased damage. Compared to the reconstruction atom map in Figure 6.5, the precipitates are newly formed by the implanted ion of Cu. Interestingly, the proxigram shows that the composition of the precipitates has a nearly 92 at.% Cu concentration, much higher than the Cu concentration of the precipitates in the dendrite area of the as-cast CrFeCoNiCu HEA (Figure 3.9 and Table 3).

Furthermore, 3D-APT was carried out at the damage peak point, corresponding to region 4 in Figure 6.2 (Figure 6.9). With an increase in the depth, the size of the precipitates clearly increased and the volume fraction of the precipitates decreased. Additionally, the proxigram in Figure 6.9(b) shows that the composition of precipitates has an approximate Cu concentration of 92 at.%, even with an increased depth. This means that the implanted ion affects not only the composition but the size and volume fraction of the

precipitates. This phenomenon is called ‘Ostwald ripening’, which occurs shrinkage of small particles and growth of larger particles when the concentration in the matrix shows a gradient. Precipitation and Ostwald ripening occur at regions 3 and 4 in Figure 6.2 due to the decrease in ballisticity with an increase in the depth and activated radiation-enhanced diffusion.

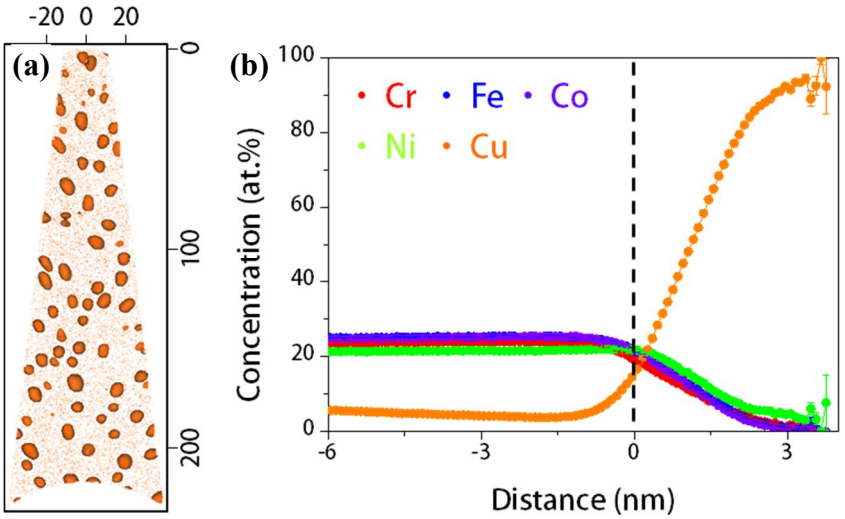

Figure 6.8 10 nm slice from an APT reconstructed Cu atom map delineated by 22 at.% Cu below from 2.43 μm to 2.63 μm. (b) Proxigrams displaying the distribution of Cr (●), Fe (●), Co (●), Ni (●) and Cu (●) in the precipitates formed in the whole reconstructed volume.

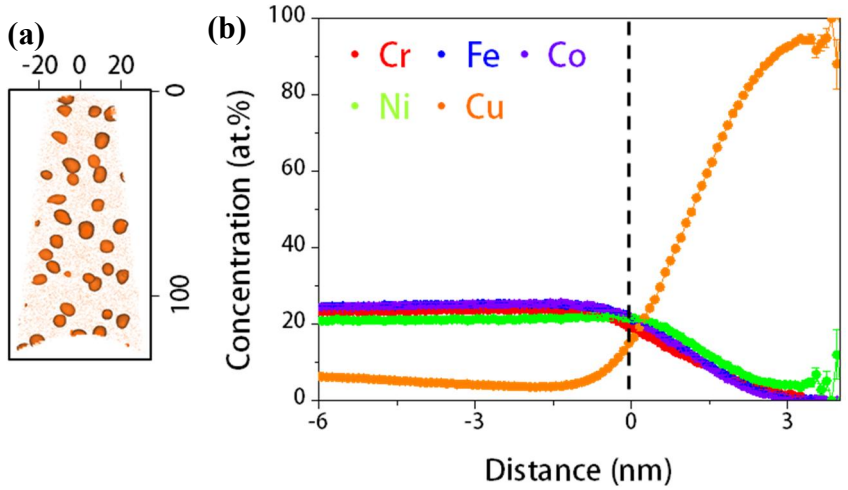

Figure 6.9 10 nm slice from an APT reconstructed Cu atom map delineated by 22 at.% Cu below from 2.90 μm to 3.03 μm. (b) Proxigrams displaying the distribution of Cr (●), Fe (●), Co (●), Ni (●) and Cu (●) in the precipitates formed in the whole reconstructed volume.

6.6 Phase Stability under Irradiation: Competition between Radiation-enhanced Diffusion and Ballistic Diffusion

As described in section 6.1, the dose rate effects influence the microstructural evolution under irradiation. The irradiation dose rate is given in units of dpa/sec, indicating the local density of the displacement defects, in this case the interstitial-vacancy pair per atom per unit of time. For example, smaller voids with higher density levels are observed in pure Ni at a higher dose rate and at a temperature of 575℃ [126]. Furthermore, while the sizes of dislocation loops are similar at high and low dose rates, the number density levels of the dislocation loops are higher in the Fe-Cr alloy at a higher dose rate and at 300℃. Additionally, at a low dose rate, Cr segregation in the matrix is more prominent, and the increase in irradiation hardening is due to the evolution of complex defect clusters [127].

Likewise, the dose rate is closely related to the evolution of defect clusters under irradiation, and the interaction between the displacement defects (interstitial-vacancy pairs) is affected by the material as well as by the defect mobility rate, irradiation conditions and other factors. Generally, the types of interaction can be classified according to three reaction paths [127]:

(1) Defects are lost at extended sinks such as dislocations and grain boundaries.

(2) Defect clusters are grown or shrunk by the capturing of point defects.

(3) Defects are mutually annihilated by recombinations of vacancies and interstitials.

Reaction 1, defect loss at the sink, is dominant at a low dose rate and/or a high irradiation temperature, and reaction 3 applies where defect recombinations are dominant at a high dose rate and/or low irradiation temperature (Figure 6.10)

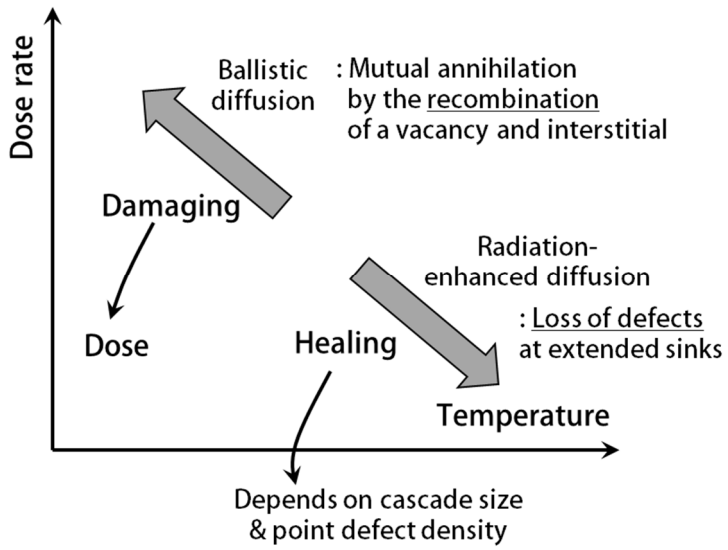

Figure 6.10 Phase stability under irradiation: competition between ballistic diffusion and radiation-enhanced diffusion.

6.7 Applicability of HEA as Nuclear Materials

As described in the previous sections, radiation damage causes changes in not only microstructures such as defect structures but also in alloy properties such as the mechanical properties and electrical resistivity levels. In this section, alloys widely used as nuclear materials, for example, reduced-activation ferritic/martensitic (RAFM) F28H, 9Cr oxide dispersion-strengthened (ODS) ferritic steel, and zircaloy-4, are utilized in order to compare the irradiation hardening of HEAs. Additionally, refractory HEAs are introduced. Those alloys were irradiated at 1 dpa and 10 dpa at room temperature using 9.5 MV Cu ions.

As shown in Figure 6.11, the changes in the hardness upon irradiation are compared in various alloy systems with different irradiation conditions. In order to normalize the mechanical properties and radiation damage, the fluence and normalized hardening were used, as determined by the ratio of the hardness of an un-irradiated alloy to that of an irradiated alloy. Irradiation hardening is observed in most alloy systems.

To check the reliability, the hardening of high-Cr ODS ferritic steel was compared to that of 9Cr ODS ferritic steel in this study. High-Cr ODS ferritic steel was irradiated under an irradiation condition in which the incident energy and dose are nearly identical while the irradiation temperature is slightly higher. Although the irradiation hardening is depressed at a lower irradiation temperature in the high-Cr ODS [11, 12], 316 ODS [12], and F82H

ODS ferritic steel [12], the 9Cr ODS ferritic steel and F82H [14]in this study appears to have a lower value of irradiation hardening in Figure 6.11. This resulted from the irradiation conditions, i.e., the incident energy and particle type, and from characteristics of the indentation technique used, in this case the type of indenter tip and load, and the intrinsic characteristics of the materials. Furthermore, the mechanical property change under irradiation was affected by various factors, and individual roles of the mechanical properties were not fully elucidated. Therefore, the variation in the mechanical properties is difficult to explain simply in terms of the irradiation damage.

Therefore, only the alloy systems obtained at identical irradiation and indentation conditions were compared. Irradiation hardening decreased in the order of CrFeCoNi, Ni and Cu, which is in good agreement with earlier work [85]. Specifically, RAFM F28H, 9Cr ODS ferritic steel, and zircaloy-4 showed nearly unchanged hardness upon irradiation, suggesting excellent radiation resistance. On the other hand, FCC HEAs such as CrFeCoNi alloy and CrFeCoNiCu alloy as well as pure FCC metals such as Cu and Ni show relatively high irradiation hardening compared to those of alloys widely used as nuclear materials. Although the irradiation hardening outcomes suggest vulnerability to irradiation, these hardening value of HEAs are in fact quite remarkable. These results can be attributed to the prominent difference between the BCC matrix with enhanced radiation tolerance and the FCC matrix with weaker resistance, and they are reasonable because the alloys investigated in this dissertation were not optimized in terms of the

microstructure, i.e., with regard to the initial defect density or grain size and the alloying conditions. Therefore, the alloy design as well as the microstructure should be optimized in order to utilize HEAs as nuclear materials.

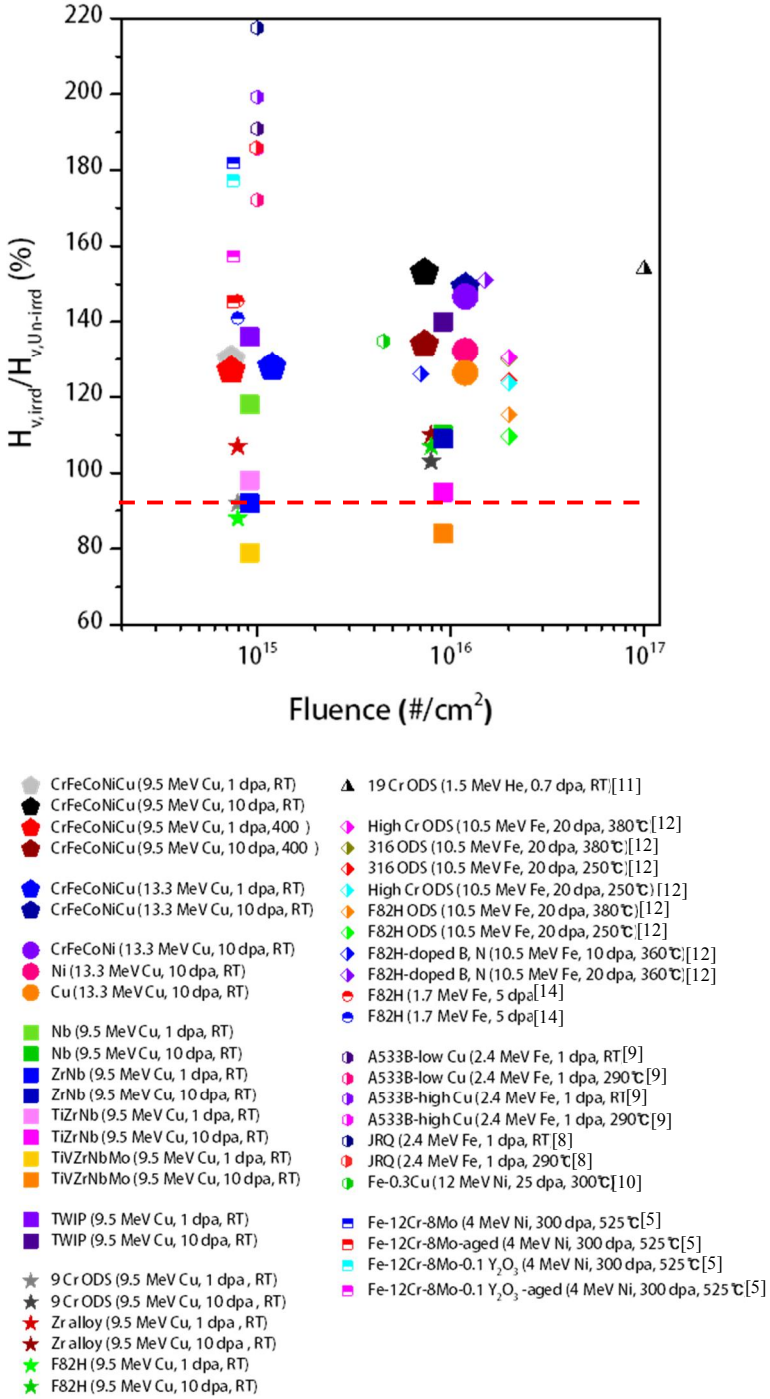

Figure 6.11 Hardness change in various alloy system upon

6.8 Summary

Under irradiation, the phase stability is explained by the competition between radiation-enhanced diffusion and the ballistic diffusion. In this chapter, the effect of the ballisticity on the microstructure under irradiation is comprehensively investigated by characterizing the composition, size, and fraction of precipitates with an increase in the depth using 3D-APT.

At region 2, which is mostly not affected by implanted ions but where irradiation damage increases, ballistic diffusion was activated. As a result, the precipitates shrunk and then dissolved. However, when the implanted ion concentration starts to increase, precipitation newly occurred. The new precipitates showed an unchanged Cu concentration, an increase in the size, and a decrease in the fraction of precipitates upon an increase in the depth, suggesting that Ostwald ripening and activated radiation enhanced the diffusion.

In order to elucidate the applicability of HEAs as nuclear materials, the variation in the hardness was compared with that of various alloys, though further studies are needed with regard to the optimization of the alloying process and the microstructure.

Chapter 7. Outlook and Conclusion Remarks

The phase stability of FCC HEAs under extreme environments was investigated in this dissertation. In detail, the microstructural evolution and variations in the properties were characterized in a multi-scale analysis with annealing at high temperatures and under irradiation.

In Chapter 3, the microstructure of the as-cast CrFeCoNiCu HEA was observed in depth in a preliminary experiment in order to investigate the response of this material in an extreme environment. Here, nm-sized Cu-rich precipitates in a CrFeCoNi-rich dendritic region and several tens of nm-sized CrFeCoNi-rich precipitates in a Cu-rich interdendritic region were observed, showing a composition of the dendritic matrix similar to that of the precipitates in the interdendritic region, and vice versa. Using a pseudo-binary phase diagram calculated between CrFeCoNi and Cu, it was elucidated that the Cu-rich precipitates in the dendritic region were formed by solid-state phase separation; after the CrFeCoNi-rich phase was separated from the Cu-rich interdendritic phase in a liquid state, it solidified. Furthermore, the annealing condition was set in a three-phase region using a phase diagram in order to cause variations in the microstructure, such as the creation of precipitates. After annealing at 1100℃ for 24 hours, pre-existent spherical Cu-rich precipitates grew into disk-type Cu-rich precipitates and cuboidal CrFeCoNi-rich precipitates grew with the same shape. In addition, new

precipitation occurred from the matrix due to the solubility change which occurred upon annealing. In order to investigate the effects of precipitation on the mechanical properties, the trends of the composition, size, and volume fraction of the precipitates were studied and compared to the hardness trend. It was found that the size and volume fraction of the precipitates greatly affected the mechanical properties regardless of intrinsic characteristics such as the composition, showing an optimum value of the hardness. Therefore, two types of pillars, one which shows only dendrites and the other which includes both dendrites and an interdendritic region were compressed in order to study the effects of such a composite structure. Consequently, the dendritic pillar showed multiple slips but the composite pillar containing both dendritic and interdendritic regions showed only barreling without boundary sliding and multiple slips, suggesting the formation of damage-tolerant HEAs with a stable interface during deformation. From the results of this study, with a microstructure-tailoring concept based on a phase diagram, the microstructures of HEAs can be controlled, which may offer insight into the excellent mechanical properties and phase stability characteristics of HEAs.

To describe the phase stability under irradiation, the microstructural evolution was elucidated considering the defect scale. In Chapter 4, the evolution and dynamics of the defect clusters of CrFeCoNiCu HEAs were observed upon an increase in the temperature under MV electron irradiation in real time using HVEM. As a result, dislocation loops were observed mainly in the dendritic region while SFTs were the dominant defect clusters in the

interdendritic region, all of which being vacancy-type clusters. Due to the conversion from SFT to dislocation loops and vice versa, dislocation loops were often observed in the interdendritic region and SFTs were shown in the dendrites. These sessile defect clusters grew or shrunk with atomic fluctuations or very rapid growth or shrinkage rates along the <111> direction of the [110] zone axis. Nonetheless, the average size and number density of the defect clusters did not change with an increase in the irradiation time at room temperature under MV electron irradiation. The defect stability under electron irradiation was investigated in terms of the defect lifetime. Dislocation loops in the dendrites were sustained for more time compared to the defect lifetimes of SFTs in the interdendritic region, suggesting good defect stability of dislocation loops in HEAs under irradiation. Furthermore, the dislocation loops in the dendritic regions were uniformly distributed and scarcely grew, even at an elevated temperature, whereas the SFTs were agglomerated and defect-cluster-free regions appeared upon an increase in the temperature, showing a large change in the size distribution. The dynamics of defect clusters for a direct description of the defect behavior in real time under irradiation should be determined because doing so provides a guideline with which to understand radiation damage at the final stage of irradiation.

The phase stability under irradiation can be evaluated by assessing the competition between the radiation-enhanced diffusion and the ballistic diffusion. At a high dose rate and a low irradiation temperature, ballistic diffusion was activated, while at a low dose rate and a high irradiation

temperature, radiation-enhanced diffusion was facilitated. Thus, the microstructural evolution under irradiation was investigated while considering the dose rate. In Chapter 5, the irradiation-enhanced recrystallization in CrFeCoNiCu HEAs was quantified using the ASTAR™-PED technique after MV Cu ion irradiation. Given that numerous dislocations were produced in the grains upon irradiation and the dislocation increase facilitated by vacancy diffusion was activated by radiation-enhanced diffusion, irradiation-induced recrystallization occurred. Additionally, nucleation of new grains was observed near the surface and boundary region in not only the dendritic region but also the interdendritic region upon ion irradiation, suggesting CDRX combined with DDRX. Specifically, the surface provides defect sinks and the lowest dose rate, indicating activated diffusion near the surface under irradiation. As a result, polygonization with a low angle boundary was observed in the dendrites. On the other hand, the interdendritic region was characterized by dynamic recrystallization with high-angle boundary upon irradiation. This occurred because the dendritic region shows 1) a lower amount of initial defects; 2) enhanced defect recombination in a cascade reaction, leading to fewer surviving defects after the reaction; and 3) slower defect mobility attributed to the slower thermal equilibrium diffusion and suppressed radiation-enhanced diffusion due to the fewer defects. Therefore, the chemical complexity and sluggish diffusion in the dendritic phase (the high-entropy phase) enabled an increase in the radiation resistance according to a simple comparison of the microstructures.

In Chapter 6, the effects of the dose rate on the microstructure were investigated in order to elucidate the phase stability under irradiation. Consequently, the composition, size, and fraction of the precipitates in the dendritic region were quantified using 3D-APT with an increase in the depth. Given that the dose rate follows the trend of the total number of vacancies, it increases and then decreases. At the region in which the implanted ions do not have considerable effects but the irradiation damage increases, the precipitates shrunk and then dissolved with an increase in the depth, suggesting the activation of ballistic diffusion, whereas when the implanted ion concentration begins to increases, new precipitates formed, showing an unchanged Cu concentration, an increase in the size, and a decrease in the fraction of precipitates with an increase in the depth, suggesting Ostwald ripening and activated radiation-enhanced diffusion. The variation in the hardness of the HEAs was then measured and compared with those of various alloys, including widely used nuclear materials and pure metals, in order to determine the applicability of HEAs as nuclear materials. The irradiation hardening of HEAs is a factor which suggests the radiation damage and it is higher than that of nuclear materials. The irradiation hardening of HEAs that is factor to have radiation damage was relatively higher than that of nuclear materials. These results stem from the fact that the BCC matrixes of widely utilized nuclear materials have greater radiation tolerance and the alloy designs and the microstructures are not optimized in CrFeCoNi or CrFeCoNiCu HEA. Therefore, studies with regard to the optimization of the alloying process and

the microstructure are also needed.

This dissertation covered microstructure evolution considering the scale of defects upon irradiation, suggesting excellent phase stability in HEAs. Furthermore, the radiation damage was elucidated in a stepwise manner in one alloy system, which is significant in the HEA field and in nuclear engineering.

Bibliography

[1] Advanced Analysis Ceneter in Korea Institute of Science and Technology.

[2] Ricotti ME. Nuclear energy: Basics, present, future. EPJ Web of Conferences, vol. 54: EDP Sciences, 2013. p.01005.

[3] Sickafus KE, Kotomin EA, Uberuaga BP. Radiation effects in solids: Springer Science & Business Media, 2007.

[4] NETZSCH. LFA 457 MicroFlash® (1100°C).

[5] Ohta J, Ohmura T, Kako K, Tokiwai M, Suzuki T. Journal of nuclear materials 1995;225:187.

[6] Geometry of electron beam in precession electron diffraction. Original diffraction patterns collected by C.S. Own at Northwestern University.

[7] Egerton R, Li P, Malac M. Micron 2004;35:399.

[8] Watanabe H, Masaki S, Masubuchi S, Yoshida N, Kamada Y. Journal of Nuclear Materials 2011;417:932.

[9] Fujii K, Fukuya K, Hojo T. Journal of Nuclear Science and Technology 2013;50:160.

[10] Sekimura N, Kamada T, Wakasugi Y, Okita T, Arai Y. Journal of nuclear materials 2002;307:308.

[11] Pouchon MA, Chen J, Ghisleni R, Michler J, Hoffelner W. Experimental mechanics 2010;50:79.

[12] Liu C, Yu C, Hashimoto N, Ohnuki S, Ando M, Shiba K, Jitsukawa S. Journal of Nuclear Materials 2011;417:270.

[13] Tsai K-Y, Tsai M-H, Yeh J-W. Acta Materialia 2013;61:4887.

[14] Ando M, Tanigawa H, Jitsukawa S, Sawai T, Katoh Y, Kohyama A, Nakamura K, Takeuchi H. Journal of nuclear materials 2002;307:260.

[15] Bai X-M, Voter AF, Hoagland RG, Nastasi M, Uberuaga BP. Science 2010;327:1631.

[16] 김진우. Fabrication and mechanical response of nanoscale metallic glasses / 김진우. 나노 스케일 비정질 합금의 제조 및 기계적 변형 거동 분석에 대한 연구. 서울: 서울 : 서울대학교 대학원, 2016.

[17] Senkov O, Miller J, Miracle D, Woodward C. Nature communications 2015;6:6529.

[18] Nordlund K, Djurabekova F. Journal of Computational Electronics 2014;13:122.

[19] Tong C-J, Chen Y-L, Yeh J-W, Lin S-J, Chen S-K, Shun T-T, Tsau C-H, Chang S-Y. Metallurgical and Materials Transactions A 2005;36:881.

[20] Zhang Y, Zuo TT, Tang Z, Gao MC, Dahmen KA, Liaw PK, Lu ZP. Progress in Materials Science 2014;61:1.

[21] He J, Wang H, Huang H, Xu X, Chen M, Wu Y, Liu X, Nieh T, An K, Lu Z. Acta Materialia 2016;102:187.

[22] Zinkle SJ, Snead LL. Annual Review of Materials Research 2014;44:241.

[23] Was GS. Fundamentals of radiation materials science: metals and alloys: Springer, 2016.

[24] Atkinson A, Barnett S, Gorte RJ, Irvine JTS, McEvoy AJ, Mogensen M, Singhal SC, Vohs J. Nature Materials 2004;3:17.

[25] incorporated F. Site-specific TEM specimen preparation of grain boundary corrosion in nickel-based alloys using the FIB "plane-view lift-out" technique.

[26] Okamoto NL, Yuge K, Tanaka K, Inui H, George EP. AIP Advances 2016;6:125008.

[27] Yeh JW, Chen SK, Lin SJ, Gan JY, Chin TS, Shun TT, Tsau CH, Chang SY. Advanced Engineering Materials 2004;6:299.

[28] Oh HS, Ma D, Leyson GP, Grabowski B, Park ES, Körmann F, Raabe D. Entropy 2016;18:321.

[29] 김윤중. 한국기초과학지원연구원에 설치된 초고전압 투과전자현미경의 소개. The Korean Physical Society, 2005.

[30] Miotello A, Kelly R. Nuclear Instruments and Methods in Physics Research Section B: Beam Interactions with Materials and Atoms 1997;122:458.

[31] Ackland G. Science 2010;327:1587.

[32] Gao M, Alman D. Entropy 2013;15:4504.

[33] Zhao Y, Chen H, Lu Z, Nieh T. Acta Materialia 2018;147:184.

[34] Gludovatz B, Hohenwarter A, Catoor D, Chang EH, George EP, Ritchie RO. Science 2014;345:1153.

[35] Chang S-Y, Li C-E, Huang Y-C, Hsu H-F, Yeh J-W, Lin S-J. Scientific reports 2014;4:4162.

[36] Laurent-Brocq M, Akhatova A, Perrière L, Chebini S, Sauvage X, Leroy E, Champion Y. Acta Materialia 2015;88:355.

[37] Padture NP, Gell M, Jordan EH. Science 2002;296:280.

[38] Choudhuri D, Gwalani B, Gorsse S, Mikler C, Ramanujan R, Gibson M, Banerjee R. Scripta Materialia 2017;127:186.

[39] Valiev R. Nature Materials 2004;3:511.

[40] Valiev R. Nature materials 2004;3:511.

[41] Averback R, Diaz de la Rubia T. Solid State Physics 1997;51:281.

[42] Jien-Wei Y. Ann. Chim. Sci. Mat 2006;31:633.

[43] Viladot D, Veron M, Gemmi M, Peiro F, Portillo J, Estrade S, Mendoza J, Llorca-Isern N, Nicolopoulos S. J Microsc 2013;252:23.

[44] Ziegler JF, Biersack JP. 2008.

[45] Stoller RE, Toloczko MB, Was GS, Certain AG, Dwaraknath S, Garner FA. Nuclear Instruments and Methods in Physics Research Section B: Beam Interactions with Materials and Atoms 2013;310:75.

[46] Otto F, Dlouhý A, Somsen C, Bei H, Eggeler G, George EP. Acta Materialia 2013;61:5743.

[47] Gludovatz B, Hohenwarter A, Thurston KV, Bei H, Wu Z, George EP,

Ritchie RO. Nature communications 2016;7:10602.
[48] Gludovatz B, Hohenwarter A, Catoor D, Chang EH, George EP, Ritchie RO. Science 2014;345:1153.

[49] F Otto AD, Ch Somsen, H Bei, G Eggeler, EP George. Acta Materialia 2013;61:5743.

[50] Z Li KP, Y Deng, D Raabe, CC Tasan. Nature 2016;534:227.

[51] JW Yeh SC, SJ Lin, JY Gan, TS Chin, TT Shun, CH Tsau, SY Chang. Advanced Engineering materials 2004;6:299.

[52] Y Zhang XY, PK Liaw. JOM 2012;64:830.

[53] ON Senkov JS, SV Senkova, DB Miracle, CF Woodward. Intermetallics 2011;19:698.

[54] Z Tang MG, H Diao, T Yang, J Liu, T Zuo, Y Zhang, Z Lu, YQ Cheng, YW Zhang, KA Dahmen, PK Liaw, T Egami. JOM 2013;65:1848.

[55] ON Senkov GW, DB Miracle, CP Chuang, PK Liaw. Intermetallics 2010;18:1758.

[56] J Antonaglia XX, Z Tang, CW Tsai, JW Qiao, Y Zhang, MO Laktionova, ED Tabachnikova, JW Yeh, ON Senkov, MC Gao, JT Uhl, PK Liaw, KA Dahmen. JOM 2014;66:2002.

[57] CJ Tong MC, SK Chen, JW Yeh, TT Shun, SJ Lin, SY Chang. Metallurgical and Materials Transactions A 2005;36A:1263.

[58] JW Yeh YC, SJ Lin, SK Chen. Materials Scence Forum 2007;560:1.

[59] MJ Yao KP, CC Tasan, D Raabe. Scripta Materialia 2014;72-73:5.

[60] Choi W-M, Jung S, Jo YH, Lee S, Lee B-J. Metals and Materials International 2017;23:839.

[61] Ng C, Guo S, Luan J, Shi S, Liu CT. Intermetallics 2012;31:165.

[62] Zhang C, Zhang F, Chen S, Cao W. Jom 2012;64:839.

[63] Zhang F, Zhang C, Chen S-L, Zhu J, Cao W-S, Kattner UR. Calphad 2014;45:1.

[64] Zhao Y, Chen H, Lu Z, Nieh T. Acta Materialia 2018.

[65] Lu Y, Gao X, Jiang L, Chen Z, Wang T, Jie J, Kang H, Zhang Y, Guo S, Ruan H. Acta materialia 2017;124:143.

[66] Lu Y, Dong Y, Guo S, Jiang L, Kang H, Wang T, Wen B, Wang Z, Jie J, Cao Z. Scientific reports 2014;4:6200.

[67] Lu Y, Gao X, Dong Y, Wang T, Chen H-L, Maob H, Zhao Y, Jiang H, Cao Z, Li T. Nanoscale 2018.

[68] Knipling KE, Karnesky RA, Lee CP, Dunand DC, Seidman DN. Acta Materialia 2010;58:5184.

[69] M Margarido MR. Journal of Materials Processing Technology 2003;133:149.

[70] Takeda M, Suzuki N, Shinohara G, Endo T, Van Landuyt J. physica status solidi (a) 1998;168:27.

[71] Asato M, Hoshino T. Journal of magnetism and magnetic materials 2004;272:1372.

[72] Chen W, Ding X, Feng Y, Liu X, Liu K, Lu Z, Li D, Li Y, Liu C, Chen X-Q. Journal of Materials Science & Technology 2017.

[73] Kiener D, Grosinger W, Dehm G. Scripta Materialia 2009;60:148.

[74] Zhang H, Siu KW, Liao W, Wang Q, Yang Y, Lu Y. Materials Research Express 2016;3:094002.

[75] Raghavan R, Kirchlechner C, Jaya BN, Feuerbacher M, Dehm G. Scripta Materialia 2017;129:52.

[76] Kiener D, Minor AM. Acta Materialia 2011;59:1328.

[77] Ma D, Yao M, Pradeep KG, Tasan CC, Springer H, Raabe D. Acta Materialia 2015;98:288.

[78] Tong C-J, Chen M-R, Yeh J-W, Lin S-J, Chen S-K, Shun T-T, Chang S-Y. Metallurgical and Materials Transactions A 2005;36:1263.

[79] Z Zhang MM, J Wang, B Gludovatz, Z Zhang, SX Mao, EP George, Q Yu, RO Ritchie. Nature communications 2015;6:1.

[80] Parish CM, Wang K, Edmondson PD. Scripta Materialia 2018;143:169.

[81] Egami T, Guo W, Rack PD, Nagase T. Metallurgical and Materials Transactions A 2013;45:180.

[82] Zhang Y, Stocks GM, Jin K, Lu C, Bei H, Sales BC, Wang L, Beland LK, Stoller RE, Samolyuk GD, Caro M, Caro A, Weber WJ. Nat Commun 2015;6:8736.

[83] Xia SQ, Yang X, Yang TF, Liu S, Zhang Y. Jom 2015;67:2340.

[84] Granberg F, Nordlund K, Ullah MW, Jin K, Lu C, Bei H, Wang LM, Djurabekova F, Weber WJ, Zhang Y. Phys Rev Lett 2016;116:135504.

[85] Jin K, Lu C, Wang LM, Qu J, Weber WJ, Zhang Y, Bei H. Scripta Materialia 2016;119:65.

[86] Kumar NAPK, Li C, Leonard KJ, Bei H, Zinkle SJ. Acta Materialia 2016;113:230.

[87] Abhaya S, Rajaraman R, Kalavathi S, David C, Panigrahi BK, Amarendra G. Journal of Alloys and Compounds 2016;669:117.

[88] Lu C, Yang T, Jin K, Gao N, Xiu P, Zhang Y, Gao F, Bei H, Weber WJ, Sun K, Dong Y, Wang L. Acta Materialia 2017;127:98.

[89] He M-R, Wang S, Shi S, Jin K, Bei H, Yasuda K, Matsumura S, Higashida K, Robertson IM. Acta Materialia 2017;126:182.

[90] Yang T, Xia S, Guo W, Hu R, Poplawsky JD, Sha G, Fang Y, Yan Z, Wang C, Li C, Zhang Y, Zinkle SJ, Wang Y. Scripta Materialia 2018;144:31.

[91] Lu C, Niu L, Chen N, Jin K, Yang T, Xiu P, Zhang Y, Gao F, Bei H, Shi S, He MR, Robertson IM, Weber WJ, Wang L. Nat Commun 2016;7:13564.

[92] Xia S-q, Wang Z, Yang T-f, Zhang Y. Journal of Iron and Steel Research, International 2015;22:879.

[93] Nagase T, Anada S, Rack PD, Noh JH, Yasuda H, Mori H, Egami T. Intermetallics 2012;26:122.

[94] Nagase T, Anada S, Rack PD, Noh JH, Yasuda H, Mori H, Egami T. Intermetallics 2013;38:70.

[95] Nagase T, Rack PD, Noh JH, Egami T. Intermetallics 2015;59:32.
[96] Weizhong H, J. DM, A. MN, Engang F, Subhasis S, D. RA, Yongqiang W, S. CJ, J. BI, Amit M. Advanced Materials 2013;25:6975.

[97] Bringa EM, Monk J, Caro A, Misra A, Zepeda-Ruiz L, Duchaineau M, Abraham F, Nastasi M, Picraux S, Wang Y. Nano letters 2011;12:3351.

[98] Sun C, Bufford D, Chen Y, Kirk M, Wang Y, Li M, Wang H, Maloy S, Zhang X. Scientific reports 2014;4:3737.

[99] J Li KY, Y Chen, M Song, H Wang, MA Kirk, M Li, X Zhang. Nano Letter 2015;15:2922.

[100] Y Chen JL, KY Yu, H Wang, MA Kirk, M Li, X Zhang. Acta Materialia 2016;111:148.

[101] Y Chen KY, Y Liu, S Shao, H Wang, MA Kirk, J Wang, X Zhang. Nature communications 2015;6:1.

[102] Maher D, Eyre B. Philosophical Magazine 1971;23:409.

[103] Matsukawa Y, Zinkle SJ. Science 2007;318:959.

[104] Sonoda T, Kinoshita M, Ray ILF, Wiss T, Thiele H, Pellottiero D, Rondinella VV, Matzke H. Nuclear Instruments and Methods in Physics Research Section B: Beam Interactions with Materials and Atoms 2002;191:622.

[105] Matzke H, Wang LM. Journal of Nuclear Materials 1996;231:155.

[106] Kai JJ, Huang WI, Chou HY. Journal of Nuclear Materials 1990;170:193.

[107] El-Atwani O, Efe M, Heim B, Allain JP. Journal of Nuclear Materials 2013;434:170.

[108] Vaidya WV, Ehrlich K. Journal of Nuclear Materials 1983;113:149.

[109] Nesterova EV, Rybin VV, Zinkle SJ, Barabash VR, Naberenkov AV. Plasma Devices and Operations 1994;2:293.

[110] Zinkle SJ, Kulcinski GL, Mansur LK. Journal of Nuclear Materials 1986;141-143:188.

[111] Zaefferer S, Elhami N-N. Acta Materialia 2014;75:20.

[112] Park N, Watanabe I, Terada D, Yokoyama Y, Liaw PK, Tsuji N. Metallurgical and Materials Transactions A 2015;46:1481.

[113] Valdez J, Usov I, Won J, Tang M, Dickerson R, Jarvinen G, Sickafus K. Journal of Nuclear Materials 2009;393:126.

[114] Porter DA, Easterling KE, Sherif M. Phase Transformations in Metals and Alloys, (Revised Reprint): CRC press, 2009.

[115] Ungár T. Scripta Materialia 2004;51:777.

[116] Huang K, Logé R. Materials & Design 2016;111:548.

[117] Gourdet S, Montheillet F. Acta Materialia 2003;51:2685.

[118] Hsieh H, Diaz de la Rubia T, Averback RS, Benedek R. Physical Review B 1989;40:9986.

[119] Gali A, George EP. Intermetallics 2013;39:74.

[120] Dienes GJ, Damask A. Journal of Applied Physics 1958;29:1713.

[121] Varvenne C, Luque A, Curtin WA. Acta Materialia 2016;118:164.

[122] Martin G. Physical Review B 1984;30:1424.

[123] Knipling KE, Karnesky RA, Lee CP, Dunand DC, Seidman DN. Acta Materialia 2010;58:5184.

[124] Moody MP, Stephenson LT, Ceguerra AV, Ringer SP. Microscopy research and technique 2008;71:542.

[125] Cahn JW. Acta Metallurgica 1961;9:795.

[126] Westmoreland J, Sprague J, Smidt Jr F, Malmberg P. Radiation effects 1975;26:1.

[127] Hardie CD, Williams CA, Xu S, Roberts SG. Journal of Nuclear Materials 2013;439:33.

Abstract in Korean

초 록

극한 환경 하에서 FCC 하이엔트로피 합금의 상 안정성 고찰

김진연

서울대학교 공과대학 재료공학부

하이엔트로피 합금은 다성분 원소가 유사한 비율로 합금화되어 원자 단위 응력을 갖는 고용체를 의미하며 주원소에 소량의 합금원소를 첨가하여 합금 특성을 제어하는 전통적인 합금 설계 패러다임에서 벗어난 새로운 합금 시스템이다. 이러한 하이엔트로피 합금은 극저온 뿐만 아니라 상온 및 고온에서의 우수한 기계적 특성과 방사화 환경 하에서의 우수한 저항성으로 인해 다양한 산업 분야에서 각광을 받고 있다. 특히, 안정한 고용체 구조, 느린 확산 속도와 격자 비틀림 효과로 인하여 하이엔트로피 합금의 조사 저항성이 우수할 것으로 예상되지만 현재까지는 이에 대한 연구가 각 시스템과 여러 조사 조건 하에서 산발적으로 수행되어 하이엔트로피 합금 조사 저항성에 대한 연구가 체계적으로 진행되지 못한 상태이다.

방사화 환경 하에서의 하이엔트로피 합금의 거동을 규명하기 위하여 CrFeCoNi rich 고용체의 수지상과 Cu-rich 고용체의 수지상간으로 구성되어 있는 CrFeCoNiCu 하이엔트로피 합금을 모델 합금으로 선택하였다. 또한, 두 상은 모두 FCC 구조를 가지므로 같은 조사 조

건 하에서 두 상을 TEM 에서 동시에 관찰하기 용이하다. 이를 이용하여, 조사 환경 하에서 결함 크기에 따른 하이엔트로피 합금의 미세구조적 변화를 토대로 하이엔트로피 합금의 조사 저항성 즉, 상안정성에 대해 규명하였다. 이에 대한 기본 실험으로 CrFeCoNiCu 하이엔트로피 응고 조직을 다단계로 분석하였으며 그 결과 수지상 내에 나노 크기의 Cu-rich 석출물이, 수지상간 내에는 CrFeCoNi-rich 석출물이 형성됨을 관찰하였다. 이를 통해 Cr, Fe, Co, Ni 원소들과 Cu 원소는 화학적으로 완전히 분리됨을 확인하였으며 이에 CrFeCoNi 와 Cu 의 준이성분계 상태도를 계산한 후 이를 통해 각 석출물의 응고 거동을 규명하였다. 상태도에서 고상 CrFeCoNi, Cu 와 Cu-rich 액상의 3상 영역인 1100℃ 에서 24시간 열처리 수행 후 노냉각하였으며 그 결과 기존에 있던 석출물의 성장과 열처리에 의한 고용도 변화에 의한 새로운 석출물이 형성되었다. 기계적 특성에 대한 석출물의 효과를 살펴보기 위해 석출물의 조성, 크기, 분율을 고려하였으며 석출물의 내재적 특성보다는 크기와 분율에 기계적 특성이 크게 영향을 받는다는 것을 알 수 있었다. 또한, 수지상과 수지상간 복합재 구조를 압축 시 계면에서 미끄러지는 현상과 슬립 없이 수지상간이 뭉개지면서 변형하는 것을 통해 변형에 매우 안정한 계면임을 확인할 수 있었다.

조사 환경 하에서 하이엔트로피 합금의 상 안정성을 평가하기 위하여 전자 및 이온 조사를 수행하였다. 초고전압 투과 전자현미경을 통하여 실시간으로 결함의 동역학 거동을 관찰하였다. 그 결과 수지상 내에는 전위 루프가, 수지상간 내에는 stacking fault tetrahedra (SFT) 가 주로 형성되었으며 결함 유지 시간이 수지상 내 전위루프가 더 긴 것을 알 수 있었다. 또한, 온도가 증가함에도 수지상 내 전위 루프는 균일한 분포와 상온과 유사한 크기 분포를 보이는 반면, 수지상간 내 SFT 는 더 응집되어 결함 분포가 다소 불균일하며

결함도 매우 크게 성장하게 된다.

더 나아가 이온 조사를 수행함으로서 조사 결함에 의해 활성화된 확산과 원자 간 충돌에 의해 활성화된 확산의 경쟁으로서 나타나는 상 안정성에 대해 고찰하였다. 조사 결함에 의한 확산이 활성화되는 표면 근처에서 조사 결함들에 의해 결정립 분리가 유발되었으며 이에 따라 전위 상승에 활성화되어 재결정화가 나타났다. 특히, 수지상은 저각 경계를 특징으로 하는 아결정립이 형성되었으며 수지상간은 고각 경계를 보이는 재결정이 조사 후 형성되었으며 이를 세차회절법을 이용하여 정량화하였다. 이 두 상의 극명한 차이는 하이엔트로피 합금의 낮은 초기 결함 밀도, 캐스케이드 내 결함의 높은 재결합 분율, 느린 확산 속도 및 억제된 조사에 의해 활성화된 확산에 의해 유발된다.

또한, 깊이에 따른 수지상 내 석출물의 변화를 3D-APT 를 이용하여 정량화하였으며 충돌에 의해 활성화된 확산에 의해 석출물의 수축 및 용해가 나타난 것을 관찰하였다. Driven system 에서의 상 안정성 지표인 effective temperautre 을 도입하였을 때 수지상의 경우 매우 높은 값을 보이며 이는 이온 조사 시 하이엔트로피 합금의 우수한 상 안정성을 의미한다. 또한, 점차 깊이가 증가함에 따라 주입된 이온의 영향을 받게 되면 충돌에 의한 확산에 대한 영향이 감소함에 따라 새로운 석출물이 형성되며 이 때, Ostwald ripening 현상을 보이게 된다.

하이엔트로피 합금의 원자력 재료로서의 응용 가능성을 고찰하고자 조사 후 경도 변화를 측정 후 다른 원자력 재료와 순금속과 비교하였다. 원자력 재료에 비해 FCC 하이엔트피 합금의 경도 증가가 상대적으로 매우 크지만 이는 원자력 재료가 조사 저항성이 우수한 BCC 기지를 가지고 있고 본 연구에서 활용된 FCC 하이엔트로피 합금의 최적화가 되어 있지 않다는 점에서 당연한

결과로 예상해볼 수 있다. 따라서 추후에 하이엔트로피 합금 자체의 합금 설계 및 미세구조 최적화에 대한 연구가 필요해 보인다.

본 연구에서는 결함 크기에 따른 미세구조 변화 분석을 통해 조사 환경 하에서 하이엔트로피 합금의 우수한 상 안정성을 규명하였으며 하나의 합금 시스템에서 단계별로 조사 손상을 규명한 결과는 학문적 측면뿐 만 아니라 산업적으로 기반이 되는 중요한 가치가 있는 연구 결과를 도출하였다.

주요어: 하이엔트로피 합금, 조사, 상 안정성, 투과전자현미경,

Atom probe tomography

학 번: 2014-30214